

AD-A170 192

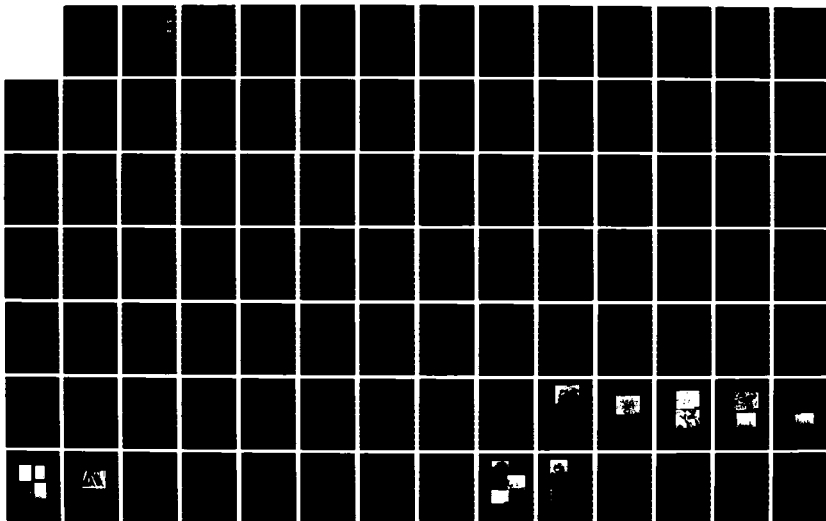
ADVANCED HIGH TEMPERATURE COATING SYSTEMS BEYOND  
CURRENT STATE OF THE ART. (U) PITTSBURGH UNIV PA DEPT  
OF MATERIALS SCIENCE AND ENGINEERING. A ASHARY ET AL.

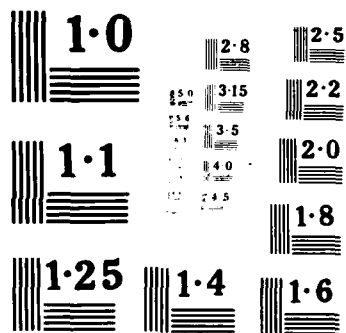
1/2

UNCLASSIFIED

15 APR 86 AFOSR-TR-86-0481 AFOSR-80-0089 F/G 11/3

NL





## PORT DOCUMENTATION PAGE

AD-A170 192

2b. DECLASSIFICATION/DOWNGRADING SCHEDULE

4. PERFORMING ORGANIZATION REPORT NUMBER(S)

University of Pittsburgh Report

6a. NAME OF PERFORMING ORGANIZATION

University of Pittsburgh

6b. OFFICE SYMBOL  
(If applicable)

6c. ADDRESS (City, State and ZIP Code)

848 Benedum Hall  
Materials Science & Engineering Department  
University of Pittsburgh, Pgh., PA 152618a. NAME OF FUNDING/SPONSORING  
ORGANIZATION

AFOSR

8b. OFFICE SYMBOL  
(If applicable)

NC

8c. ADDRESS (City, State and ZIP Code)

Bolling Air Force Base  
DC 20332-644811. TITLE (Include Security Classification) Advanced High Tem-  
perature Coating Systems Beyond Current State of the Art

12. PERSONAL AUTHOR(S)

Ashary, A. A., Meier, G. H. and Pettit, F. S.

13a. TYPE OF REPORT

Final Technical Report

13b. TIME COVERED

FROM 80-1-1 to 84-12-31

14. DATE OF REPORT (Yr., Mo., Day)

1986, April, 15

15. PAGE COUNT

16. SUPPLEMENTARY NOTATION

17. COSATI CODES

FIELD GROUP SUB. GR.

18. SUBJECT TERMS (Continue on reverse if necessary and identify by block number)  
Coatings, Oxidation, Oxide scale adherence

19. ABSTRACT (Continue on reverse if necessary and identify by block number)

Alpha- $\text{Al}_2\text{O}_3$  and the  $\text{SiO}_2$  are the two most effective reaction product barriers that can be used to protect alloys from oxidation at temperatures above  $1000^\circ\text{C}$ . In the present work the techniques to improve the adherence of  $\text{Al}_2\text{O}_3$  scales on MCrAl coating alloys are studied and the characteristics of  $\text{SiO}_2$  scales formed on Ni-Si alloys are investigated.

The theoretical aspects of oxide-metal adhesion are examined and the factors which affect the adherence of oxide scales in general are clearly defined. A critical review of the previously proposed mechanisms of the improved scale adherence by active element additions is presented. Experimentally, the effects of small additions of yttrium and hafnium on the isothermal and cyclic oxidation behavior of MCrAl type alloys are studied.

The base alloys used in the study of  $\text{Al}_2\text{O}_3$  scale adherence were Ni-20wt%Cr-10wt%Al and Co-20wt%Cr-10wt%Al. Both the isothermal and the cyclic oxidation tests were carried out at  $1100^\circ\text{C}$  for varying durations. Emphasis is given to the insitu study of the oxide scale

20. DISTRIBUTION/AVAILABILITY OF ABSTRACT

UNCLASSIFIED/UNLIMITED ☒ SAME AS RPT ☐ DTIC USERS ☐

21. ABSTRACT SECURITY CLASSIFICATION

Unclassified

22a. NAME OF RESPONSIBLE INDIVIDUAL

G. H. Meier

22b. TELEPHONE NUMBER  
(Include Area Code)

22c. OFFICE SYMBOL

failure process. An acoustic emission (AE) technique was employed for this purpose. The above study indicates that the  $\text{Al}_2\text{O}_3$  scale failure processes are quite different in the doped (i.e. containing oxygen active elements) and undoped alloys. The results of AE experiments can be most consistently explained on the basis of a stronger scale/substrate interface in the doped alloys rather than the reduction of residual stresses in the scale due to the active element addition. The AE technique was also found to be useful in evaluating the long term thermal cyclic resistance of the alloys.

Although both yttrium and hafnium can be very effective in improving the adherence of  $\text{Al}_2\text{O}_3$  scales, there are some basic differences in their oxidation behavior in alloys. Therefore, the optimum conditions for their addition also differ. It has been proposed that the oxidation behavior of an oxygen active element in an MCrAl alloy can be related to its solubility in the alloy and most of the commonly used oxygen active elements can be divided into two groups based on their solubilities in MCrAlY type alloys.

Alloys in the Ni-Si system (5 to 22.5wt% Si) have been oxidized in the temperature range 900 to 1100°C. Alloys containing approximately 20wt% Si were found to oxidize at rates as slow or slower than those for  $\alpha\text{-Al}_2\text{O}_3$  growth. The influence of alloy Si content, thermal cycling, reduced  $\text{PO}_2$ , and the presence of water vapor in the oxidation rates of Ni-Si alloys are described.

AFOSR-TR- 86-0481

Advanced High Temperature  
Coating Systems Beyond  
Current State-of-The-Art-Systems

Final Report  
on  
Contract No. 80-9089

MATERIALS SCIENCE AND ENGINEERING

University of Pittsburgh  
Pittsburgh, Pennsylvania 15261



**Advanced High Temperature  
Coating Systems Beyond  
Current State-of-The-Art-Systems**

**Final Report  
on  
Contract No. 80-0089**

**Submitted To  
AFOSR**

**by**

**A. Ashary, G. H. Meier, F. S. Pettit  
Department of Materials Science  
and Engineering**

**University of Pittsburgh  
Pittsburgh, PA 15261**

**April 15, 1986**

AIR FORCE OFFICE OF SCIENTIFIC RESEARCH (AFOSR)  
NATIONAL AERONAUTICS AND SPACE ADMINISTRATION  
This report is the property of the AFOSR and is  
approved for publication only in accordance with AFOSR-12.  
Distribution is unlimited.  
MATTHEW J. KETTER  
Chief, Technical Information Division

## TABLE OF CONTENTS

### ABSTRACT

I. <u>INTRODUCTION</u>	1
II. <u>ADHERENCE OF <math>Al_2O_3</math> SCALES ON MCrAl TYPE COATING ALLOYS</u>	2
1. INTRODUCTION	2
2. THEORY OF ADHESION AND OXIDE FAILURE	2
2.1 Definition of Adhesion	2
2.2 Nature of Oxide-Metal Adhesion	2
2.3 Factors Effecting Adherence of Oxide Scales	3
2.4 Residual Stresses	4
2.5 Stress Relieving	6
2.6 Mechanical Failure of Scales	6
3. INFLUENCE OF REACTIVE ADDITIONS ON GROWTH AND ADHERENCE OF $Al_2O_3$ SCALES	9
3.1 Introduction	9
3.2 Initial Development of $Al_2O_3$ Scales	9
3.3 $Al_2O_3$ Scale Growth Process	10
3.4 Morphologies of Alumina Scales	11
3.5 Proposed Models of Scale Adherence	11
4. EXPERIMENTAL TECHNIQUES AND PROCEDURES	18
4.1 Acoustic Emission Technique	18
4.2 Materials	21
4.3 Alloy and Specimen Preparation	21
4.4 Experimental Procedures	21
5. EXPERIMENTAL RESULTS	23
5.1 Microstructure of the Alloys	23
5.2 Isothermal Oxidation Weight Gain Tests	24
5.3 Acoustic Emission Study of $Al_2O_3$ Scale Failure	24
5.4 Cyclic Oxidation Weight Change Tests	27
5.5 Mechanical and Chemical Stripping of $Al_2O_3$ Scales	28
6. DISCUSSION OF RESULTS	29
6.1 Isothermal Oxidation Behavior	29
6.2 Mechanical Failure of $Al_2O_3$ Scales	34
6.3 Cyclic Oxidation Resistance of the Alloys	38
6.4 Mechanism of Improved Scale Adherence	41
6.5 Optimum Conditions for the Active Element Additions	43
7. SUMMARY AND CONCLUSIONS	44

Accession For	
NTIS CRA&I	<input checked="" type="checkbox"/>
DTIC TAB	<input type="checkbox"/>
Unannounced	<input type="checkbox"/>
Distribution	
By	
Distribution	
Availability Codes	
Availability Codes	
Special	

### III. OXIDATION OF Ni-Si ALLOYS

1. INTRODUCTION	47
1.1 Oxidation of Si	47
1.2 Oxidation of SiO <sub>2</sub> -Forming Alloys	49

2. Experimental	49
-----------------	----

3. Results and Discussion	50
---------------------------	----

4. Summary and Concluding Remarks	52
-----------------------------------	----

IV. REFERENCES	53
----------------	----

TABLES AND FIGURES	60
--------------------	----



## I. INTRODUCTION

This program was concerned with defining coatings compositions, structures and surface treatments which can be used to obtain new systems possessing superior high temperature oxidation resistance compared to the current state-of-the-art MCrAlY systems and diffusion aluminide coatings. The approach which was used consisted of attempting to obtain reaction product barriers with improved protective properties compared to those formed on state-of-the-art systems.

A number of oxide systems were examined in this program and their protectiveness as reaction product barriers compared (e.g.  $\alpha\text{-Al}_2\text{O}_3$ ,  $\text{Cr}_2\text{O}_3$ ,  $\text{SiO}_2$ ,  $\text{MgO}$ ,  $\text{BeO}$ ). It was concluded that only alumina ( $\alpha\text{-Al}_2\text{O}_3$ ) and silica ( $\text{SiO}_2$ ) had potential for use to develop improved systems. For example,  $\text{Cr}_2\text{O}_3$  could not be used at temperatures in excess of  $1000^\circ\text{C}$  due to the formation of gaseous  $\text{CrO}_3$ , and  $\text{MgO}$  and  $\text{BeO}$  cracked and spalled excessively in the presence of water vapor.

The further investigation of alumina and silica scales has been pursued by using a variety of conventional tests, in particular, isothermal and cyclic oxidation where specimens after exposure have been examined by using optical and scanning electron metallography. From the onset of these investigations, however, it was apparent that these conventional testing techniques were not an adequate means to compare the protectiveness of these scales. Hence several new tests procedures have been examined and used to more effectively study and compare the protective properties of alumina and silica. These tests have involved the development of procedures to measure the load to pull such scales from the surfaces of alloys, and the use of acoustic emission measurements to describe the cracking and spalling in the scales upon cooling from the test temperature.

This report consists of two parts. The first part is concerned with  $\text{Al}_2\text{O}_3$  scales and techniques to improve the adherence of such scales to metallic alloys. The second part involves results obtained with alloys upon which silica scales are formed and grow.

## II. ADHERENCE OF $\text{Al}_2\text{O}_3$ SCALES ON MCrAl TYPE OF COATING ALLOYS

### 1. INTRODUCTION

Alpha- $\text{Al}_2\text{O}_3$  is currently the most effective reaction product barrier that can be used to protect alloys from oxidation at temperatures above 1000°C.<sup>(1)</sup> Diffusion of oxygen through grain boundaries in these scales controls the oxidation rate.<sup>(2,3)</sup> While it may be possible to decrease oxidation rates by attempting to control the structure of the  $\alpha\text{-Al}_2\text{O}_3$  scales or by using dopants to inhibit grain boundary transport, a crucial factor determining the lives of coatings and structural alloys is cracking and spalling of these scales. In this section the factors effecting oxide scale cracking and spalling are examined and the concentrations of oxygen active elements to optimize alumina adherence are described.

### 2. THEORY OF ADHESION AND OXIDE FAILURE

#### 2.1 Definition of Adhesion

Adhesion between two phases, as defined in thermodynamics and in fracture mechanics, is the minimum work required per unit interfacial area to separate the two phases<sup>(4)</sup>. The thermodynamic property 'work of adhesion' is defined by the Dupre' equation<sup>(5)</sup>. For an oxide-metal system the Dupre' equation can be written as follows:

$$W_{ad} = \Delta(G_{O/m})^{ad} = \gamma_O + \gamma_m - \gamma_{O/m} \quad (1)$$

where  $\Delta(G_{O/m})^{ad}$  is the free energy change when 1 cm<sup>2</sup> of free surface of oxide and 1 cm<sup>2</sup> of free surface of metal are created out of 1 cm<sup>2</sup> of interface between oxide and metal;  $\gamma_O$  and  $\gamma_m$  are the surface free energies of oxide and metal respectively, and  $\gamma_{O/m}$  is the interfacial energy.

#### 2.2 Nature of Oxide-Metal Adhesion

Adhesion between two phases can be due to van der Waal forces, to chemical valence forces or to electrostatic forces. The exact nature of the interfacial forces between oxide scale and metallic substrate is not completely understood. Due to the fact that scales are developed as a result of reaction between metal atoms and atmospheric oxygen, these forces are probably electronic in nature, i.e., they are akin to the type of bonding between oxygen and metal ions. This hypothesis seems to be in agreement with the experimentally determined values of work of adhesion of various liquid metals and oxide substrates. First, these values are too high to be explained on the basis of van der Waal forces alone, and secondly, there appears to be a correlation between the adhesion and the free energy of oxide formation of a metal<sup>(6,7)</sup>.

McDonald and Eberhart<sup>(7)</sup> have proposed a model for metal-alumina (sapphire) interface bonding. Two types of atomic sites for metal atom on the close packed plane <0001> oxygen plane at the surface of sapphire can be distinguished, as shown in Figure 1. The metal atoms situated directly over the center of the hexagonal array of aluminum ions in the second layer, site A, are assumed to be chemically bonded to the oxygen ions on the surface with a bond energy comparable to that of bulk metal oxide. Those metal atoms situated directly over the aluminum ions of the second layer, site B, are assumed to be attracted by the surface oxygen ions by van der Waal type of forces. The values of work of adhesion calculated on the

basis of this model were found to be in close agreement with those measured experimentally for several liquid metals on a sapphire substrate.

No quantitative data are, however, available on the adhesion of solid-solid oxide-metal systems. The reason for this is the nonavailability of an experimental technique which can isolate the effect of interfacial forces on adhesion from the effects of residual stress in the system and of morphology of the interface.

An outstanding aspect of scale-metal adhesion, at least during the growth process, is its dynamic nature due to atom transfer at the interface. Although the sequence of steps involved in the atom transfer process across the interface is not known, it suffices to say that the bonds at the interface are continuously forming and breaking. It has also been suggested that electrostatic forces may also be important in the adhesion of oxide scale<sup>(8)</sup>. The electrostatic forces are supposed to arise due to the electric field in an oxide layer produced by the difference in the mobility of the ionic and electronic species.

### 2.3 Factors Effecting Adherence of Oxide Scales

The work of adhesion as defined by Eqn. (1) is only applicable to an ideal case where two pure phases free of elastic strains are in perfect contact with a flat interface. The oxides grown on metallic substrates contain several imperfections which can greatly alter the work of adhesion. The factors which can affect adherence of oxide scales can be divided into three groups: a) chemical factors, mechanical factors, and c) physical factors.

#### 2.3.1. Chemical Factors

Chemical factors are those which directly influence the interfacial forces responsible for adhesion, for instance, the impurities which tend to segregate at the interface. Assuming that chemical bond energies are important in the adhesion of oxide and metal, the impurities which have a higher affinity for oxygen as compared to the base metal will provide a stronger bond if they segregate at the interface. The well known phenomenon of temper embrittlement in steels is also associated with the effect of impurities on adhesion. Elements like phosphorus and antimony segregate at the alloy's grain boundaries and weaken the adhesion between grains<sup>(9)</sup>.

#### 2.3.2 Mechanical Factors

Oxide scales are invariably subjected to stresses which induce strain energy in the system thus lowering the necessary work of adhesion<sup>(10)</sup>. To take into account the strain energy stored in a system, the expression for the work of adhesion Eqn. 1 can be modified as follows:

$$W_{ad} = (\gamma_o + \gamma_m - \gamma_{o/m}) - tS \quad (2)$$

where  $S$  is the strain energy per unit volume and  $t$  is the thickness of the oxide layer. The term ' $tS$ ' is, therefore, the strain energy per unit interfacial area.

Spalling of an oxide scale occurs when the strain energy in a system exceeds the energy required to create the new surfaces of scale and substrate,

$$tS > (\gamma_o + \gamma_m - \gamma_{o/m}) \quad (3)$$

While the above is a necessary condition, it may not be a sufficient condition for spalling of scale depending upon the distribution and state of stress in the oxide. Other necessary conditions for spalling will be discussed in Section (2.6).

### 2.3.3. Physical Factors

Scale/substrate interfaces may contain several different types of irregularities, such as, voids, oxide intrusions, a discontinuous second oxide phase or just a geometrically irregular interface. These irregularities can modify the work of adhesion by altering both the interfacial work and strain energy in a system. A modified expression for the work of adhesion would then be written as follows:

$$W_{ad} = A(\gamma_o + \gamma_m - \gamma_{o/m}) - B(tS) \quad (4)$$

Values of coefficients A and B will depend on the type of irregularity present at the interface. Quantitative estimates of the coefficients A and B are rather difficult. A qualitative discussion of the effects of some of the most common morphological features of scale/substrate interfaces is, however, possible.

a) Voids at the Interface: Voids at the scale/substrate interface are a common occurrence. Origins of void formation in the  $Al_2O_3$  scale growth process are discussed in Section (3.5.5). Voids are physical gaps at the interface which reduce the interfacial work to be performed for separation of the oxide scale ( $A < 1$ ).

b) Irregular Interface: The effect of geometrical irregularities on adhesion is somewhat more complex. On one hand a geometrically irregular interface has more contact area between scale and substrate than a flat interface, which will increase the interfacial work of separation ( $A > 1$ ) but, on the other hand, depending upon the size and distribution of the irregularity, it can provide a stress concentration effect ( $B > 1$ ). Small and closely spaced oxide intrusions (Fig 2a) will not have as strong an influence on stress concentration as widely spaced large oxide intrusions (Fig 2b)(11).

Another effect of a geometrically irregular interface on adhesion is mechanical keying. An interface may develop in such a way that the oxide and substrate are mechanically interlocked as illustrated schematically in Figure 3.

c) Interface Phase: Oxygen active element rich oxide pegs are an example of an interface phase. Such a phase or particles at the interface can act much the same way as a geometrically irregular interface with an additional effect of the bond energy of oxide and second phase, and that of substrate and second phase.

## 2.4 Residual Stresses

Residual stresses in oxide scales are comprised of growth stresses and thermal stresses. Growth stresses are generated during the scale growth process and

thermal stresses arise during cooling of an oxidized metal or alloy. Several different origins of growth stresses have been identified<sup>(12,13)</sup>, but the most common and perhaps the most important one is the constrained volumetric dilatation of growing oxide, which is responsible for the compressive stresses in oxide scales. Volumetric dilatation may arise either from a greater volume of the oxide forming at the scale/substrate interface as compared to the volume of the replaced metal<sup>(14)</sup> or from the formation of new oxide within existing oxide<sup>(15,16)</sup>. Constraint to volumetric dilatation is due to the adhesion between scale and substrate. Tensile stresses may also result if the volume of growing oxide is less than the volume of replaced metal. Since tensile stresses are more damaging than compressive stresses, these oxides are usually not protective.

Thermal stresses mainly arise due to the difference in the coefficients of thermal expansion of oxide and metal. Metals usually have higher coefficients of thermal expansion than their oxides. On cooling, the substrate metal or alloy contracts more than the surface oxide which again generates compressive stresses in the oxide. These stresses are, therefore, added to the growth stresses.

The spatial distribution of stresses is essentially the same for both modes of stress development. The state of stress in an oxide scale is a function of the geometrical shape of the substrate. For a flat substrate these stresses are biaxial and compressive in the plane parallel to the interface, but for a cylindrical substrate, in addition to the biaxial compressive stresses (in axial and tangential directions), a tensile stress normal to the interface also exists as shown schematically in Figure 4. The residual stresses in an oxide layer can be characterized, in general, in terms of an unconstrained elastic mismatch strain,  $\Delta\epsilon$ , between the oxide and the substrate. For a thin oxide layer biaxial residual stresses are given by<sup>(17)</sup>

$$\sigma = E \Delta\epsilon / (1-\nu) \quad (5)$$

where  $\sigma$  is the residual stress in the oxide,  $E$  and  $\nu$  are the modulus of elasticity and Poisson's ratio for the oxide, respectively. The stress normal to the interface in the case of a cylindrical substrate is given as follows<sup>(17)</sup>

$$\sigma_i = E \Delta\epsilon (t/a) / 2(1-\nu) \quad (6)$$

where  $a$  is the radius of the substrate and  $t$  is the thickness of oxide layer. Notice for a flat semi-infinite plate (radius of curvature approaches infinity) the interface stress,  $\sigma_i$ , tends to zero. As opposed to the earlier misconception about the existence of a large shear stress at the scale/substrate interface, recent analysis by Evans et. al.<sup>(17)</sup> indicates zero shear stress at the interface except near the edges of the specimen.

Distribution of residual stresses and their magnitudes are also affected by the geometrical configuration of the scale/substrate interface. For instance, a wavy interface will have a stress component normal to the interface even in the case of a flat specimen. This situation is schematically illustrated in Figure 5.

Unconstrained mismatch strain associated with a difference in the thermal expansion coefficients,  $\Delta\alpha$ , is simply

$$\Delta\epsilon = \Delta\alpha \Delta T \quad (7)$$

where  $\Delta T$  is the cooling range that dictates the generation of elastic strain. However, the elastic strain associated with the scale growth process is difficult to assess. When the growth of new oxide takes place at the scale/substrate interface the actual elastic strain in the oxide is less than that which would be expected from the differences in the molar volumes of the oxide and the metal, because the volumetric dilatation is, at least, partially accommodated by the rigid outward displacement of oxide in the direction normal to the interface<sup>(12)</sup>. Every thing being equal, oxide growing on a curved surface is expected to have greater volumetric dilatational strain as compared to that growing on a flat substrate<sup>(13,18)</sup>. The volumetric dilatation from the growth of new oxide within existing oxide is difficult to determine, simply because the fraction of the oxide formed by such a process cannot be determined satisfactorily by any existing technique.

## 2.5 Stress Relieving

Growth stresses generated at high temperatures can be at least partially relieved either by the plastic deformation of the substrate or the oxide itself. The thermal stresses, however, are less likely to be relieved by either of such processes, because of the higher strain rates and lower temperatures involved. The subject of the plastic deformation of oxide scales has been extensively reviewed<sup>(12)</sup>. Deformation of the substrate metal may occur under the biaxial tensile stresses which are set forth to balance the compressive stresses in the oxide. Thin sheets and wires tend to deform more than thick cross section substrates<sup>(13)</sup>. In thicker substrates only localized deformation has been observed, such as the extrusion of the corners of an oxidized specimen<sup>(19)</sup>.

Stress relieving by the plastic deformation of the substrate alloy is naturally a function of the creep resistance of the alloy. MCrAl coating alloys are extremely weak at elevated temperatures. The flow stress measured for the NiCoCrAlY coating alloys at a strain rate of about  $10^{-4}$  to  $10^{-3} \text{ sec}^{-1}$  is not more than a few MPa above about  $1000^\circ\text{C}$ <sup>(20)</sup>. Some authors<sup>(21)</sup> have reported virtually unmeasurable strengths at these temperatures. There is no way of knowing the actual strain rate during the oxide growth process. Approximate estimates made by Stringer<sup>(12)</sup> indicates that the strain rates may range between  $10^{-4}$  to  $10^{-10} \text{ sec}^{-1}$ , depending upon the rates of oxidation. For  $\text{Al}_2\text{O}_3$  scales, because of their slow growth, strain rates should be on the lower side of this range. Therefore, the growth stress in  $\text{Al}_2\text{O}_3$  scales on MCrAlY type alloys may be expected to be relieved at least partially. Golightly et. al.<sup>(19,22)</sup> have indeed attributed the deformation of FeCrAlY specimens into a "dog bone configuration" to the stresses generated due to lateral growth of an  $\text{Al}_2\text{O}_3$  layer. Smialek and Gibala<sup>(23)</sup> have observed a high dislocation density ( $10^{10} \text{ cm}^{-2}$ ) in a NiCrAl alloy, both with and without yttrium, just beneath the oxide/alloy interface. This, they concluded, was due to the plastic deformation of the alloys at temperature ( $1100^\circ\text{C}$ ) to accommodate the growth stresses in the oxide. The frequently observed void formation at scale/substrate interfaces may also be a direct result of the creep deformation of the substrate metal under biaxial tension<sup>(24)</sup>.

## 2.6 Mechanical Failure of Scales

Mechanical Failure of oxide scales occurs when residual stresses in an oxide scale exceed a critical level. This critical level and the overall oxide failure process depend on the state of stress in the oxide and the fracture resistance of both the oxide and the scale/substrate interface. Biaxial tensile stresses in the plane

parallel to the interface tend to produce cracks in the oxide normal to the interface, while the biaxial compressive stresses have a tendency to cause buckling of the scale prior to crack growth along the interface. The latter situation is more common in oxide scales. Evans et. al.(17) have recently carried out a detailed stress analysis of the scale or coating failure under biaxial compressive stresses. They have divided the failure process into three consecutive steps: a) buckling of oxide scale, b) crack growth along the interface, and c) eventual spalling by the fracture of a separated portion of oxide. These steps are schematically shown in Figure 6. In the following, the scale failure process essentially based on their analysis will be described.

a) Buckling of Scale: The crack driving force (energy release) in the absence of buckling is zero, since there is no change in the strain energy of the system with the growth of an interfacial crack. This condition arises because of no stress normal to the interface. Following the buckling a strain energy release accompanies crack growth. Buckling of a scale occurs when the compressive stress in the scale exceeds a critical stress

$$\sigma = [kE/12(1-\nu^2)] (t/c)^2 \quad (8)$$

where  $c$  is the radius of separation between the oxide and substrate,  $t$  is the thickness of the oxide layer and  $k$  is a constant = 14.7. Note that a preexisting separation is a prerequisite for buckling, the smaller the radius of curvature the larger will be the stress required for buckling. Voids are frequently observed at the scale substrate interface. In the case of a curved or wavy interface, due to a normal stress component, an additional crack driving force exists and a preexisting separation is not required.

b) Crack Growth Along the Interface: Growth of the initial flaw occurs when the crack driving force reaches the critical value for the weakest material element within the vicinity of the interface. For example, if the interface exhibits a fracture resistance  $K_C^i$  lower than that of the oxide or substrate, a crack will extend along the interface when the stress exceeds a critical value  $\sigma^*$

$$\sigma^* = (K_C^i / t) [(1+\nu)/(1-\alpha)]^{1/2} \quad (9)$$

where  $\alpha = 0.4$ . The stronger the fracture resistance of the interface the larger will be the stress required for crack growth. Fracture resistance,  $K_C^i$ , of the interface is directly related to the interfacial work as defined in Eqn. (1). It is possible that the interface may not be the weakest material element in the vicinity of the flaw. Instead, the oxide may have some other plane of weakness, such as, due to a duplex grain structure in the oxide or a multilayered scale. In such situations a crack will grow along that plane of weakness instead of the scale substrate interface. The crack may also grow in the oxide in the through thickness direction due to a local inhomogeneity such as a second phase oxide particle.

c) Eventual Spallation: Continued growth of the interfacial crack leads to eventual spalling. The precise spalling condition is determined by the configuration of the substrate. Flat plates, subjected to a zero stress normal to the interface are

more resistant to spalling and an approximate spall condition develops when the interface crack attains a size  $C_s$  given by

$$C_s/t = (Et/K_C^i)^{1/2} \quad (10)$$

Notice, the size of the spalled scale,  $C_s$ , is a function of the fracture resistance of the interface. A weak scale/substrate bond will give rise to large oxide flakes. However, if the interface contains irregularities such as oxide protrusions the spalled flake size may be a function of the spacing between those protrusions.



### 3. INFLUENCE OF REACTIVE ADDITIONS ON GROWTH AND ADHERENCE OF $\text{Al}_2\text{O}_3$ SCALES

#### 3.1 Introduction

Good adherence of oxide scales is an essential requirement for high temperature oxidation resistance of alloys. Large improvements in the adherence of oxide scales are commonly obtained by small additions of oxygen active elements, such as Y, Hf, Zr etc., or by fine dispersion of their oxides in the alloys. Several different models have been proposed to explain the mechanism of improved scale adherence but none of them is universally accepted. These models are essentially based on the concepts developed in the previous section for scale adherence.

Each individual model emphasizes the role of reactive additions either affecting the interfacial forces between scale and metal, or reducing the amount of residual stresses in the oxide, or development of an interfacial morphology which promotes oxide adhesion. Since the development of stresses and interfacial morphology is related to the scale growth process the effects of reactive additions on the growth process of  $\text{Al}_2\text{O}_3$  scale will be discussed first and then a detailed discussion of the proposed models will follow. No attempt is made to review, comprehensively, the previous work, as such reviews can be found elsewhere<sup>(25,26)</sup>. The aim is to present the current understanding of the subject.

#### 3.2 Initial Development of $\text{Al}_2\text{O}_3$ Scale

An external layer of  $\text{Al}_2\text{O}_3$  scale can be developed on an alloy surface after a transient oxidation period, provided that the aluminum content of the alloy is sufficiently high. Several studies<sup>(27-30)</sup> have been carried out to define composition ranges in Ni, Co, and Fe base alloys over which a protective  $\text{Al}_2\text{O}_3$  scale will form when exposed to oxidizing atmospheres. These studies have been comprehensively reviewed by Wood and Stott<sup>(26)</sup>. It has been found that for a binary alloy, such as Ni-Al, Fe-Al and Co-Al, the amount of Al required to form a continuous  $\text{Al}_2\text{O}_3$  scale is considerably higher than the amount required when a third element such as Cr is present in the alloy. Chromium acts as a getter which prevents oxygen from entering the alloy, so  $\text{Al}_2\text{O}_3$  tends to develop as a complete layer instead of as an internal oxide<sup>(31,32)</sup>.

The sequence of steps leading to the development of a continuous  $\text{Al}_2\text{O}_3$  scale on a NiCrAl alloy has been described by Giggins and Pettit<sup>(28)</sup>, and shown schematically in Figure 7. A similar sequence can also be expected to be followed in scale development on CoCrAl or FeCrAl alloys. As the alloy is exposed to the oxidizing atmosphere the oxides NiO,  $\text{Al}_2\text{O}_3$ ,  $\text{Cr}_2\text{O}_3$ , as well as spinel phases ( $\text{NiAl}_2\text{O}_4$ ,  $\text{NiCr}_2\text{O}_4$ ) are developed on the surface of the alloy. The relative proportions of these phases are determined by initial composition of the alloy. As the oxidation continues, inward diffusion of oxygen and outward diffusion of metal ions take place close to the alloy surface. Because of the consumption of inward diffusing oxygen in the formation of  $\text{Cr}_2\text{O}_3$ , aluminum will have more chance to diffuse out to the alloy surface, without being internally oxidized, to form a continuous layer of  $\text{Al}_2\text{O}_3$ .

The process of  $\text{Al}_2\text{O}_3$  development is not significantly affected by the presence of oxygen active elements or dispersed oxide phases in the alloy. (These additions, particularly dispersed oxide particles, significantly enhance the selective oxidation process of chromium.) Nevertheless, there are some results that suggest a positive

influence of the reactive additions in the development of  $\text{Al}_2\text{O}_3$  scales. Giggins and Pettit<sup>(33)</sup> have observed less development of nickel rich oxides before the establishment of an  $\text{Al}_2\text{O}_3$  scale on Ni-15Cr-6Al doped with about 0.1% Y, as compared to the undoped alloy. Similarly, Allam et. al.<sup>(34)</sup> have found smaller amounts of Co rich phases in the scale on Co-10Cr-11Al containing up to 1% Y or Hf. In the latter alloys an even more pronounced effect was observed, when the hafnium was converted to  $\text{HfO}_2$  by a pre-internal oxidation treatment<sup>(35)</sup>. This is consistent with the observations made in  $\text{Cr}_2\text{O}_3$  forming alloys, that is, dispersed oxides are more effective than the active element additions in curtailing transient oxidation<sup>(36)</sup>.

The curtailment of transient oxidation by dispersed oxide phases in  $\text{Cr}_2\text{O}_3$  forming alloys is attributed to the increased nucleation sites for the first formed oxides, provided by the dispersed oxide particle<sup>(37)</sup>, which resulted in decreased distance between adjacent  $\text{Cr}_2\text{O}_3$  nuclei. Therefore, the time required for the lateral growth process to form a complete layer of  $\text{Cr}_2\text{O}_3$  is reduced<sup>(37)</sup>.

It is not clear, how the active element addition enhances the selective oxidation process. Oxidation of these elements may produce nucleation sites for  $\text{Al}_2\text{O}_3$ .

### 3.3 $\text{Al}_2\text{O}_3$ Scale Growth Process

Inert markers placed on  $\text{Al}_2\text{O}_3$  forming FeCrAl alloys<sup>(21,38,39)</sup>, doped with Y, Sc, Ce, and  $\text{Y}_2\text{O}_3$  or on the alloys without any dopant, are always found at the scale/gas interface, indicating that the growth of  $\text{Al}_2\text{O}_3$  has taken place by inward diffusion of oxygen, and the process is not altered by the additions. Since for oxygen, grain boundary diffusion is much faster than the bulk diffusion, it is generally accepted that oxygen transport in  $\text{Al}_2\text{O}_3$  scales occurs primarily via grain boundaries<sup>(40,41)</sup>. The growth rates of  $\text{Al}_2\text{O}_3$  scales, calculated on the basis of grain boundary diffusivity of oxygen were found to be in agreement with the experimental parabolic rate constants for the scales grown on NiCrAl and CoCrAl alloys with and without active element additions<sup>(33,42)</sup>. Furthermore,  $^{18}\text{O}$  tracer studies have also confirmed that the primary mode of transport is oxygen inward and that the profiles are most consistent with a grain boundary transport model<sup>(43)</sup>.

To explain the differences in the morphological features of scales developed on FeCrAl alloys with and without yttrium, Golightly et. al.<sup>(19)</sup> have suggested that, in addition to inward diffusion of oxygen some outward diffusion of aluminum ions also occurs, probably along line defects in the oxide, which leads to the formation of new oxide within the existing oxide layer. They have also suggested that incorporation of yttrium in the  $\text{Al}_2\text{O}_3$  scale suppresses the outward diffusion of aluminum ions and the growth of  $\text{Al}_2\text{O}_3$  scale then occurs exclusively by inward diffusion of oxygen. No experimental technique has as yet conclusively shown the contribution of aluminum ion migration to the growth of  $\text{Al}_2\text{O}_3$  scales.

While  $\text{Cr}_2\text{O}_3$  scale growth rates are substantially reduced by reactive additions<sup>(37,44)</sup>, only minor changes in the growth rates of  $\text{Al}_2\text{O}_3$  scales have been observed with these additions. Many studies<sup>(19,34,45)</sup> have indicated that  $\text{Al}_2\text{O}_3$  scale growth rates were first reduced by the addition of less than about 0.1% of Y, Zr or Hf, then increased by large additions up to 1.0%. There are also examples where no reduction in growth rates of  $\text{Al}_2\text{O}_3$  have been observed even with low concentrations of active elements<sup>(33,46)</sup>.

The decrease in growth rate with small additions can be explained on the basis of stoppage of aluminum outward diffusion as suggested by Golightly et. al.<sup>(34)</sup>. Alternative explanations such as segregation of yttrium to scale grain boundaries to decrease the inward diffusion of oxygen also exist<sup>(19,47)</sup>. Decreased weight gains during oxidation of Co-10Cr-11Al alloys with small amounts Y and Hf have been explained due to reduction in the transient oxidation<sup>(34)</sup>.

The increase in scale growth rates with increasing amounts of oxygen active elements can be more easily explained on the basis of short circuit paths that are formed due to incorporation of active element rich internally oxidized phases in the scale.

### 3.4 Morphologies of Alumina Scales

Morphological features of alumina scales vary greatly, depending upon the composition of the alloys, oxidation time, temperature, and surface conditions of the alloys. However, there are some commonly observed differences between the morphologies of alumina scales developed on alloys with and without active element additions. In fact many of the proposed mechanisms of the improved scale adherence are based on these morphological differences. In the following these differences and their possible origins will be discussed. Emphasis will be given to well developed alumina scales at temperatures between 1100°C and 1200°C.

The alumina scales formed on MCrAl type alloys without active element additions, are usually flat for shorter times and at lower temperatures. As the time and/or temperature at which oxidation is occurring is increased the scales start to wrinkle on the substrate surface and give rise to a 'convoluted' scale morphology. Associated with these wrinkles on the substrate alloy surfaces are usually smooth areas showing the detachment of the scale at high temperature during oxidation. The smooth areas on the substrate surfaces are sometimes referred to as voids<sup>(21)</sup>. The convoluted scale morphology is more pronounced on FeCrAl alloys than on NiCrAl or CoCrAl alloys. Wrinkles in the scale on FeCrAl alloys were observed<sup>(48)</sup> for times as short as one minute at 1200°C.

In contrast, the Al<sub>2</sub>O<sub>3</sub> scales on the alloys with reactive additions remain flat, unconvoluted and adherent even for extended periods of oxidation. However, the morphology of the scale/substrate interface has been found to be a strong function of the type, concentration and the state in which an active element is initially present in the alloy. That is, whether it was dissolved in the matrix or an intermetallic compound was formed with one of the elements in the alloy or it was dispersed as oxide particles.

### 3.5 Proposed Models of Scale Adherence

From the practical standpoint, the most significant aspect of reactive additions is the improved scale-alloy adherence. This aspect has been studied in great detail and a number of mechanisms have been proposed to explain this effect. Most of the models have been proposed on experimental observations which unfortunately seem to vary a great deal depending upon, the alloy system, types of additions and their concentration, and experimental conditions. No single model can explain all the different experimental observations. It must be realized that the improved scale adherence may be explained on the basis of more than one model. In other words, they are not necessarily mutually exclusive.

In the following discussion these models will be described and both the supporting and contradicting experimental evidence as obtained by different researchers will be presented.

### 3.5.1 Enhanced Scale Plasticity

It has been suggested that the elements such as Y may improve adhesion of the alumina scales by causing them to be more easily deformable and thereby allowing the relief of growth and thermal stresses that would otherwise have caused spalling of alumina scale<sup>(38,49-51)</sup>.

Like most other polycrystalline ceramics, alumina is not amenable to plastic deformation by dislocation motion<sup>(52)</sup>. Therefore, high temperature creep deformation processes such as diffusional creep, stress assisted dislocation climb or grain boundary sliding must be operative. These processes typically occur at temperatures in excess of approximately half the melting temperature (e.g.  $> 1000^{\circ}\text{C}$  for  $\text{Al}_2\text{O}_3$ ). Therefore, thermal stresses are not likely to be relieved by the creep deformation of oxide. Furthermore, the strain rates encountered during cooling periods are much higher than that required for creep deformation.

Diffusional creep is the most dominant mechanism in the deformation of fine grained ( $< 15\ \mu\text{m}$ ) alumina<sup>(53)</sup>. Alumina scales are generally fine grained ( $< 5\ \mu\text{m}$ ) and therefore they are more likely to deform by this process. Dislocation climb and grain boundary sliding are more important in the deformation of coarse grained ( $15\text{--}65\ \mu\text{m}$ ) alumina<sup>(53,54)</sup> and in the deformation of other oxides particularly at lower temperatures<sup>(13)</sup>.

Diffusional creep rates in fine grained alumina are controlled by the lattice and grain boundary diffusivity of aluminum ions<sup>(62)</sup>. Therefore, the plastic deformation of alumina can be improved either by grain refinement or by enhancing lattice diffusion of aluminum ions.

Alumina scales are inherently fine grained and most investigators failed to find any significant difference in the grain size of alumina scales grown on the alloy with and without the active elements<sup>(21,33)</sup>.

Delaunay et. al.<sup>(50)</sup> have found improved sintering kinetics of alumina when doped with  $\text{Y}_2\text{O}_3$ . The authors have concluded that the dissolved yttrium in alumina alters the defect structure such that increased diffusion rates are obtained which also improve the plasticity of  $\text{Al}_2\text{O}_3$ . It has been shown in various studies<sup>(55,56)</sup> on creep deformation of doped alumina, that the aliovalent dopants such as  $\text{Fe}^{+2}$  or  $\text{Ti}^{+4}$  improve the creep rate of fine grained alumina while the isovalent impurities such as  $\text{Cr}^{+3}$  do not have any significant effect on the creep rate. These results have been explained on the basis of a Frenkel type intrinsic defect structure of alumina. The acceptor dopants such as  $\text{Fe}^{+2}$  create aluminum ion interstitials and the donor impurities such as  $\text{Ti}^{+4}$  lead to the formation of aluminum ion vacancies<sup>(55)</sup>. Both of these defects will enhance aluminum lattice diffusion and hence creep rates over and above pure or Cr doped alumina. Yttrium is isovalent with aluminum so it is not expected to alter the intrinsic defect structure of alumina, however, conductivity measurements on yttrium doped alumina carried out by El-Aiat and Kroger<sup>(57)</sup> have shown that the yttrium despite it being isoelectronic with aluminum acts as a donor in  $\text{Al}_2\text{O}_3$  presumably because of its large atomic size. This result can explain the improved sintering kinetics of yttrium doped alumina as observed by Delaunay et. al.<sup>(50)</sup>

Alumina scales usually contain some acceptor impurities such as  $\text{Fe}^{+2}$  incorporated from the base metal. These impurities should have the same effect as a yttrium addition in improving creep rates due to the reasons mentioned above. In fact El-Aiat and Kroger<sup>(57)</sup> have suggested that the yttrium lowers the mobility of aluminum ions in alumina in the presence of impurities like  $\text{Fe}^{+2}$ .

Grain boundary sliding may be another possibility of stress relieving of the alumina scale particularly because of a columnar grain structure. However, Tien and Pettit<sup>(21)</sup> and Kumar and Douglass<sup>(58)</sup> have suggested that the scale plasticity should actually be decreased with active element additions if such a mechanism is operative since  $\text{Y}_2\text{O}_3$ ,  $\text{YAlO}_3$  and  $\text{Y}_2\text{Al}_3\text{O}_{12}$  (YAl garnet) which form at grain boundaries inhibit grain boundary sliding.

Recently Evans et. al.<sup>(17)</sup> have suggested a model for diffusional creep of fine columnar grain alumina under biaxial compressive stress. According to this model, deformation occurs by stress induced diffusion along the grain boundaries normal to the interface (under normal compressive stress) and down the oxide/alloy interface (zero or tensile stress depending upon the geometry of the interface). They have shown that the creep rate diminishes as oxide thickness increases.

While there is a possibility of stress relaxation by plastic deformation of alumina scales at high temperature, via mechanisms associated with creep, there is no conclusive evidence that the deformability of alumina is modified by the incorporation of either active element or oxide particles within the scale. In contrast Tien and Pettit<sup>(21)</sup> have reported more apparent plastic deformation of alumina scales on undoped alloys.

Deformation of the alloy is possibly another means whereby stress relief can occur. Golightly et. al.<sup>(19)</sup> observed apparent deformation of the alloy due to 'lateral growth' of alumina scales as evidenced by the 'dog bone' structure. However, the loads required to deform typical alumina forming alloys were not particularly affected by the yttrium concentration<sup>(33)</sup>.

### 3.5.2 Modification to the Growth Process

This model is essentially based on the modification of the scale growth mechanism such that smaller growth stresses are produced. Golightly et. al.<sup>(19)</sup> have applied the concept of stress generation by lateral growth to  $\text{Al}_2\text{O}_3$  scales which was first proposed by Rhines and Wolf<sup>(15)</sup> to explain the stress generation in NiO. As pointed out earlier, growth of an alumina scale occurs predominantly by the inward diffusion of oxygen along the grain boundaries. However, Golightly et. al.<sup>(19)</sup>, have suggested that, in addition to inward oxygen diffusion down the alumina grain boundaries, some outward diffusion of aluminum occurs, probably along line defects in the oxide. Reaction between the inward and outward diffusing species results in the formation of oxide within the existing scale layer. Hence, lateral growth of the oxide occurs as oxidation proceeds, leading to the rapid development of high compressive stresses and consequently localized detachment of the scale from the underlying alloy. They suggest that condensation of voids along the scale/alloy interface and the continuing lateral growth of the scale result in the development of a convoluted morphology of the oxide leading to oxide detachment at temperature and extensive spalling during cooling.

Based on this model, the increased adherence of the scale due to yttrium additions was mainly attributed to the prevention of the formation of convoluted

morphologies. Incorporation of yttrium into the scale suppressed the cation contribution to scale growth and therefore reduces oxide formation within the existing layer.

In the original model of Golightly et. al.(19) it was supposed that yttrium segregated in dislocation pipes or other short circuit diffusion paths for the outward diffusion of  $\text{Al}^{+3}$  ions, which could effectively block them. El-Aiat and Kroger(57) have presented an alternative explanation on the basis of conductivity measurements. As mentioned in the previous section, yttrium acts as a donor in alumina despite it being isovalent with aluminum presumably because of its large atomic volume. Being a donor in alumina, yttrium doping will reduce  $\text{Al}_i^{\bullet\bullet}$  but increase  $V_{\text{Al}}^{\bullet\bullet}$ . It has been suggested that because of its small solubility in alumina the donor activity of yttrium is limited, such that yttrium concentration in alumina is just enough to compensate the effect of  $\text{Fe}^{+2}$  acceptors in the scale (incorporated from the Fe base alloy) by reducing aluminum ion interstitials  $\text{Al}_i^{\bullet\bullet}$  without markedly increasing aluminum vacancies  $V_{\text{Al}}^{\bullet\bullet}$ . Suppression of aluminum ion diffusion by yttrium doping implies reduction in the growth rates of alumina scales. Decreases in growth rates of alumina do seem to occur with very small additions ( $< 0.05\%$ ) of active elements. However, as pointed out earlier, the growth rates of alumina, calculated(33,41) on the basis of grain boundary diffusivity of oxygen, were found consistent with the experimental parabolic rate constant for NiCrAl and CoCrAl alloys with and without active elements.

The convoluted scale morphology of alumina scales and scale detachment at temperature in the absence of yttrium can, however, be explained alternatively on the basis of weak scale/substrate adhesion as opposed to the lateral growth mechanism.

### 3.5.3 Graded Seal Mechanism

The graded seal mechanism is based on the supposition that a layer of oxide is developed between the scale and the alloy, which has a thermal expansion coefficient that gradually changes from the values similar to those of alloy to one similar to the scale as one proceeds through this layer from the alloy to the scale(59,60). Using a radioactive tracer method, Pfeiffer(60) showed that cerium accumulates at the alloy scale interface on Fe-Cr-Al-Ce alloys as a separate phase, and, as indicated, assumed it played the role of a buffer, attenuating the destructive action of thermal stresses.

Most other researchers(21,25,34) have failed to detect any such complete or even partial layer present between the substrate and scale. Giggins and Pettit(33) did not observe such a continuous layer but proposed the yttrium rich stringers and internal oxide particles may possess such properties, since their amounts increase as one proceeds from the alloy towards the  $\text{Al}_2\text{O}_3$  scale.

### 3.5.4 Chemical Bonding

This model is essentially based on the role of oxygen active elements in affecting the interfacial forces which are responsible for the oxide/metal adhesion. It has been proposed(7) that the oxygen active elements, such as yttrium, segregate at the oxide/metal interface and establishes a strong chemical bond across the interface because of their higher free energy of oxide formation as compared to that of base metal oxide. However, such a segregation has never been detected. This segregation may be limited to mono or biatomic layers at the interface which makes it difficult to detect by ordinary techniques.

This model however cannot explain the improved scale adherence obtained by the dispersion of  $\text{Al}_2\text{O}_3$  particles in an  $\text{Al}_2\text{O}_3$  scale forming alloy as observed by Tien and Pettit<sup>(21)</sup>. This effect can perhaps be explained better on the basis of the vacancy sink model which will be discussed in a subsequent section.

An alternative proposal also based on chemical effects, suggests that the oxygen active element or oxide addition in the alloy traps those impurities which are harmful for adherence such as sulfur. Recently, Funkenbush and Smeggil<sup>(61)</sup>, by using Auger analyses have found an enrichment of sulfur on the NiCrAl alloy surface at elevated temperature. They have proposed the segregation of sulfur at the scale/substrate interface in the absence of the active additions causes spalling and oxygen active elements prevent spalling by decreasing the availability of sulfur for segregation to the interface.

### 3.5.5 Vacancy Sink Mechanism

This model is based on the assumption that the formation of voids at the scale/substrate interface leads to the spalling of the scales. In undoped alloys the voids arise from the condensation of vacancies at the interface<sup>(21,56)</sup>. It was proposed that the internal oxide particles or the active element atoms themselves provide alternative sites for vacancy condensation<sup>(21,34,37,62)</sup> thus eliminating the interfacial porosity. This, in turn, helps to maintain scale-substrate contact and minimize scale spalling.

There has been considerable discussion in the past about the sources of excess vacancies leading to void formation. The scales such as CoO, FeO, and NiO which grow by the outward diffusion of cations, produce a countercurrent of vacancies which are injected into the metal at the scale/metal interface.  $\text{Al}_2\text{O}_3$  however, grows primarily by the inward diffusion of oxygen which cannot give rise to vacancy injection to the underlying alloy. Therefore the source of vacancies must be elsewhere.

It has been frequently suggested that the excess vacancies might arise from the Kirkendall effect associated with the selective oxidation of aluminum and the unbalanced flux of metal atoms near the scale/alloy interface<sup>(62)</sup>. In view of the slow growth rates of  $\text{Al}_2\text{O}_3$ , however, such a vacancy flux would be quite small<sup>(63)</sup>. Apparently large interfacial voids may be the result of stress assisted growth of initially nucleated small voids<sup>(21)</sup>. Their presence can also result in convoluted scale morphologies.

Another source of void formation pointed out<sup>(34)</sup> is vacancy injection during the transient oxidation period due to faster growing base metal oxides such as NiO, CoO, etc. Indeed, fewer voids have been observed<sup>(34)</sup> on NiCrAl or CoCrAl alloys oxidized in an atmosphere having oxygen pressure below that required to form NiO or CoO. On the contrary, in another study<sup>(64)</sup>, fewer voids have been observed on the  $\alpha$ -Co phase than on the  $\beta$ -CoAl alloy phase at the scale substrate interface in a CoCrAl alloy oxidized at 700 °C for only 1 hour. This result indicates that void formation is related to the selective oxidation of aluminum. Even more surprisingly, approximately the same amount of voids were observed with and without Y in the same study<sup>(64)</sup>. However, Y implantation seems to eliminate void formation. It must be pointed out that the above study dealt with  $\gamma$ - $\text{Al}_2\text{O}_3$ .

A third source of void formation is supposed to be related to the tensile stress in the alloy close to the scale/alloy interface. Voids may nucleate due to Hull and Rimmer creep in the alloy under tension<sup>(24)</sup>. Furthermore, relatively large local tensile stresses normal to the interface may arise due to waviness of the scale/substrate interface. This stress may exceed the critical void nucleation stress<sup>(17)</sup>.

There is no doubt that the presence of large interfacial voids would lower the adherence of the oxide scale but the question is whether the elimination of interfacial voids will ensure good adherence. There have been examples where few voids were present at the scale/substrate but the scale spalled profusely<sup>(33)</sup>.

Strong support for the vacancy sink model was provided by an experiment<sup>(21)</sup> where substantial improvement in the adherence of an  $\text{Al}_2\text{O}_3$  scale was observed on a FeCrAl alloy containing 2 vol.% of fine  $\text{Al}_2\text{O}_3$  particles without any addition of oxygen active elements. It was concluded that the dispersed  $\text{Al}_2\text{O}_3$  particles in the alloy act as vacancy sinks.

### 3.5.6 Mechanical Keying

It is proposed that the oxide protrusions which are developed at the scale substrate interface, due to the internal oxidation of oxygen active elements or dispersed oxide particles sitting at the scale substrate interface, provide a mechanical keying effect in improving adherence of the oxide scale to the substrate<sup>(21,34,49,65,66)</sup>. These oxide protrusions are commonly referred to as oxide pegs, since they are thought to serve the purpose of pegging the oxide scale to the substrate surface.

The adherence provided by these pegs is considered to be a function of their size, shape and distribution at the interface. A uniform and intense distribution of small oxide pegs is suggested to be the ultimate aim in achieving good oxide scale adherence<sup>(35)</sup>.

As discussed previously the morphology and distribution of oxide pegs is a function of the type, concentration, distribution and the state of the oxygen active element in the alloy, i.e., whether it is dissolved in the alloy or present as intermetallic compound, or dispersed as oxide particles in the alloy.

In general, the active elements such as Hf and Zr give rise to more numerous and uniformly distributed pegs as compared to the elements like Y or Ce. Because of this difference in the peg morphology, Allam et al.<sup>(34)</sup>, showed that Hf addition to a Co-10Cr-11Al alloy provides more resistance to  $\text{Al}_2\text{O}_3$  scale spalling than equivalent amounts of Y. They have also shown that the fine dispersion of the  $\text{HfO}_2$  in the alloy gives rise to more uniform distributions of smaller pegs which provided even better resistance to oxide spalling.

Giggins and Pettit<sup>(33)</sup> have identified two types of oxide pegs in Y containing NiCrAl and CoCrAl Al alloys: the macropegs which are developed at the sites where yttrium rich intermetallics are present in the alloy, and micropegs which are formed rather uniformly at the scale/substrate interface as a result of internal oxidation of dissolved yttrium in the alloy. Micropegs perhaps play a more



important role than the macropegs. Macropegs when grown extra large can actually induce scale spalling because of a stress concentration effect. Localized scale spalling in the neighborhood of large oxide pegs have been observed by several investigators<sup>(19,34)</sup>.

As with the other proposed models, improved scale adherence cannot be solely attributed to oxide pegging, since there are many examples where good adherence of oxide scale is observed in the absence of any oxide pegs at the scale/substrate interface. For instance when the elements such as Y or Ce were added below the solubility limit, no oxide pegs of any kind, not even internal oxide particles, have been detected but substantial improvements in the adherence were observed<sup>(19,21,45)</sup>. Similarly, Tien and Pettit<sup>(21)</sup> have found scandium rich oxide pegs completely incorporated in the  $\text{Al}_2\text{O}_3$  scale after 1000 hours of oxidation of FeCrAlSc, due to the inward growth of the  $\text{Al}_2\text{O}_3$  scale; still the scale adherence was quite good, however, not as good as for the thinner scales.

## 4.0 EXPERIMENTAL TECHNIQUES AND PROCEDURES

### 4.1 Acoustic Emission Technique

Acoustic emissions are transient elastic waves generated by the rapid release of energy as a result of changes in the local stress and strain fields within a material undergoing deformation, fracture or phase transformation processes. These transient waves are usually detected at the surface of the material by a piezoelectric transducer, which transforms the mechanical signal into an electrical signal. The shape of a transduced signal from an acoustic emission event is schematically shown in Figure 8. It consists of a damped sinusoid with a frequency corresponding approximately to the resonant frequency of the transducer<sup>(67)</sup>. The exponential decay of the signal may be expressed as follows:

$$V = V_0 e^{-\beta t} \sin(2\pi f t) \quad (11)$$

where  $f$  is the frequency of the transducer,  $\beta$  is a damping constant, and  $V_0$  is called the peak amplitude of the acoustic emission event. The transduced electrical signal is normally preamplified and filtered before further processing. In order to measure the intensity of acoustic emission during a given process or to ascertain certain information about the micromechanisms involved in the process, the acoustic emission signals can be processed in several different ways. The parameters measured in the present study of oxide scale failure processes were mainly acoustic emission counts and peak amplitude analysis of AE events. In the following a brief description of these parameters and their significance will be presented.

#### 4.1.1 Acoustic Emission Counts

Acoustic emission counts are by far the most commonly measured parameter. They are relatively easy to measure and provide an estimate of the intensity of acoustic emission activity in a given process. AE counts are measured by comparing the preamplified and filtered signal against a preset threshold voltage which is generally set just above the background noise level. The number of times this signal crosses the preset threshold level ( $V_t$  in Figure 8) before "ringing down" to a voltage below the trigger level is termed "ringdown" counts or simply AE counts. Three counts would result from the signal shown in Figure 8. The number of counts from a single event are related to its peak amplitude as follows:

$$n = (f/\beta) \ln(V_0/V_t) \quad (12)$$

The square of the peak amplitude is in turn related to the energy of the event. Consequently, the cumulative AE counts which is the sum of all counts resulting from various emissions in a given process, is a function of the elastic energy released. However, this number is influenced by the properties of the detector and by the geometry of the specimen. The latter effect is due to internal reflection of the elastic waves. In the present study the size of specimens was very small (12mm x 9mm x 2mm), the reflections are expected to be minimal. The size was also kept constant throughout the study. An alternative method of counting is to count the squared amplitudes of the signal to obtain a better measure of elastic energy released during a process. These counts may be termed energy counts. This

method was also employed in the present work; but the instrument used for this purpose has only 26 dBs dynamic range.

#### 4.1.2 Peak Amplitude Analysis

Peak amplitude is one of the several characteristics of acoustic emission events which can be related to the mechanism involved in their origin. The distribution of events with respect to their peak amplitudes can be used to determine the dominant mechanism involved in the process of deformation or cracking. Other methods to characterize emissions are: frequency, pulsewidth and rise-time distributions. These methods have not been used in the present work. Several good references<sup>(68-70)</sup> are available which describe the significance of these distributions.

During the course of a typical acoustic emission test, the peak amplitudes of individual emissions vary over several orders of magnitude. Two alternative functions may be used to describe the distribution of peak amplitudes<sup>(68)</sup>,  $N(V)$  and  $M(V)$ . The function  $N(V)$  may be defined as a fraction of events whose peak amplitude exceed a voltage  $V$ . The second function  $M(V)$  is the fraction of the emission population whose peak amplitude falls between  $V$  and  $(V + \Delta V)$ . The function  $N(V)$  is necessarily a monotonically decreasing function, whereas  $M(V)$  may show peaks if there is a tendency for emission amplitudes to cluster around particular values. It is found that the experimental data often approximate to a power law distribution of the form

$$N(V)/N(V_0) = (V/V_0)^{-b} \quad (13)$$

It is very convenient to describe whole distributions by specifying a single parameter  $b$ , whose value is uniquely related to the mechanism involved in the process.

However, when two distinct types of mechanisms are operating simultaneously it would be advantageous to use function  $M(V)$ . This is usually the case with an oxide scale failure process, where both spalling and cracking processes occur simultaneously. In a 'spalling' event the crack grows along the scale/substrate interface and is an adhesive failure. In a 'cracking' event the crack grows through the thickness of oxide scale and is a cohesive failure.

It has been hypothesized<sup>(71,72)</sup> that during a crack growth process, the peak amplitude  $V_0$  of an event depends on the incremental area swept out,  $\Delta A$ , and on the stress intensity at the crack tip,  $K$ .

$$V_0 \propto (\Delta A)^K \quad (14)$$

Dunegan/Endevco's Model 921 (Amplitude Detector) and Model 920A (Distribution Analyzer) were used for peak amplitude analysis of acoustic emission events during cooling of oxidized specimens. As the name implies, the Amplitude Detector detects the peak amplitude of the emissions and the Distribution Analyzer stores them in different memory slots according to their amplitudes.

In performing the peak amplitude analysis setting of DEAD TIME on the Model 920A is crucially important. DEAD TIME may be defined as the time duration between

when an emission signal has decayed below the threshold level and when Model 921 is ready to process a new event. Too short a DEAD TIME can cause a single event to be registered as multiple events depending upon the waveform shape of the event and how an event has been defined. Some time dependent event(s) are considered to be part of a parent event. Too long a DEAD TIME can cause separate consecutive events to be registered as a single event. Therefore, some prior knowledge of the waveform shape, duration and rate of occurrence of the event is necessary.

In the preliminary tests acoustic emission event rates up to 500/sec have been observed during the cooling of oxidized specimens depending on the cooling rate and the particular alloy. Event duration also varied widely from 100 microseconds to 10 milliseconds. A DEAD TIME setting of 100 microseconds was used for all the experiments. This was also the minimum selectable DEAD TIME. The minimum DEAD TIME setting was used so that a maximum number of events could be analyzed. The minimum setting was also needed to register cracking events which are usually immediately followed by a spalling event.

#### 4.1.3 Experimental Apparatus and Signal Processing

As mentioned earlier, acoustic signals (elastic waves) are usually detected at the surface of specimens by a piezoelectric transducer. However, no transducer is yet available which can withstand the high temperatures of interest (1100°C) in the current study. Therefore, a waveguide was used to transmit the acoustic signal from the specimen to the transducer, as shown schematically in Figure 9. The waveguide was one millimeter thick and about one meter long platinum wire which also served the purpose of hanging the specimen in the furnace tube. The specimen was attached to the waveguide with a fine spot weld. On the other end of the waveguide a stainless steel cone was permanently welded, to which the transducer was attached. Platinum was chosen since it does not oxidize under the experimental conditions used and does not undergo any phase transformations which could be a potential source of acoustic emission. The experimental arrangement also included a screw lift mechanism to remove the specimen from the furnace with a controlled speed and without introducing noise above the threshold level.

The acoustic emission monitoring system used, was the Dunegan/Endevco, 3000 series. The function block diagram of this system is shown in Figure 10. The acoustic emission signal is detected by a high sensitivity PZT transducer (Model S9204) which has a frequency response over a range of 100-400 KHz. The transduced signal is preamplified by a fixed gain of 40 dB (100 times) and passed through a 100 KHz highpass filter. The preamplified and filtered signal is then processed for count measurements and for amplitude analysis. For count measurement, the signal is further amplified and fed to a threshold detector which sends a digital pulse to a digital counter each time the signal exceeds the threshold voltage. The threshold voltage is fixed at one volt so the signal has to be amplified such that the noise level is just below one volt to obtain the maximum sensitivity. The digital counter accumulates all the pulses and displays them on a LED window as AE counts. The digital signal is also converted into an analog signal to plot the counts on a recorder. A reset clock may be used to reset the counter as programmed to plot the acoustic emission count rate. An Energy Processor (Model 602) which has a fairly limited dynamic range, 26 dB, provides an output proportional to the energy of the signal, which is derived from the square of the signal amplitude integrated over the period of its duration above a threshold level.

For peak amplitude analysis, the preamplified and filtered signal goes to the Amplitude Detector (Model 921). The amplitude detector first performs a logarithmic amplification, to obtain a wide dynamic range, and then detects the peak amplitude of individual events. A digital output proportional to the peak amplitude of the event is then sent to the distribution analyzer which stores the events in 101 slots, with an increment of 1 dB from 0 to 100 dB.

## 4.2 Materials

The alloys studied were nickel and cobalt base, with 20%\* chromium and 10% aluminum and varying amounts of yttrium and hafnium. One of each alloy was made with none of the active elements to serve as the control alloys. The nominal compositions of these alloys are given in Table I. The first column in the table has the alloy designations which will be referred to in the subsequent discussion. The yttrium and hafnium contents as determined by plasma arc and X-ray fluorescence methods are indicated in parentheses in the table. All the alloys were alumina scale formers and the compositions are typical of the MCrAlY alloys which are used for coating the components in the hot sections of gas turbine engines.

## 4.3 Alloy and Specimen Preparation

All of the alloys were prepared from high purity elements (> 99.9%) by tungsten arc melting, under an argon atmosphere, and drop casting into a copper mold of dimensions 300mm x 25mm x 9mm. The ingots were then annealed for 100 hours at 1150 °C to promote homogeneity in the cast structure. Specimens of dimensions 12mm x 9mm x 2mm were cut from the ingots, polished through 600 grit, and ultrasonically cleaned in alcohol prior to oxidation. The specimens used in the cyclic oxidation tests were twice as large in size, 24mm x 9mm x 2mm.

## 4.4 Experimental Procedures

### 4.4.1 AE Experiments

Two series of AE experiments were carried out. In the first series the specimens were isothermally oxidized for 24 hours at 1100°C and then cooled slowly inside the furnace, by switching the furnace off. In the other series, the specimens were cyclically oxidized. Each cycle consisted of 24 hours isothermal oxidation at 1100 °C followed by at least half an hour cooling, outside the furnace, in air. Acoustic emission data were obtained during isothermal periods as well as during cooling of the specimens. A total gain of 90 dB was used throughout the AE experiments. This value is about 3 dB lower than the gain at which the background noise in the system would reach the threshold level.

### 4.4.2 Thermogravimetric Tests

Two types of thermogravimetric tests were carried out; static oxidation weight gain tests, to study the oxidation kinetics, and cyclic oxidation weight change tests, to determine the long term cyclic oxidation resistance of the alloys. Both types of tests are commonly used in oxidation studies. In the static oxidation tests specimens were isothermally oxidized at 1100°C in flowing air (at flow rate of 1.5 cm/min) over a period of one week. The test temperature was controlled within  $\pm 2$  °C. A 'Cahn 2000' microbalance was used to record the weight of the specimen being oxidized.

---

\*All compositions are presented in weight percent.

Long term cyclic oxidation tests were carried out by cyclically oxidizing the specimens in an apparatus which automatically removed the specimens from the furnace and reinserted them. Each cycle consisted of 45 minutes isothermal oxidation followed by cooling for 15 minutes outside the furnace. The specimens were weighed after every 20 to 30 cycles. Before each weighing the loose oxide scale was removed from the specimen surface with the help of pressurized air. The net weight change of the specimen is, therefore, the weight gain due to oxidation minus the weight lost from oxide spalling.

#### 4.4.3 Mechanical Stripping of Oxide Scales

Mechanical stripping of oxide scales was accomplished by attaching an epoxy coated stud (1/16 in. dia.) to the surface of an oxidized specimen and applying a tensile load to the stud. Prior to the load application, the epoxy was cured by placing the specimen-stud assembly in an oven at 150 °C, for about an hour. The arrangement is schematically illustrated in Figure 11. The exposed surface of the substrate and the underside of the scale were analyzed by SEM and Auger electron spectroscopy. A 'Sebastian Coating Adherence Tester' was employed to apply the load on the stud. The stress at which failure occurs is displayed on the tester. The maximum load which can be applied is limited by the strength of epoxy, which is 10,000 psi. Scales on some alloys were found more strongly adherent than 10,000 psi. In those cases failure took place within the epoxy.

#### 4.4.4 Chemical Stripping of Oxide Scales

The oxides which were too strongly adherent to be pulled off mechanically were stripped from their substrates by dissolving the latter in a 10% bromine-methanol solution. This solution dissolves away the alloy without adversely affecting the oxide layer. Samples were prepared by oxidizing the specimens at 1100 °C for 48 hours and grinding the edges in order to expose the substrate to the solution to start the dissolution process.

Filtration of solvent and the extraction of oxide were performed under an exhaust hood with a filter disc (US millipore 0.25 micron pore size) which is inert to the solvent. The glass assembly was made by Millipore Corporation. The flakes of oxide remaining on the filter disc were washed with a freshly made 10% bromine-methanol solution and rewashed several times in methanol. The flakes were immersed in distilled water and collected on a TEM copper grid for SEM examination.

## 5. EXPERIMENTAL RESULTS

### 5.1 Microstructure of the Alloys

The chemical compositions of the alloys are given in Table I. The specimens for microstructural characterization were either prepared by polishing through 0.05 micron alumina and etching with a solution of glycerol, nitric acid and hydrochloric acid (60:25:15 by volume, respectively), or by heat tinting the polished specimens. The heat tinting technique, which involved heating the specimen for about five minutes at 600 °C in air, was particularly useful in identifying the active element rich phases. Both, optical and scanning electron microscopes were employed in the microstructural analysis. Energy dispersive and wave length dispersive X-ray analysis were used for phase identification.

The microstructures of all the nickel base alloys were very similar except for the size and the distribution of active element rich phases. This distribution varied with the type and concentration of the active element in the alloys. The grain structure of the ingots consisted of large columnar grains and a central equiaxed zone. The average primary dendrite arm spacing of the columnar grains was about 100  $\mu\text{m}$  and the average grain size in the central zone was about 50 to 60  $\mu\text{m}$ . A typical microstructure of a nickel base alloy is shown in Figure 12. It consists of primary dendrites of bcc  $\beta$  (NiAl) in a matrix of  $\gamma$  (NiCr) and  $\gamma'$  (Ni<sub>3</sub>Al). At higher magnification (Figure 13), fine precipitates of  $\gamma'$  in the  $\gamma$ -phase, globules of  $\alpha$ -chromium in the  $\beta$  phase and a layer of  $\gamma'$  at the  $\gamma + \gamma'/\beta$  phase boundary can be resolved. The phases identified above are the same as those found in the Ni-15Cr-24Al (at%) alloys used in a previous study<sup>(23)</sup>.

The three cobalt base alloys studied had very similar microstructures, but as a group their microstructures differed significantly from the nickel base alloys. The grain structures of the cobalt base ingots consisted of fine equiaxed grains of about 40-50  $\mu$ . Phase constituents were primary dendrites of  $\beta$  (CoAl) in the  $\alpha$  (CoCr) matrix as shown in Figure 14.

The exact solubility of yttrium in MCrAl type alloys is not known but it is believed to be very low, less than about 0.04 wt%<sup>(33)</sup>. Consequently no yttride phase (intermetallic compound of yttrium) was detected in the NiCrAl-0.02Y alloy. A few yttride particles were detected in the NiCrAl-0.2Y and CoCrAl-0.2Y alloys, (Figure 15). The yttride phase was a regular phase constituent in the NiCrAl-0.8Y alloy (Figure 16) and was most frequently associated with phase boundaries and the grain boundaries in the above alloys.

The solubility of hafnium in MCrAl type alloys is known to be relatively high<sup>(34)</sup>, between 1 and 1.5 %. Accordingly, no intermetallic compound of hafnium was detected in the nickel base alloys used in this study. A small fraction of hafnium-cobalt intermetallic phase was found in the CoCrAl-1.0Hf alloy, shown in Figure 17. Particles of hafnium oxide were however, detected in all three hafnium containing alloys. Figure 18 shows the hafnium oxide particles in the NiCrAl-1.0Hf alloy and the X-ray maps for hafnium and oxygen in that region. The hafnium oxide particles were finer and more numerous in NiCrAl-0.3Hf (Figure 19) than those in NiCrAl-1.0Hf or CoCrAl-1.0Hf.

## 5.2 Isothermal Oxidation Weight Gain Tests

To study the isothermal scale growth kinetics, specimens were oxidized isothermally for one week at 1100 °C in flowing air. The weight changes of the specimens were continuously recorded throughout the course of oxidation using a Cahn 2000 microbalance. The results of these experiments are shown in Figure 20. The square of the specific weight change  $(\Delta \text{wt}/\text{area})^2$ , versus time is plotted in Figure 21. The best fit straight lines are drawn through the data to approximate the parabolic kinetics. The parabolic rate constant,  $k_p$ , and the statistical variance are also indicated for each straight line.

After the initial transient oxidation period, the scale growth rate for both undoped specimens, NiCrAl and CoCrAl, appears to follow a parabolic rate law. The value of  $k_p$  for the NiCrAl specimen is slightly higher than that for the CoCrAl specimen. The scale growth kinetics for the NiCrAl-1.0Hf, NiCrAl-0.3Hf and CoCrAl-0.2Y also followed a parabolic rate law. However, the value of  $k_p$  for the NiCrAl-1.0Hf is larger than those for the undoped specimens and the values of  $k_p$  for the NiCrAl-0.3Hf and CoCrAl-0.2Y specimens are lower than those for undoped alloys. The data for the NiCrAl-0.8Y and NiCrAl-0.2Y could not be approximated to any definite parabolic rate. The other two doped specimens, NiCrAl-0.02Y and CoCrAl-1.0Hf deviate from parabolic kinetics during the later stages of oxidation.

## 5.3 Acoustic Emission Study of $\text{Al}_2\text{O}_3$ Scale Failure

The purpose of the acoustic emission (AE) study was to obtain both quantitative and qualitative information about the  $\text{Al}_2\text{O}_3$  scale failure process. Two sets of oxidation experiments were carried out. In the first set the specimens were isothermally oxidized for 24 hours and then allowed to cool in the furnace by switching the furnace off at the end of the isothermal oxidation period. Slow cooling of the specimens enabled closer monitoring of the scale failure process. In the second set of experiments the specimens were cyclically oxidized to study the scale damage as a function of the number of thermal cycles.

### 5.3.1 Short Term AE Experiments

To study the effect of yttrium and hafnium additions on the  $\text{Al}_2\text{O}_3$  scale failure in both the nickel and the cobalt base alloys, the following six specimens were used in this series of experiments: NiCrAl, NiCrAl-0.2Y, NiCrAl-1.0Hf, CoCrAl, CoCrAl-0.2Y and CoCrAl-1.0Hf.

#### Acoustic Emission Counts

No significant AE signals, which are indicators of scale failure, were detected during the isothermal oxidation of the specimens. The cumulative AE counts recorded during the cooling of the specimens are plotted as a function of time in Figures 22 and 23, for the nickel and cobalt base alloys, respectively. The cooling curves for the specimens are also shown in these figures. The total AE counts for the NiCrAl specimen were about an order of magnitude greater than those for the NiCrAl-0.2Y or for the NiCrAl-1.0Hf specimens. In cobalt base alloys the effect of doping was more pronounced. The specimens doped with either yttrium or hafnium had about two orders of magnitude fewer AE counts than the undoped CoCrAl specimens. The SEM micrographs of the surfaces of the specimens are shown in Figures 24 and 25. The  $\text{Al}_2\text{O}_3$  scale had completely spalled off the surface of the undoped NiCrAl specimen while only localized spalling occurred on the surfaces of yttrium or hafnium containing NiCrAl specimens (Figure 24). The undoped CoCrAl specimen also experienced severe scale damage but it was not as extensive as the spalling on the undoped NiCrAl specimen. No apparent scale



damage had occurred on the surface of the CoCrAl alloys doped with yttrium or hafnium. The AE counts from these specimens were in fact very small. The sources of this emission may be highly localized scale damage or the scale damage at the location where the specimens were welded to the platinum wire wave guide.

The number of AE counts seems to be clearly related to the amount of scale damage on the different specimens. A more exact relationship between the scale spalled area and the total number of AE counts will be developed subsequently.

#### Rate of Acoustic Emission

The rate of scale damage as a function of temperature during cooling is an important parameter in studying and comparing the scale failure process in different alloys. The acoustic emission count rate (AE counts/deg. C) was used to obtain this type of information. The AE count rate during the cooling of an undoped NiCrAl specimen accelerated rapidly at approximately 650 °C and reached its maximum at roughly 400 °C before decreasing. This behavior is shown in Figure 26. Conversely, the count rates of doped NiCrAl specimens rose gradually during the entire cooling period. Although it is not shown in Figure 26, the count rate eventually drops off with time, after the specimens have been cooled to room temperature. Thus the data in Figure 26 indicate that most of the scale damage on the undoped NiCrAl specimen occurred earlier in the cooling process, i.e., at higher temperature, while most of the scale damage on the doped NiCrAl alloy took place at lower temperatures during cooling. Similar trends in AE count rates can be seen in cobalt base alloys, shown in Figure 27. However, due to the low magnitude of counts from the doped CoCrAl alloys the increase in the count rate during cooling is barely noticeable in the plot shown in Figure 27.

#### Peak Amplitude Analysis

Amplitude analysis of the acoustic emission events was also carried out. The distributions of the events with respect to their peak amplitude for various alloys tested in this series of experiments are given in Figures 28 and 29. In these figures, the number of AE events are plotted as a function of their peak amplitude. A log scale is used for the number of AE events and the peak amplitudes are given in dBs which is also proportional to the log of the peak amplitude. No events below 30 dBs are shown in the figures because 30 dBs was the preset threshold for peak amplitude detection.

Not only the number of AE events but also the ranges of peak amplitudes were greater for undoped alloys than the corresponding doped alloys. The greater number of AE events can be expected from the more extensive scale damage on the undoped alloys. The greater number of high amplitude events indicate that the failure of  $Al_2O_3$  scale on these specimens may be occurring in large steps. Another noticeable feature of the distributions for the undoped specimens is the pronounced change in the slope of the curves at about 40 dBs.

#### 5.3.2. Cyclic Oxidation AE Tests

These tests were performed to compare the cyclic oxidation resistance of the nickel and cobalt base alloys containing varying amounts of yttrium and hafnium, and to study the scale failure process as cyclic oxidation progresses. In these experiments the specimens were cyclically oxidized. Each cycle consisted of 24 hours isothermal oxidation followed by a minimum of twenty minutes cooling in

ambient air. All the alloys containing the active elements listed in Table I, were tested in this series of experiments. Most of these tests consisted of six thermal cycles.

#### Acoustic Emission Counts

The total number of AE counts recorded during each cooling cycle are plotted as a function of the number of cooling cycles in Figure 30. There was a general trend towards an increase in the number of AE counts as the number of cycles increased. However, there were a few exceptions to this trend. The rate of increase in the counts, as a function of number of cycles, was dependent on the individual alloy. For example, the number of AE counts for NiCrAl-0.8Y and NiCrAl-1.0Hf specimens increased by more than an order of magnitude as the number of cycles increased from one to six, whereas, the increase in the counts for NiCrAl-0.2Y or NiCrAl-0.02Y specimens was not as large. In the case of CoCrAl-0.2Y or CoCrAl-1.0Hf specimen the increases in the counts were barely significant. The behavior of the NiCrAl-0.3Hf specimen was quite anomalous. After the initial increase in counts between the first cycle and the second cycle, the number of AE counts declined as the number of cooling cycles progressed.

Using AE counts as an indicator of scale damage, it appears that the CoCrAl-0.2Y and CoCrAl-1.0Hf specimens have the best cyclic oxidation resistance. However, the difference between the two alloys is not obvious. Perhaps longer thermal cycling is needed to make a clear distinction. The next best were the NiCrAl-0.2Y and NiCrAl-0.02Y alloys. The difference between these two is not large but it is consistent and the NiCrAl-0.2Y seems to be better than the NiCrAl-0.02Y. The worst perhaps are the NiCrAl-0.8Y and NiCrAl-0.3Hf. Although the AE counts were lower for NiCrAl-0.3Hf than for the NiCrAl-0.8Y during the latter stages of thermal cycling, the scale was observed to be completely spalled off from the surface of the NiCrAl-0.3Hf specimen as early as the second cooling cycle.

After the thermal cycling experiments, the surfaces of the specimens were analyzed by SEM. Figure 30 shows some of the SEM micrographs obtained during this analysis. The scale was severely damaged on the NiCrAl-0.8Y and NiCrAl-0.3Hf, and relatively less so, on the NiCrAl-1.0Hf specimen, but it was generally adherent on the NiCrAl-0.2Y and NiCrAl-0.02Y specimens, except for a few small isolated spalled areas. No spalling, however, could be detected on the CoCrAl-1.0Hf and CoCrAl-0.2Y specimens.

#### Amplitude Analysis

The peak amplitude distributions of the AE events, generated during each cooling cycle, for the various specimens are given in Figures 32-38. While there were only marginal differences in the distributions for different cooling cycles for a given specimen, there were significant differences in the distributions for the different alloys. In other words, each specimen had a characteristic distribution of the peak amplitudes which changed only slightly with the number of thermal cycles. This suggests that the oxide scale failure process may be characteristically different in different alloys. An attempt will be made to correlate these peak amplitude distributions with the morphologies of the scale/substrate interfaces in the various alloys used in this series of experiments.

#### 5.4 Cyclic Oxidation Weight Change Tests

The results of the AE experiments and the post analyses of the oxidized specimens by SEM have provided a general idea about the cyclic oxidation resistance of nickel and cobalt base alloys used in the present study. The long term cyclic oxidation weight change tests were conducted to compare the cyclic oxidation resistance of these alloys more rigorously by using a conventional test. The five alloys tested in this series of experiments, are those which had superior performance in the previous series of cyclic tests, namely, CoCrAl-0.2Y, CoCrAl-1.0Hf, NiCrAl-0.2Y, NiCrAl-0.02Y, and NiCrAl-1.0Hf. In the long term experiments each cycle consisted of 45 minutes of isothermal oxidation at 1100 °C followed by 15 minutes of cooling outside the furnace. The specimens were weighed periodically and the weight change in each specimen was then plotted as a function of the number of cycles. These results are given in Figure 39.

While the cobalt base specimens continued to gain weight throughout the entire thermal cycling, the nickel base specimens, after an initial weight gain eventually showed a net weight loss. The CoCrAl-1.0Hf specimen had relatively larger weight gain than the CoCrAl-0.2Y specimen. The total weight lost in the NiCrAl-1.0Hf specimen was significantly greater than the weight loss in the other two nickel base specimens. The difference in weight loss between the latter two nickel base specimens was in fact very small. The NiCrAl-0.02Y had relatively higher weight loss during cycling than the NiCrAl-0.2Y. It should be noted that the above trends in the weight changes of the different specimens, are in good agreement with the previous results of the scale damage using the AE measurements in a relatively short term thermal cycling test.

At the end of the 1000 hours of thermal cycling the specimens were analyzed by SEM. The scales on the nickel base alloys were severely damaged and consisted of several layers, as shown in Figure 40. Some of these layers were richer in chromium than the others. The chromium rich layers may have been formed during the latter stages of thermal cycling when the specimens became depleted in aluminum. The scales on the cobalt base specimens were single layered and not nearly as damaged as were those on the nickel base specimens. Only localized scale damage was observed on the cobalt base specimens, as can be seen in the SEM micrographs in Figure 41.

The cobalt base alloys containing active elements have consistently shown better performance under the previous experiments than the corresponding nickel base alloys. Therefore, weight change cyclic oxidation tests were also performed on the undoped NiCrAl and CoCrAl specimens to determine if the CoCrAl alloy is inherently better than the NiCrAl alloy or if the active elements are more effective in the CoCrAl alloy. The results of these tests are plotted in Figure 42. Both specimens lost excessive weight in the beginning of the tests due to excessive  $\text{Al}_2\text{O}_3$  scale spallation. However, the initial weight lost in the CoCrAl specimen was less than that for the NiCrAl specimen. After an initial weight loss, both specimens started gaining weight. This may be due to the formation of the faster growing oxides such as NiO and CoO. The presence of these oxides was apparent from the changes in the color of the specimens.

After about 300 cycles very large weight losses had occurred in the NiCrAl specimen due to the spallation of the thick NiO. Although the CoCrAl specimen continued to gain weight it had developed large cracks. The NiCrAl specimen had severely warped. At this point the thermal cycling was stopped. Looking at the weight change data one might get the impression that the CoCrAl alloy was significantly better than the NiCrAl alloy but both the specimens looked equally poor at the end of the above test.

### 5.5 Mechanical and Chemical Stripping of $\text{Al}_2\text{O}_3$ Scales

The mechanical oxide stripping test was designed to serve a dual purpose. The first purpose was to measure the adherence of oxide scales in terms of the tensile load required to pull the scale from the substrate and the second purpose was to have both sides of the scale and the substrate available for SEM examination. The substrates on which scales were too adherent to be pulled off mechanically were dissolved in a 10% Bromine Methanol solution, and the undissolved flakes of scale were then collected for SEM analyses. The specimens were prepared for oxide stripping by isothermal oxidation for 48 hours.

The oxidation conditions were chosen to produce a well developed  $\text{Al}_2\text{O}_3$  scale which would not spall excessively during the subsequent cooling. The loads required to pull the  $\text{Al}_2\text{O}_3$  scales from the NiCrAl-0.02Y, NiCrAl-0.2Y, NiCrAl-0.8Y and NiCrAl-0.3Hf substrates were 8.45, 9.46, 10.1 and 9.67 ksi, respectively. The exposed surfaces of the  $\text{Al}_2\text{O}_3$  scales and the corresponding exposed areas on the substrate are shown in Figures 43-46. The fine  $\text{Al}_2\text{O}_3$  grain imprints on the substrate surfaces indicate intimate contact between the scale and substrate prior to failure at the interface as a result of oxide stripping.

The microscopic features of the exposed surfaces in the NiCrAl-0.02Y and NiCrAl-0.2Y specimen were very similar (Figures 43 and 44). They were relatively flat and did not contain any oxide protrusions such as those present on the undersides of the  $\text{Al}_2\text{O}_3$  scales removed from the NiCrAl-0.8Y and NiCrAl-0.3Hf substrates. These oxide protrusions, which are generally termed, 'oxide pegs', were rich in yttrium or hafnium depending upon the dopant used in the alloy. These pegs were fairly large in size in the NiCrAl-0.8Y specimen. Some of the pegs in this specimen were even pulled away with the scale, leaving behind large pits in the substrate (Figure 45). The oxide pegs in the NiCrAl-0.3Hf were not as large and varied in size.

The scales on the CoCrAl-1.0Hf, CoCrAl-0.2Y and NiCrAl-1.0Hf substrates were too strongly adherent to be pulled off mechanically. The undersides of the  $\text{Al}_2\text{O}_3$  scales, obtained by dissolving the CoCrAl-0.2Y and CoCrAl-1.0Hf substrates, are shown in Figure 47. The scale from the CoCrAl-0.2Y specimen had features very similar to those found on the scale from the NiCrAl-0.2Y specimen. Both scales were very flat and contained a few yttrium oxide particles. However, the underside of the scale from the CoCrAl-1.0Hf specimen was quite different. It had an intense network of hafnium oxide pegs (Figure 47b).

The chemical stripping technique was not successful in obtaining  $\text{Al}_2\text{O}_3$  flakes from the NiCrAl-1.0Hf specimen. Although the substrate was successfully dissolved, the remaining  $\text{Al}_2\text{O}_3$  flakes were too small to be handled. However, an area exposed at the surface of NiCrAl-1.0Hf specimen as a result of scale spallation is shown in Figure 48. Numerous hafnium oxide pegs can be seen in this area.

## 6. DISCUSSION OF RESULTS

In discussing the results isothermal oxidation will be considered first and then the mechanical failure of oxide scales under the influence of thermally induced stresses. The cyclic oxidation behavior of alloys and the effects of oxygen active elements will then be considered.

### 6.1 Isothermal Oxidation Behavior

#### 6.1.1 $\text{Al}_2\text{O}_3$ Scale Growth Kinetics

The differences in the rates of scale growth on various alloys were not large, mainly, because all the alloys used were  $\text{Al}_2\text{O}_3$  scale formers. The parabolic rate constants  $K_p$ 's, for the alloys which followed a parabolic rate law, were in good agreement with previous studies<sup>(28,38)</sup> on  $\text{Al}_2\text{O}_3$  former alloys. Although the differences in growth rates of  $\text{Al}_2\text{O}_3$  on the various alloys were small, and it may not be justifiable to attach any significance to these differences, the rate of scale growth on the alloys containing relatively smaller amounts of yttrium or hafnium, such as NiCrAl-0.02Y, NiCrAl-0.2Y, NiCrAl-0.3Hf and CoCrAl-0.2Y, seems to be smaller than the undoped alloys. On the other hand, the scale growth rates, on the alloys containing relatively larger amounts of yttrium or hafnium, such as NiCrAl-0.8Y, NiCrAl-1.0Hf, and CoCrAl-1.0Hf, were greater than the undoped alloys.

These observed effects of the oxygen active element additions are consistent with previous studies<sup>(19,34,45)</sup> where decreases in  $\text{Al}_2\text{O}_3$  scale growth rate were observed at first with small additions of active element but as the amount of the additions were increased larger weight gains were observed. The increase in weight gain during oxidation of alloys containing relatively higher amounts of active elements can be explained on the basis of the development of oxide pegs at the scale/substrate interface, which when partially or completely incorporated in the inwardly growing  $\text{Al}_2\text{O}_3$  scale provide rapid diffusion paths through the scale since diffusion takes place more rapidly through the active element oxides compared to  $\text{Al}_2\text{O}_3$ .

The lowering of growth rate of  $\text{Al}_2\text{O}_3$  by the addition of yttrium can be attributed to the alteration of the defect structure in  $\text{Al}_2\text{O}_3$ <sup>(19,57)</sup>. The models proposed by Golightly et. al.<sup>(19)</sup> and El-Aiat and Kroger<sup>(57)</sup> have already been discussed in this regard.

#### 6.1.2 Scale/Substrate Interface Morphologies

Figure 49 shows an SEM micrograph of the surface of an undoped NiCrAl specimen, oxidized for one week. The wrinkled  $\text{Al}_2\text{O}_3$  scale and the smooth areas on the substrate indicate a partial loss of contact between the scale and the substrate during the isothermal oxidation period. The NiCrAl specimen which was oxidized for a relatively short time, 24 hours, developed an undulated scale/substrate interface but did not show any sign of the loss of scale-substrate contact at temperature. In fact, a good match between the underside of the spalled  $\text{Al}_2\text{O}_3$  scale and the exposed substrate, as shown in Figure 50, indicate intimate contact prior to spallation. The undulated scale/substrate interface may have resulted from plastic deformation of the substrate under the influence of the growth stresses in the  $\text{Al}_2\text{O}_3$  scale, as has been proposed by Golightly et. al.<sup>(19)</sup>.

Loss of scale-substrate contact for longer exposure times may have occurred by the stress assisted growth of interfacial voids<sup>(21)</sup>. The wrinkling of the  $\text{Al}_2\text{O}_3$  scale on the surface of the undoped CoCrAl specimen was considerably less than that on the corresponding NiCrAl specimen, as can be seen in Figure 51. Areas on the CoCrAl at which the scale was not in contact with the substrate, however, can also be seen. The  $\text{Al}_2\text{O}_3$  scale on the CoCrAl alloy contained a significant amount of cobalt and chromium rich oxides.

The  $\text{Al}_2\text{O}_3$  scales developed on the NiCrAl and CoCrAl alloys doped with yttrium or hafnium were relatively flat and nonwrinkled. Figure 52 shows the scale/gas interface of the NiCrAl-0.02Y and CoCrAl-0.2Y specimens which were oxidized for one week. As in the case of undoped specimens the doped CoCrAl specimens also contained a significant amount of Co and Cr rich transient oxides. These oxides were found to be associated with grain boundaries in the substrate.

In Figure 53 photographs showing transverse sections of some oxidized specimens are presented. The scale/substrate interfaces in the NiCrAl-0.02Y, NiCrAl-0.2Y and CoCrAl-0.2Y specimens were flat and did not have any oxide pegs. The oxide pegs were, however, present at the scale/substrate interface in the NiCrAl-0.8Y, NiCrAl-0.3Hf, NiCrAl-1.0Hf and CoCrAl-1.0Hf specimens. The size and distribution of these pegs were different in each alloy. They were much more numerous in NiCrAl-1.0Hf and CoCrAl-1.0Hf than in either NiCrAl-0.8Y or NiCrAl-0.3Hf. The microprobe analyses of these pegs showed that the central cores were composed of oxides of the active element in the alloy and these cores were surrounded by or coated with  $\text{Al}_2\text{O}_3$ . The results of the microprobe analyses for CoCrAl-1.0Hf and NiCrAl-0.8Y are presented in Figures 54 and 55, respectively. The formation of these pegs will be discussed in the following section.

### 6.1.3 Oxidation of Oxygen Active Elements

With the exception of NiCrAl-0.02Y specimens, the oxides of oxygen active elements have been detected at or near the scale/substrate interfaces in all the oxidized specimens doped with hafnium or yttrium. The number, size, shape and distributions of these oxide phases were found to be a function of the type, concentration and the state of the active element present in the alloy prior to oxidation.

The differences in the morphological features of the scale/substrate interfaces in the yttrium and hafnium containing alloys can be related to the difference in the solubilities of yttrium and hafnium in the alloys. The solubility of yttrium, as found in this study and elsewhere<sup>(33,45)</sup> was quite low, perhaps less than 0.04%. On the other hand hafnium was found to be soluble up to about 1%. However, a fraction of the added hafnium oxidized during the fabrication of the alloys.

#### 6.1.3.1 Oxidation of Yttrium

As mentioned previously no yttrium oxide particles were detected at or near the scale/substrate interface in the NiCrAl-0.02Y specimen. The yttrium content of this alloy was much below the solubility limit of yttrium. Previous studies<sup>(19,45)</sup> on the alloys containing yttrium less than its solubility limit have also failed to detect oxides of yttrium in the oxidized specimens. Yttrium oxide phases, however, have been commonly observed at the scale/substrate interface in alloys which contained yttrium above its solubility limit. There seems to be a correlation between the distributions of the intermetallic yttride phases in the alloys prior to oxidation and

the yttrium oxide phases in the oxidized specimens. For instance, the NiCrAl-0.2Y and CoCrAl-0.2Y alloys, which contained a widely distributed yttride phase, had only a few yttrium oxide particles at the scale/substrate interface (Figures 44 and 47a). The NiCrAl-0.8Y alloy which contained a relatively large fraction of yttride phase generated a large number of yttrium oxide pegs at the scale/substrate interface upon oxidation (Figures 44 and 53b).

The above observations suggest that the internal oxidation of yttrium is perhaps limited to the yttride phases and internal oxidation of the dissolved yttrium does not take place, even though, because of its higher affinity for oxygen as compared to the affinity of aluminum for oxygen, one would expect to observe internal oxidation of yttrium ahead of the  $\text{Al}_2\text{O}_3$  scale front. Another possibility is, that the dissolved yttrium does get internally oxidized but the particles are too small to be resolved by SEM. The smaller size of particles formed by internal oxidation is favored by the lower concentration and lower diffusivity of an internally oxidizing element. No data are available on the diffusivity of yttrium in MCrAlY type alloys but because of its large atomic size it is expected to be low.

The internal oxidation of dissolved yttrium ahead of an inward growing  $\text{Al}_2\text{O}_3$  scale front may occur by reaction with dissolved oxygen,



Incorporating the activity coefficients in the equilibrium constant, the equilibrium constant for the above reaction may be written as follows:

$$K = [\text{Y}_2\text{O}_3]/[\text{Y}]^2[\text{O}]^3 \quad (16)$$

For the internal oxidation of yttrium a critical solubility product,  $[\text{Y}]^2[\text{O}]^3$ , is required to nucleate  $\text{Y}_2\text{O}_3$  particles. Apparently this critical solubility product is not reached in the yttrium doped alloys because of the low solubility of yttrium in the alloy and the extremely small partial pressures of oxygen at the  $\text{Al}_2\text{O}_3$ /alloy interface. The latter controls the dissolution of oxygen at the scale/substrate interface and is affected by aluminum concentration in the alloy.

If it is assumed that the internal oxidation of the dissolved yttrium does not occur ahead of the inward growing  $\text{Al}_2\text{O}_3$  scale front, then the question is: what happens as the yttrium atoms in the alloy encounter the inwardly moving  $\text{Al}_2\text{O}_3$ /alloy interface? At the interface the following reaction may take place if it is assumed that  $\text{Al}_2\text{O}_3$  and  $\text{Y}_2\text{O}_3$  are the only stable oxide phases :



Using the mass action law with reaction 17 the activity of yttrium in the alloy must be equal to or greater than the following quantity

$$a_{\text{Y}} \geq \left[ \frac{a_{\text{Y}_2\text{O}_3} a_{\text{Al}}^2}{a_{\text{Al}_2\text{O}_3} K} \right]^{1/2}$$

or

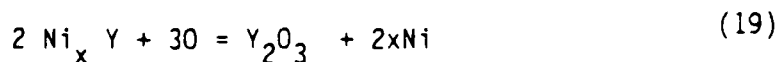
$$a_Y \geq \left[ \frac{a_{Y_2O_3} a_{Al}^2}{a_{Al_2O_3} \exp - \left( \frac{\Delta G_{Y_2O_3}^0 - \Delta G_{Al_2O_3}^0}{RT} \right)} \right]^{1/2} \quad (18)$$

to be incorporated in the  $Al_2O_3$  scale. On the other hand if the activity of yttrium in the alloy is less than the above, yttrium will not be oxidized, instead it will enrich at the  $Al_2O_3$ /alloy interface. One would then expect to see precipitated yttride phase provided the yttride forms at a lower activity than that required to form  $Y_2O_3$ . Equation (18) predicts that higher activity of aluminum (in the alloy) and higher activity of  $Y_2O_3$  (in  $Al_2O_3$  scale), will require a higher activity of yttrium in the alloy for its oxidation. In other words a smaller concentration of aluminum and higher solubility of  $Y_2O_3$  in  $Al_2O_3$  will promote the oxidation of yttrium at the  $Al_2O_3$ /alloy interface.

#### Oxidation of Yttride Phase

The yttrium oxide particles which were observed in the NiCrAl-0.2Y (Figure 43) and the yttrium oxide pegs which were observed in the NiCrAl-0.8Y specimen (Figure 44) must have formed by the oxidation of the yttride phases present in the alloys prior to oxidation, since a correlation was found between the distributions of the two. The steps involved in the development of the scale/substrate interface morphology in a specimen containing yttride phases are schematically shown in Figure 56. Although yttride phases usually tend to segregate at the grain boundaries (or at the phase boundaries), as shown in the figure at location 1 and 3, for the sake of completeness oxidation of a yttride precipitate away from these boundaries is also shown in the figure at location 2.

As the alloy is exposed to an oxidizing atmosphere such as air, not only the yttride phases at the alloy surface will oxidize, but the oxygen partial pressure will be high enough, even to oxidize yttrium in solution despite its low activity in the alloy. Consequently fine nuclei of  $Y_2O_3$  will form all over the surface of the alloy (Figure 56b). Oxides of other elements such as Cr, Ni, or Co will also form depending upon the alloy's composition. For the sake of simplicity only the  $Al_2O_3$  and  $Y_2O_3$  are shown in Figure 56b. As the oxidation proceeds, due to the selective oxidation process only the  $Al_2O_3$  will continue to grow. A continuous layer of  $Al_2O_3$  will develop at the alloy surface except at the locations where yttride precipitates are present (Figure 56c). Since the  $Al_2O_3$  scale grows inward, the fine nuclei of  $Y_2O_3$  which were formed from the oxidation of dissolved yttrium will remain confined to the  $Al_2O_3$ /gas interface. On the other hand the  $Y_2O_3$  formed due to oxidation of yttride precipitates will also grow inward by the inward diffusion of oxygen through the  $Y_2O_3$ . Suppose, the yttride is the  $Ni_xY$  type, the following reaction at the  $Ni_xY/Y_2O_3$  interface can be considered.



The freed nickel either forms a buffer between  $Ni_xY$  and  $Y_2O_3$  or may diffuse away from the reaction zone into the alloy matrix. If a buffer zone forms the yttrium has to diffuse through this buffer zone for further reaction. A buffer zone rich in nickel (and chromium) has been observed by Giggins and Pettit<sup>(33)</sup> in oxidized NiCrAl-3.0Y specimens. No such buffer zone has been observed in the



NiCrAl-0.8Y specimens in the present study. After the complete oxidation of the yttride phase at location 2 the growth of  $Y_2O_3$  will stop since a sufficient flux of yttrium can not be maintained at this location. However, at the grain boundaries the flux of yttrium can be maintained from the decomposition of the next yttride precipitate along the grain boundary.

The formation of  $Al_2O_3$  around the  $Y_2O_3$  stringer as observed in the NiCrAl-0.8Y specimen (Figure 55) can be explained on the basis of enhanced diffusivity of oxygen through the  $Y_2O_3$ . Faster diffusion of oxygen has also been reported in the oxides of other oxygen active elements such as Zr and Hf<sup>(73)</sup>. The oxygen diffusing inward through the  $Y_2O_3$  reacts with the outward diffusing aluminum in the outer layer of the alloy, which results in the formation of  $Al_2O_3$  around the yttrium oxide stringer (Figure 56d). At location 2 yttrium oxide pegs will be completely surrounded by  $Al_2O_3$  since the growth of the  $Y_2O_3$  peg has already been stopped. Since the pegs at location 1 and 3 are still growing, only a sleeve of  $Al_2O_3$  will develop around the pegs.

In the alloys, which contain only a small fraction of yttride phase, a sufficient flux of yttrium may not be maintained for a long time even at the grain boundaries. Consequently, the pegs will not be able to grow much deeper into the alloy before they will be completely surrounded by the  $Al_2O_3$ . The NiCrAl-0.2Y and CoCrAl-0.2Y alloys in the present study are an example of such a condition. The yttride particles were so small and widely spaced in this alloy, that after the oxidation of an individual particle it did not have a chance to grow to form a deeper oxide peg in the alloy.

#### 6.1.3.2 Oxidation of Hafnium

Unlike the yttrium oxide pegs, the hafnium oxide pegs (Figures 53c-53e) were not the direct result of the oxidation of intermetallic hafnium, since these pegs were observed in the alloys (NiCrAl-0.3Hf and NiCrAl-1.0Hf) which did not even contain any hafnium intermetallic phase prior to the oxidation. The CoCrAl-1.0Hf alloy did contain a small fraction of hafnium intermetallic phase, but the density of this phase was too small to account for the generation of all the hafnium oxide pegs observed at the scale/substrate interface (Figure 53d). Therefore the formation of hafnium oxide pegs must involve the oxidation of dissolved hafnium in the alloy. The pegs were much more numerous in NiCrAl-1.0Hf and in CoCrAl-1.0Hf alloys as compared to NiCrAl-0.3Hf alloy. The reason may be, the much smaller amount of hafnium in solution in the latter alloy. Previous studies have also shown that the alloys which contained higher amounts of hafnium (~ 1%) had a high density of oxide pegs at the interface upon oxidation and the alloys which contained relatively smaller amounts of hafnium had very few or no hafnium oxide pegs<sup>(34)</sup>.

The development of hafnium oxide pegs in the alloys such as NiCrAl-1.0Hf or CoCrAl-1.0Hf may be schematically represented by Figure 57. Unlike the  $Y_2O_3$ , the  $HfO_2$  nuclei which formed upon the first exposure of the alloy to the oxidizing atmosphere, are not completely out grown by the  $Al_2O_3$ . The  $Al_2O_3$  scale surrounds the  $HfO_2$  nuclei on the alloy surface but they continue to grow inwardly, since a sufficient flux of hafnium can be maintained towards these nuclei. Due to the faster diffusion of oxygen through the  $HfO_2$ , these pegs also grow much deeper in the alloy ahead of the  $Al_2O_3$  scale front and for the same reason growth of  $Al_2O_3$  occurs around them. The hafnium oxide pegs will continue to grow deeper into the alloy until the alloy becomes depleted of hafnium. The pegs will then become completely coated with  $Al_2O_3$ .

### 6.1.3.3 Oxidation of Other Oxygen Active Elements

The correlation between the solubility of an oxygen active element in an MCrAl type alloy and its oxidation behavior is not limited to yttrium and hafnium. A thorough literature search indicates that the other commonly used oxygen active elements seem to follow the same relationship. For instance, Zr and Sc, which have relatively high solubilities in MCrAl type alloys, when added close to their solubility limit, give rise to large number of oxide pegs at the scale/substrate interface quite similar to that of  $\text{HfO}_2$  pegs in the present study<sup>(21,74)</sup>. On the other hand, Ce and Th which have very low solubilities act much the same way as yttrium does. No internal oxidation of these elements was observed at or near the scale/substrate interface, except at the locations where intermetallic compounds of these elements were present in the alloys prior to oxidation<sup>(46,58)</sup>.

Based on their solubilities the different oxygen active elements, therefore, can be divided into two groups; those which have less than about 0.05 wt% solubility and those which are soluble up to about 1 wt% in the MCrAl type alloys. The first group includes yttrium, cerium, lanthanum and thorium; and the second group includes hafnium, scandium, and zirconium. The above classification of the active elements can also be made on the basis of their atomic sizes. This is not surprising since the solubility of an atom is a function of its size. Yttrium, cerium, thorium and lanthanum have large atomic radii, between 1.78 and 1.87 Å, while hafnium, zirconium, and scandium have relatively small atomic radii, between 1.6 and 1.67 Å.

## 6.2 Mechanical Failure of $\text{Al}_2\text{O}_3$ Scale

The theoretical aspects of stress development and of scale failure under these stresses have been discussed previously in this report. Experimental results involved with the failure of alumina scales will now be considered. An emphasis will be placed on the effect of oxygen active element additions on the scale failure processes. The effects of scale/substrate interface morphology will also be discussed.

### 6.2.1 Isothermal Scale Damage

The cracking of oxide scales during isothermal oxidation due to growth stresses has been reported in many studies<sup>(19,75,76)</sup>. Golightly et. al.<sup>(19)</sup> have proposed that the loss of  $\text{Al}_2\text{O}_3$  scale adhesion occurs at temperature due to excessive growth stresses in the undoped FeCrAl alloys. However, no significant acoustic emissions were generated during the isothermal oxidation of doped or undoped alloys in the AE experiments, in the present study, which could be attributed to the scale damage at temperature. The post analyses of the specimens also failed to indicate any signs of scale damage during the isothermal oxidation periods. However, the NiCrAl and CoCrAl specimens oxidized for one week in the weight gain experiments did show smooth areas on the substrate surface (Figures 49 and 51) indicating scale separation at temperature.

To attempt to detect this scale/substrate interface failure at temperature, one specimen of NiCrAl was oxidized for one week in an AE test. Again no emission was detected which could be attributed to the mechanical failure of the scale. As mentioned earlier, separation of the  $\text{Al}_2\text{O}_3$  scale may take place during isothermal oxidation by the stress assisted growth of interfacial voids, which is a combined effect of vacancy condensation and the growth stresses in the scale. Such a process

of void growth would be slow, perhaps atom by atom, and no sudden release of elastic energy in that case may be expected. Consequently, no acoustic emissions are generated during the separation of  $\text{Al}_2\text{O}_3$  scale from the substrate at temperature.

#### 6.2.2 $\text{Al}_2\text{O}_3$ Scale Failure During Cooling

The results of AE experiments and subsequent SEM analyses of the surfaces of the oxidized specimens, have shown much more scale damage on the undoped nickel and cobalt base alloys, as compared to the alloys which were doped either with yttrium or with hafnium. This was in agreement with the commonly known phenomenon of improved scale adherence due to the addition of such oxygen active elements. However, in the present study the active element containing cobalt base alloys were found significantly better than the corresponding nickel base alloys. The reasons for this difference between the cobalt and nickel base alloys are not quite clear. Attention will be focused on the effects of yttrium and hafnium on the  $\text{Al}_2\text{O}_3$  scale failure process and the adherence.

#### 6.2.3 Scale Damage as a Function of Temperature

One of the main purposes of using the AE technique was to obtain insitu information about the scale failure process. The AE count rate was used to measure the instantaneous scale damage during the cooling of the specimens. It was found that the scale damage on the undoped specimens occurs earlier during the process of cooling as compared to the scale damage in the doped specimens (Figures 26-27). Furthermore, the instantaneous scale damage on the former specimens during cooling reaches a maximum value and then drops off, while it continues to rise throughout the cooling process in the latter specimens.

The occurrence of scale failure at relatively higher temperatures in the undoped specimens can have two alternate explanations: (a) The scale on the undoped specimens had larger growth stresses as compared to the growth stresses in the doped specimens. Therefore the critical stress required for the crack growth along the scale/substrate interface (eqn. 9) was reached earlier during cooling of the undoped specimens. (b) The growth stresses were not very different in the two types of specimens but the interface in the undoped specimen was weak; which implies that the scale/substrate interface failure in the undoped alloys had occurred at lower stress levels. If an estimate of the stress level at which scale failure occurs in the two types of specimens could be obtained, it will be possible to determine which of the above two explanations holds true. In the following section an attempt will be made to obtain some estimate of the stress level at which scale failure occurs.

#### 6.3.4 AE Counts per Unit Spalled Area

The number of AE counts from a single AE event are related to its peak amplitude (eqn. 12). The peak amplitude of an event, in a crack growth process, is in turn related to the incremental area swept out and the stress intensity at the crack tip (eqn. 14). In an oxide scale failure process during cooling numerous acoustic emission events occur at varying stress levels. The total number of AE counts ( $N$ ) in such a process can be expected to be proportional to the total spalled area ( $A_s$ ) and the average stress level  $\sigma_a$  at which the failure had occurred;

$$N \propto (\sigma_a)(A_s)$$

The AE Counts per unit spalled area, therefore, will be a function of the stress level at which failure had occurred. Alternatively, AE counts are also related to the energy release which is again a function of the stress intensity at the crack tip during the crack growth process.

Quantitative measurements of spalled areas were performed by taking several SEM micrographs of an oxidized specimen at random locations and analyzing the micrographs by an image analyzer. These measurements were carried out on the specimens oxidized for 24 hours in the short term AE tests. As mentioned earlier, no spalling of  $\text{Al}_2\text{O}_3$  scale was detected on the CoCrAl-0.2Y and CoCrAl-1.0Hf specimens. The results of the estimated spalled area for the rest of the four specimens are given in Table II. The AE count/spalled areas for each specimen are also given in the table. The AE counts/spalled area were more than an order of magnitude greater for the doped specimens as compared to the undoped ones. The difference between the two undoped (NiCrAl and CoCrAl) or between the two doped (NiCrAl-0.2Y and NiCrAl-1.0Hf) specimens was not large. The higher number of AE counts/spalled area for the specimens containing active element suggest that the scale failure in these specimens must have occurred at a higher stress level than in the undoped specimens. The scale failure at higher stress level can be explained on the basis of a stronger scale/substrate interface, that is, a higher value of  $K_{\text{c}}^{\text{i}}$  in equation (9).

Difficulties were encountered in measuring the spalled area on the specimens which were cyclically oxidized in the AE experiments due to insufficient contrast between the different  $\text{Al}_2\text{O}_3$  layers which were formed due to the repetitive spalling and the formation of new oxide. However, according to a rough estimate, the AE counts/spalled area for the active element containing cyclically oxidized specimens were also an order of magnitude greater than those for the undoped specimens. For instance, there were over 25 million counts during the sixth cooling cycle of the NiCrAl-0.8Y specimen (Figure 30), the scale was spalled from about 60% of the surface; but during the cooling of the undoped NiCrAl specimen after 24 hours of oxidation the scale was almost completely spalled, yet the total AE counts were only 2.6 million.

The size of the spalled oxide flake can also be taken as an indication of the fracture resistance of the interface. Once the critical stress required for crack growth along the scale/substrate interface is reached, the crack can grow a longer distance if the fracture resistance of the interface,  $K_{\text{c}}^{\text{i}}$ , is low (eqn. 10). The  $\text{Al}_2\text{O}_3$  scales from the undoped NiCrAl and CoCrAl specimens were spalled off in relatively large flakes. A few such  $\text{Al}_2\text{O}_3$  flakes are shown in Figure 58.

#### 6.2.5 Peak Amplitude Analysis

Peak amplitudes of the events during the cooling of oxidized specimens did not follow a 'power law' distribution instead, the distributions in most cases can be approximated to two intersecting normal distributions as shown schematically in Figure 59. The bimodal distribution is consistent with the two types of cracking events which may occur during a scale failure process i.e. crack growth along the scale/substrate interface and crack growth within the scale in the through-thickness direction. Although, scale failure under biaxial compression primarily occurs by buckling and crack growth along the interface, cracking in the through-thickness direction occurs during the eventual spallation process (Figure 22c). Local inhomogenities, such as second phase oxide particles, are additional sources of through-thickness cracking. In the following discussion, a crack growth

increment along the scale/substrate interface will be referred to as a 'spalling event' and crack growth in the through-thickness direction will be referred to as a 'cracking event'.

It is believed that the low amplitude AE events in the distributions are related to the cracking events and the high amplitude events are related to the spalling events, since the strain energy release will be much larger in the delamination process than in the crack growth in the through-thickness direction<sup>(77)</sup>. The range of peak amplitudes over which spalling events occur seems to vary a great deal during the scale failure in different specimens, but this range is fairly constant for the cracking events. The reasons may be as follows. The peak amplitude of an AE event depends upon the incremental area swept in the crack growth step, and the stress intensity at the crack tip (eqn. 14). In spalling events both factors may vary a great deal depending upon the morphology of the scale/substrate interface and the fracture resistance of the interface. On the other hand, these factors are fairly constant for the cracking event, since the area swept is limited by the thickness of the  $\text{Al}_2\text{O}_3$  scale and the stress intensity at the crack tip is determined by the fracture toughness of the  $\text{Al}_2\text{O}_3$  scale.

Although there should not be a sharp boundary between the peak amplitudes of the cracking or spalling events, for the sake of discussion, the events less than or equal to 40 dBs will be considered as cracking events and the events above 40 dBs will be considered as spalling events. The number of cracking events (< 40 dBs) was almost always found to be about an order of magnitude greater than the spalling events (> 40 dBs). Assuming scale failure under biaxial compression occurs primarily by crack growth along the interface, the larger number of cracking events can be explained on the basis of the generation of the large number of cracking events during the tearing of the scale when the crack growth along the interface temporarily stops and eventual spallation occurs. As pointed out earlier, the local inhomogenities in the scale are additional sources of cracking events. The specimens such as CoCrAl-0.2Y and CoCrAl-1.0Hf which had very little scale damage also had a very small number of AE events during cooling, particularly, the high amplitude events were not statistically large enough even to give rise to another peak in the distributions (Figures 37 and 38). The peak amplitude distribution for such specimens had only one apparent peak.

#### 6.2.6 Effect of Active Elements

To gain a better insight into the scale failure process a real time analysis of the peak amplitudes was also performed during the slow cooling of specimens. The main intention was to study the relative occurrence of the cracking and spalling events during the scale failure process. The amplitude distributions were recorded at every fifty degree interval during cooling. The ratio of the spalling events (> 40 dBs) to the cracking events (< 40 dBs) for each fifty degree interval is plotted against the temperature of the specimens in Figure 60, for the nickel base alloys. The spalling to cracking ratio for the undoped NiCrAl specimen starts out high, as the scale failure process starts, but decreases continuously throughout the cooling process. On the other hand this ratio for the NiCrAl-0.2Y and NiCrAl-1.0Hf specimen is relatively low and did not change very much during cooling.

The above trends in the spalling to cracking ratios can be best explained on the basis of a weak scale/substrate interface in the NiCrAl specimen and a relatively strong scale/substrate interface in the specimens doped with yttrium or hafnium. Because of the weak scale/substrate interface in the NiCrAl specimen, relatively

more spalling events occurred in the beginning of cooling. Through-thickness cracking occurs later in the process. In the doped specimens, because of the relatively stronger interface, cracks along the interface grow shorter distances before eventual spallation occurs. Therefore, the spalling to cracking ratio was small and remained almost the same throughout the cooling process.

#### 6.2.7 Effect of the Scale/Substrate Interface Morphology

The crack growth process along the scale/substrate interface may be affected by the morphology of the interface. Along a highly irregular interface crack growth will occur in a large number of small steps and along a relatively flat interface it will occur in a small number of large steps. Therefore, the peak amplitude of the events (spalling events), which are proportional to the area swept in the incremental step, will be affected by the morphology of the interface. Amplitude distributions which were obtained during the 24 hour thermal cycling of the NiCrAl-0.2Y and NiCrAl-1.0Hf specimens are superimposed in Figure 61. The peak amplitudes of the spalling events in the NiCrAl-1.0Hf specimen were relatively lower and also had a relatively narrow range as compared to the peak amplitudes of the corresponding events in the NiCrAl-0.2Y specimens. The scale/substrate interface was highly irregular in the former specimen (Figure 6.5a) and relatively flat in the latter specimen (Figure 6.5c).

The scale/substrate interface was not as irregular in the NiCrAl-0.3Hf alloy compared with NiCrAl-1.0Hf alloys (Figures 53c and 53e). The peak amplitude distributions obtained during the cooling of these two specimens are compared in Figure 62. The spalling events for the NiCrAl-0.3Hf does seem to occur over a greater range of peak amplitudes. The peak amplitude distributions for the three yttrium containing nickel base alloys are compared in the Figure (63). The ranges of the peak amplitudes are approximately the same for all three alloys. The NiCrAl-0.02Y and the NiCrAl-0.2Y specimens had relatively flat interfaces but the NiCrAl-0.8Y did contain oxide pegs which may temporarily stop the crack growth along the interface. One would expect a narrower range of peak amplitudes. Perhaps the pegs were too widely spaced to be an effective barrier to crack growth along the interface.

### 6.3 Cyclic Oxidation Resistance of the Alloys

A correlation was found between the long term cyclic oxidation resistance of different alloys and the total number of AE counts detected during the cooling of oxidized specimens in the relatively short term cyclic oxidation tests. The total number of AE counts resulting from oxide scale damage are not only proportional to the spalled area on the specimen surface but are also proportional to the fracture resistance of the scale/substrate interface.

The AE counts/spalled area varied a great deal between the doped and undoped alloys, but the values of this ratio were in the same order for the various active element containing alloys. Therefore, the total AE counts for different active element containing specimens were a good measure of the degree of scale damage on the specimen. Similarly, the weight changes, in the active element containing specimens undergoing long term cyclic oxidation, were also a measure of the scale damage, since the weight gains due to scale growth were approximately the same in these specimens. However, the AE technique is more sensitive to scale damage than the weight measurements, since, mere cracking of the oxide scale cannot be detected by weight change measurements but it could be detected by the AE

technique. In the following discussion an attempt will be made to rationalize the cyclic oxidation behavior of the various alloys.

### 6.3.1 CoCrAl vs. NiCrAl

The thermal cyclic oxidation resistance of both undoped NiCrAl and CoCrAl alloys were poor, but based on the results of short term AE tests and the SEM examination of oxidized specimens, the adherence of the  $\text{Al}_2\text{O}_3$  scale, if anything, was better on the CoCrAl alloy than on the NiCrAl alloy. However, the differences in the thermal cyclic resistances of active element containing NiCrAl and CoCrAl alloys were very obvious. The number of AE counts detected during the cooling of active element containing cobalt base alloys were approximately an order of magnitude less than those detected during the cooling of the best nickel base alloys (Figure 30).

Virtually no scale damage was observed on the cobalt base specimens undergoing short term thermal cycling. Even after 1000 hours of thermal cycling only localized scale damage occurred on these alloys (Figure 41), whereas, significantly greater scale damage was observed on the corresponding nickel base alloys (40). The severity of scale damage on the latter type of alloys was, however, a function of the active element added and the extent of thermal cycling.

The reasons for the superior behavior of the doped CoCrAl alloys are not yet clear. It should be pointed out that these differences are not believed to be due to the fabrication of the alloys by casting, since similar differences were observed by Giggins and Pettit<sup>(33)</sup> earlier where NiCrAlY and CoCrAlY alloys were formed by physical vapor deposition. Barrett and Lowell<sup>(78)</sup> have also found that the cobalt base alloys, containing chromium and aluminum matching the alloys used in the present study, were superior to most other nickel or cobalt base alloys in their study. They have also found that the cobalt base alloys in question did not perform well in the high frequency thermal cycling tests. In the following, the possible reasons for the superior behavior of active element containing cobalt base alloy will be discussed.

The thermal stresses due to differential thermal contraction cannot be expected to be lower in the  $\text{Al}_2\text{O}_3$  scale on the cobalt base alloys than the nickel base alloys. The thermal expansion coefficient, of the  $\alpha$ -Cobalt layer adjacent to the  $\text{Al}_2\text{O}_3$  scale in the former alloys is actually slightly larger than the corresponding  $\gamma$ -layer in the latter alloys<sup>(79)</sup>. The morphology of the scale/substrate interfaces was found to be a function of the type and concentration of active element added but not a function of base metal. Therefore, a particular scale/substrate interface morphology cannot be held responsible for the better adherence of  $\text{Al}_2\text{O}_3$  scales on the cobalt base alloys. The isothermal weight gains were indeed slightly lower for the CoCrAl, CoCrAl-0.2Y, and CoCrAl-1.0Hf specimens as compared to those for the corresponding nickel base specimens (Figure 21). The growth stresses were possibly lower in the  $\text{Al}_2\text{O}_3$  scale on the cobalt base alloys. The smaller scale growth rates, however, cannot be solely responsible for the better cyclic oxidation resistance of the cobalt base alloys, since the NiCrAl-0.3Hf alloys which had the smallest weight gain during isothermal oxidation showed the poorest cyclic oxidation resistance among all the active element containing alloys.

Based on the chemical bonding theory of adhesion, the adherence of oxide on a metal is related to the affinity of that metal for oxygen. Experimentally determined work of adhesion for liquid cobalt on  $\text{Al}_2\text{O}_3$  substrates in a previous

study was indeed found to be greater than that for liquid nickel on an  $\text{Al}_2\text{O}_3$  substrate<sup>(7)</sup>, but the difference between the two is really not large enough to explain the differences in the adherence of  $\text{Al}_2\text{O}_3$  scales on the two types of alloys observed in the present study.

Nevertheless,  $\text{Al}_2\text{O}_3$  scales do seem to be more adherent on the cobalt base alloys, since the mechanical stripping of  $\text{Al}_2\text{O}_3$  scales by the application of a tensile load was possible from most of the nickel base specimens but the scale could not be stripped from the CoCrAl-0.2Y and CoCrAl-1.0Hf specimens. The scale/substrate interface in the CoCrAl-1.0Hf specimen was very irregular due to the hafnium oxide pegs (Figure 53d). Separation of this scale under tensile load can be expected to be difficult. The same is true for the NiCrAl-1.0Hf specimen which was the only nickel base specimen from which  $\text{Al}_2\text{O}_3$  could not be stripped mechanically. The scale/substrate interfaces were however, very flat and quite similar in the CoCrAl-0.2Y and NiCrAl-0.2Y specimens (Figures 43 and 45). The scale was successfully stripped from the latter specimen but not from the former specimen. This shows the  $\text{Al}_2\text{O}_3$  was indeed more adherent in the cobalt base alloys. Unfortunately no measurement of AE counts per unit spalled area could be carried out for the CoCrAl-0.2Y and CoCrAl-1.0Hf (because the scale damage was very small), which could provide some additional information about the fracture resistance of the scale/substrate interface in these specimens.

#### 6.3.2 Yttrium Doped Alloys

The relative thermal cyclic oxidation resistance of the yttrium containing NiCrAl and CoCrAl alloys was correctly predicted by the total number of AE counts on the first cooling cycle, but the real differences between these alloys became apparent only after several thermal cycles (Figure 30). The AE counts for NiCrAl-0.8Y specimen increased exponentially as the number of cooling cycles progressed. The AE counts for NiCrAl-0.2Y and NiCrAl-0.02Y were much less than those for NiCrAl-0.8Y and did not increase as much with the thermal cycling. The CoCrAl-0.2Y specimen had the least number of AE counts among all the yttrium doped specimens. The SEM analyses of the surfaces of the specimens showed, severe scale damage on the NiCrAl-0.8Y specimen but only localized scale damage on NiCrAl-0.2Y and NiCrAl-0.02Y specimens; and no scale damage on the CoCrAl-0.2Y specimen (Figure 31).

The difference between NiCrAl-0.2Y and NiCrAl-0.02Y was not large but the number of AE counts during each cooling cycle were consistently greater for the NiCrAl-0.02Y specimen than the NiCrAl-0.2Y specimen. Similar differences were found in their long term cyclic oxidation behavior (39).

The large yttrium oxide pegs which were observed at the scale/substrate interface in the NiCrAl-0.8Y specimens (Figure 58b), may be responsible for the excessive scale damage. Although in principle, an irregular interface can provide a mechanical keying effect, it has been shown<sup>(11)</sup> that the size and distribution of the irregularity is extremely important. Previously, researchers<sup>(19,34)</sup> have reported preferential scale damage in the vicinity of a large yttrium oxide peg.

The yttrium oxide particles which were observed on the stripped  $\text{Al}_2\text{O}_3$  scales from the NiCrAl-0.2Y and CoCrAl-0.2Y specimens (Figures 44 and 47b) did not show any scale damage in their vicinity. However, these oxide particles cannot be held responsible for the improved scale adherence on these specimens for the following reasons. Firstly these particles were widely distributed, secondly the shape of the



particles was not such which can provide any mechanical keying effect, and finally the NiCrAl-0.02Y specimen had good adherence of the  $\text{Al}_2\text{O}_3$  scale despite the absence of any yttrium oxide particles or pegs at the scale/substrate interface. The exact yttrium content of the NiCrAl-0.02Y alloy, as determined by the plasma arc method, was only 0.0084 %. Pivin et. al.<sup>(45)</sup> have also found that yttrium as low as 0.0085%, was very effective in improving  $\text{Al}_2\text{O}_3$  scale adherence on FeNiCrAl alloys. Therefore it seems that even very small amounts of yttrium can be very effective in improving scale adherence.

### 6.3.3 Hafnium Doped Alloys

Three hafnium doped alloys were studied namely, NiCrAl-0.3Hf, NiCrAl-1.0Hf and CoCrAl-1.0Hf. The relative cyclic oxidation resistance, as determined by the AE tests and by the post examination of the oxidized specimens by SEM, was the best for the CoCrAl-1.0Hf alloy among the three. The next best was the NiCrAl-1.0Hf alloy and the worst of all was the NiCrAl-0.3Hf. The first two alloys developed a relatively fine network of hafnium oxide pegs at the scale/substrate interface (Figures 53d and 53e). The third alloy which contained relatively less hafnium had very few and widely distributed oxide pegs (Figure 53c). The type of scale/substrate interface morphology developed in the former alloys, in principle, can provide a mechanical keying between the scale and the substrate. The oxide pegs in the NiCrAl-0.3Hf alloy may be too widely separated to provide an effective mechanical keying, instead these pegs may have been acting as stress concentration sites as they were thought to be in the case of NiCrAl-0.8Y alloy.

The NiCrAl-0.3Hf specimen also showed anomalous behavior in the cyclic oxidation AE experiments (Figure 30). While for most of the specimens the number of AE counts increased as a function of the number of cooling cycles, for the NiCrAl-0.3Hf specimen the AE counts actually dropped during thermal cycling after the second cooling cycle. The  $\text{Al}_2\text{O}_3$  scale was completely spalled from the surface of the NiCrAl-0.3Hf specimen during the second cooling cycle. The scales which developed in the latter periods of cyclic oxidation were relatively richer in chromium which was obvious from the color of the specimen. The decrease in AE counts may be related to the different acoustic emission characteristics of the latter formed scales.

Comparing the oxide peg morphologies in the NiCrAl-1.0Hf and CoCrAl-1.0Hf oxidized specimens (Figures 53d and 53e), the pegs in the latter alloy are in fact relatively finer than the pegs in the former specimen. The difference is, however, not large and there may be other factors responsible for the excellent thermal cyclic resistance of the CoCrAl-1.0Hf alloy.

### 6.4 Mechanism of Improved Scale Adherence

The mechanisms proposed to account for improved scale adherence, can be divided into two groups. Those which emphasize the generation of smaller amount of stresses or the relaxation of stresses in the presence of reactive additions, such as yttrium and hafnium; and those which emphasize the generation of a stronger scale/substrate interface. The first group includes enhanced plasticity, graded seal, and modification to growth process mechanisms. The second group consists of the vacancy sink, chemical bonding, and the oxide pegging mechanisms.

Some of the data obtained in the present study, such as the lowering of scale growth rates by the small additions of yttrium or hafnium and the generation of an

undulated scale/substrate interface in the undoped specimens, were found to be consistent with the proposal of reduced growth stresses<sup>(19)</sup>. However, the acoustic emission data clearly indicate a stronger scale/substrate interface in the presence of active elements. Therefore, the improved scale adherence can be explained on the basis of more than one mechanism. However, the principal effect of the oxygen active elements in improving the oxide scale adherence must be the formation of a stronger scale/substrate interface.

A scale/substrate interface can be made stronger (or more resistant to crack growth) by physical, chemical or by mechanical means. Each of these means has been emphasized in the above three proposed mechanisms. The vacancy sink mechanism proposes the achievement of a stronger interface by physical means i.e. the elimination of voids at the interface. The oxide pegging mechanism suggests the mechanical keying of the oxide scale and the chemical bonding mechanism emphasizes the direct role of the oxygen active element in making a stronger chemical bond across the scale/substrate interface.

The  $\text{Al}_2\text{O}_3$  scale on the undoped NiCrAl and the CoCrAl specimens oxidized for 24 hours spalled off profusely despite very small and very few voids at the scale/substrate interface. The large voids, however, have been observed at the interfaces of the undoped specimens which were oxidized for one week (Figures 49 and 51). These voids indicate the separation of the  $\text{Al}_2\text{O}_3$  scale during the isothermal oxidation due to growth stresses. The separation of the  $\text{Al}_2\text{O}_3$  scale at temperature can again be explained on the basis of a relatively weak scale/substrate interface rather than the larger amounts of growth stresses as compared to the growth stresses in the  $\text{Al}_2\text{O}_3$  scale on the doped specimens. Therefore, a stronger interface is not only required to resist crack growth under thermal stresses during cooling but also to resist crack growth along the interface during the isothermal oxidation period.

The adherence of the  $\text{Al}_2\text{O}_3$  scale was good to excellent, on the NiCrAl-0.02Y, NiCrAl-0.2Y and CoCrAl-0.2Y specimens. These specimens had flat scale/substrate interfaces and contained no oxide protrusions from the  $\text{Al}_2\text{O}_3$  layer into the substrate alloy which can be considered to provide any keying effect. Hence, mechanical keying is not a necessary requirement for the improved  $\text{Al}_2\text{O}_3$  scale adhesion. On the other hand if the oxide pegs are large and widely spaced they may act as stress concentration sites at interfaces and may result in excessive scale damage. This type of oxide peg was observed in the NiCrAl-0.8Y and NiCrAl-0.3Hf specimens, both of which had poor resistance to scale damage.

The data in the present study are consistent with the improved  $\text{Al}_2\text{O}_3$  scale adhesion on the active element containing alloys by chemical means. The improved scale adhesion by chemical means has been suggested to occur two alternative ways. The oxygen active elements may segregate to the interface and form a strong chemical bond with the  $\text{Al}_2\text{O}_3$  layer due to their higher energies of oxide formation, or the active element in an alloy may act as a scavenger to harmful impurities such as sulphur, which would otherwise segregate at the scale/substrate interface and weaken the scale-substrate bond<sup>(61)</sup>.

The surfaces of  $\text{Al}_2\text{O}_3$  scales and substrates exposed as a result of mechanical stripping of the scale from the NiCrAl-0.2Y and NiCrAl-0.02Y specimens were analyzed by scanning Auger electron microscopy. The results of this analysis were inconclusive to show any enrichment of yttrium on the stripped surfaces. This may be due to the atmospheric oxidation of the exposed substrates prior to the Auger analysis.

## 6.5 Optimum Conditions for the Active Element Additions

Although the smaller additions of yttrium were found to be more effective than the hafnium additions in improving the cyclic oxidation resistance of the NiCrAl alloys in the present study and elsewhere<sup>(61)</sup> the hafnium was at least as effective as yttrium in the CoCrAl alloy (Figure 30 and 39). In fact Allam et. al.<sup>(34)</sup> have found hafnium to be somewhat better than yttrium in Co-10Cr-11Al alloy. Therefore, it seems that both type of elemental additions could be very effective in improving the cyclic oxidation resistance of MCrAl type alloys. However, since their oxidation behavior in an alloy depends on their solubilities, they tend to produce different scale/substrate interface morphologies. Consequently, the optimum conditions of their addition also differ.

The NiCrAl alloys doped with the smaller amounts of yttrium (NiCrAl-0.02Y and NiCrAl-0.2Y) had better cyclic oxidation resistance than the alloy doped with a relatively large amount of yttrium (NiCrAl-0.8Y). However doping with higher amounts of hafnium (NiCrAl-1.0Hf) was more effective than the doping with a smaller amount of hafnium (NiCrAl-0.3Hf). Since yttrium has much lower solubility than hafnium in these type of alloys, these results indicate that the beneficial effects of these additions are dependent on the amount dissolved in an alloy.

Because of its lower solubility yttrium tends to form intermetallic phases in the alloy. Upon oxidation these phases internally oxidize and give rise to yttrium oxide pegs. Apparently internal oxidation of dissolved yttrium does not occur. However, the dissolved hafnium does get internally oxidized and gives rise to hafnium oxide pegs at the scale/substrate interface.

Although the oxide pegs at the interface are not necessary for good adherence of oxide scale, they can be beneficial or harmful depending on their size and distribution. When yttrium is added above its solubility, it may produce fewer but larger size pegs depending upon the size and distribution of the yttride phase in the alloy. These type of oxide pegs are less likely to provide any mechanical keying effect. Instead, they produce an adverse effect of stress concentration. The size and distribution of the hafnium oxide pegs, on the other hand, depend upon the concentration of the dissolved hafnium in an alloy. When hafnium is added close to its solubility (i. e., about 1%), such as in NiCrAl-1.0Hf and CoCrAl-1.0Hf alloys, a large number of more uniformly distributed oxide pegs are generated (Figure 53d and 53e). This type of peg distribution can mechanically key the scale to the substrate.

Unfortunately all oxide pegs, regardless of their size and distribution, are partially or completely incorporated in the inwardly growing  $\text{Al}_2\text{O}_3$  scales and provide rapid diffusion paths, which results in higher oxidation rates. Therefore, improved adherence of  $\text{Al}_2\text{O}_3$  scales with a planar scale/substrate interface is more desirable, as was observed in the following alloys: CoCrAl-0.2Y, NiCrAl-0.2Y and NiCrAl-0.02Y.

While smaller amounts of yttrium additions generally produce a planar scale/substrate interface, a planar scale/substrate interface was not produced in the NiCrAl-0.3Hf alloy. However, small hafnium additions (< 0.3%) have been shown to produce a planar scale/substrate interface and good scale adherence on Co-10Cr-11Al alloys<sup>(34)</sup>.

## 7. SUMMARY AND CONCLUSIONS

In the present study the effects of small additions of yttrium and hafnium on the isothermal and the cyclic oxidation behavior of MCrAl type coating alloys were studied. The base alloys were Ni-20Cr-10Al and Co-20Cr-10Al. The microstructures of these alloys were thoroughly characterized prior to the oxidation experiments. Both isothermal and the cyclic oxidation tests were performed at 1100 °C for varying durations. Since the oxide scale failure process is a function of residual stresses, morphology and fracture resistance of the scale/substrate interface, an emphasis was given to the insitu study of the oxide scale failure process to gain pertinent information about the mechanisms of scale adherence. An acoustic emission technique was employed to study the scale failure processes. A summary of the significant results is presented in the following.

### Isothermal Oxidation Behavior

- The growth of  $\text{Al}_2\text{O}_3$  scales on the undoped NiCrAl and CoCrAl alloys followed parabolic kinetics. The values of the parabolic rate constants were approximately the same for both of the alloys. The scale growth on most of the doped alloys did not follow parabolic kinetics. However, the overall weight gains during the isothermal oxidation were slightly, less for the alloys doped with relatively small amounts of yttrium or hafnium, as compared to the undoped alloys. Conversely, the alloys doped with relatively larger amounts of yttrium or hafnium had higher weight gains than the undoped alloys.
- The increase in scale growth rate is related to the formation and incorporation of oxide pegs in the  $\text{Al}_2\text{O}_3$  scale which provided rapid diffusion paths through the scale. The decrease in scale growth rate may be related to the alteration of the defect structure of the  $\text{Al}_2\text{O}_3$ .
- Despite the general spallation of the  $\text{Al}_2\text{O}_3$  scale on the undoped alloys oxidized up to 24 hours, the exposed surfaces of the substrate did not show any significant amount of voids or any other signs of adherence loss during the isothermal oxidation period. However, the scale/substrate interface in the undoped alloys was undulated, indicating plastic deformation of the substrate under the the influence of growth stresses.
- The  $\text{Al}_2\text{O}_3$  scale on the doped alloys remained adherent for the extended period of isothermal oxidation. The scale/substrate interfaces were flat in the alloys doped with smaller amounts of yttrium (NiCrAl-0.02Y, NiCrAl-0.2Y and CoCrAl-0.2Y). The alloys doped with hafnium or higher amounts of yttrium (NiCrAl-0.3Hf, NiCrAl-1.0Hf, CoCrAl-1.0Hf and NiCrAl-0.8Y) developed oxide protrusions at the scale/substrate interface. The size and distributions of the oxide protrusions at the interfaces were a function of the type and concentration of the active element added.

### Yttrium vs Hafnium

-Differences in the oxidation behavior of yttrium and hafnium were related to the differences in their solubilities in the alloys. Because of its smaller solubility, yttrium tends to form intermetallic phases in the alloy. Upon oxidation, these phases internally oxidize and give rise to yttrium oxide pegs. Apparently internal

oxidation of the dissolved yttrium does not occur. However, the dissolved hafnium does get internally oxidized and gives rise to hafnium oxide pegs at the scale/substrate interface.

-Although the oxide pegs at the interface are not necessary for good adherence of oxide scales, the size and distribution of these pegs are important. The size and distribution of oxide pegs in the hafnium doped alloy depends on the hafnium content but in the yttrium doped alloy it is a function of the size and distribution of the yttride phase in the alloy.

-The correlation between the solubility and oxidation behavior is not limited to yttrium and hafnium only. Other commonly used active elements seem to follow the same trend.

### Al<sub>2</sub>O<sub>3</sub> Scale Failure Process

-The rate of acoustic emission counts was used to determine the rate of scale damage during the cooling of oxidized specimens. Most of the scale damage during cooling on the undoped alloys took place at higher temperatures as compared to the scale damage on the doped alloys.

-The AE counts/unit spalled area, which are related to the stress level at which the failure occurs, were about an order of magnitude greater from the scale damage on the doped alloys than those from the undoped alloys. The above results were explained on the basis of a weaker scale/substrate interface in the undoped alloys as compared to the interface in the doped alloys. Further evidence of the weak interface in the undoped alloys was obtained by the peak amplitude analysis of the AE events.

-The peak amplitude analysis was used to distinguish the two types of cracking events during oxide failure in particular the 'cracking events' which arise from the crack growth in the through-thickness direction and the 'spalling events' which arise from the crack growth along the interface. Because of the weak scale/substrate interface in the undoped alloys the spalling events were predominant early in the process of the scale failure during cooling. The spalling to cracking event ratio, however, remained constant throughout the cooling of the alloys doped with yttrium or hafnium.

-A correlation was also found between the peak amplitude distributions and the morphologies of the scale/substrate interfaces in the various active element containing alloys. The specimens which had a highly irregular interface due to oxide pegs, generated a large number of small amplitude events indicating the scale failure occurred in a large number of small steps. The specimens which had a relatively flat interface generated a small number of high amplitude events indicating that scale failure occurred in a small number of large steps.

### Thermal Cyclic Resistance of the Alloys

-A good correlation was found between the total number of AE counts generated during the cooling of various doped specimens and their long term cyclic oxidation resistance as determined by the 1000 hour cyclic oxidation weight change tests.

-Both yttrium and hafnium were found more effective in the cobalt base alloys than in the nickel base alloys. A satisfactory explanation of this behavior is not available.

-The nickel base alloys doped with smaller amounts of yttrium (NiCrAl-0.02Y and NiCrAl-0.2Y) had better cyclic oxidation resistance than the alloy doped with a relatively large amount of yttrium (NiCrAl-0.8Y). In contrast doping with higher amounts of hafnium (NiCrAl-1.0Hf) was more effective than a smaller amount of hafnium (NiCrAl-0.3Hf). Since yttrium has a much smaller solubility than hafnium, the above results indicate that the beneficial effects of these additions are related to the amount of active element dissolved in the alloy.

### Major Conclusions

- \* The principal effect of oxygen active elements in improving oxide scale adherence is the formation of a stronger scale/substrate interface.
- \* The stronger scale/substrate interface is not primarily due to the elimination of the interfacial voids or the generation of oxide pegs. Improved chemical bonding may be important but this aspect was not critically examined.
- \* The beneficial effect of an active element on scale adhesion is related to the amount of this element dissolved in the alloy.
- \* The oxidation behavior of an oxygen active element depends on its solubility in the alloy. Most commonly used oxygen active elements can be divided into two groups based on their solubilities or their atomic sizes.
- \* Good adherence of oxide scales via a planar scale/substrate interface is more desirable than adherence by oxide pegging. The above conditions are generally met by relatively small additions of the low solubility active elements such as yttrium.
- \* The acoustic emission technique was found to be very useful in obtaining both qualitative and quantitative information about scale failure processes. By using this technique, the scale failure process can be followed event by event, and the long term cyclic oxidation resistance of an alloy can be evaluated by a relatively short term test.

### III. OXIDATION OF Ni-Si ALLOYS

#### 1. INTRODUCTION

Alloys and coatings for high temperature applications generally obtain oxidation resistance by the selective oxidation of Cr or Al to form protective surface films of  $\text{Cr}_2\text{O}_3$  or  $\text{Al}_2\text{O}_3$ . As a result, the formation of  $\text{Cr}_2\text{O}_3$  and  $\text{Al}_2\text{O}_3$  have been extensively studied (e.g. refs. 80 and 81). The selective oxidation of Si to form  $\text{SiO}_2$  films has not been investigated in great detail but appears to offer great potential as another means of protecting high temperature alloys and coatings. In this section the literature on the formation of  $\text{SiO}_2$  on pure Si (generated mainly in studies of semiconductor device fabrication) and on the oxidation of alloys and ceramics which form protective oxides which are rich in Si will be briefly reviewed. The results of the experimental study on the high temperature oxidation of binary Ni-Si alloys will then be described.

##### 1.1 Oxidation of Si

The oxidation of Si to form vitreous  $\text{SiO}_2$  layer is generally assumed to follow what are termed "linear-parabolic kinetics". This growth law introduced by Deal and Grove<sup>(82)</sup> may be written:

$$x^2 + Ax = Bt \quad (1)$$

where  $x$  = oxide thickness  
 $t$  = oxidation time  
 $A, B$  = constants

For short times and low temperatures

$$x = \frac{Bt}{A} \quad (2)$$

and for times and higher temperatures

$$x = B^{\frac{1}{2}} t^{\frac{1}{2}} \quad (3)$$

so that  $B/A$  is referred to as the "linear rate constant",  $k_l$ , and  $B$  as the "parabolic rate constant",  $k_p$ .

There is general agreement that amorphous  $\text{SiO}_2$  grows on Si by the inward transport of oxidant. This is based on observations that (i)  $k_p \propto p_{\text{O}_2}$ , (ii) the activation energy for oxygen diffusion and oxidation are virtually equal at high temperatures and (iii) experiments in which the oxidizing gas is switched after some exposure time from  $\text{O}^{16}$  to  $\text{O}^{18}$  results in nearly all of the  $\text{O}^{18}$  being concentrated at the Si/ $\text{SiO}_2$  interface<sup>(83)</sup>. However, there is some question regarding the particular oxidizing species which is transported and considerable controversy regarding the nature of the transport path through the oxide. Kroger<sup>(84)</sup> has recently reviewed the literature on the defect structure of  $\text{SiO}_2$  and concludes that the major species transported are charged oxygen interstitials,  $\text{O}_2^-$ ,  $\text{O}_2^{2-}$ , and  $\text{O}_2$ ,  $\text{i}$ , but uncharged  $\text{O}_2$  is probably not much slower. The transport by charged species is not consistent with  $k_p \propto p_{\text{O}_2}$  as pointed out by Kroger<sup>(84)</sup>.

The rate of growth of vitreous  $\text{SiO}_2$  on Si occurs with rates several times faster than those calculated from the diffusion coefficient of oxygen in vitreous  $\text{SiO}_2$ <sup>(85)</sup>, thus indicating the presence of short-circuit paths through the oxide. These paths have been proposed to be "micropores" extending through the oxide (or nearly through<sup>(86,87)</sup> and, alternatively, to the formation of channels formed perpendicular to the specimen surface by localized structural ordering of the  $\text{SiO}_2$ <sup>(85)</sup>. Pores have been reported in  $\text{SiO}_2$  films grown on Si based on transmission electron microscopy results<sup>(88)</sup> but the exact nature of the paths for oxidant transport is not yet resolved.

The linear rate constant,  $k_l$ , is observed to depend on  $p_{\text{O}_2}$  raised to a power,  $m$ , which is usually between 0.6 and 0.8 rather than linearly on  $p_{\text{O}_2}$  as would be expected from Eqn. (3)<sup>(89)</sup>. This requires the expression for the interface reaction to be written as

$$R = k N_l^m \quad (4)$$

so that the overall kinetics cannot be strictly "linear parabolic". Hu<sup>(89)</sup> has derived a more complex rate law taking this into account and has analyzed the reaction at the Si/ $\text{SiO}_2$  interface as being controlled by chemisorption of oxidant.

The oxidation of Si by water vapor is much faster than in dry oxygen with both  $k_p$  and  $k_l$  being increased. When oxidation is carried out in pure water vapor  $k_p$  and  $k_l$  are found to vary linearly with the partial pressure of water vapor<sup>(90)</sup>. The transport of oxidant is proposed to occur by the ambipolar diffusion of hydronium ( $\text{H}_3\text{O}^+$ ) and hydroxyl ( $\text{OH}^-$ ) ions<sup>(90)</sup>.

The growth of  $\text{SiO}_2$  on Si has also been reported to be influenced by growth stresses generated by the formation of new oxide at the Si/ $\text{SiO}_2$  interface. The activation energy associated with  $k_p$  is found to be independent of temperature above about 950°C but to vary with temperature below 950°C. This has been explained as a reduction of the diffusion coefficient of oxidant in the inner region of the  $\text{SiO}_2$  layer due to compressive stresses<sup>(91)</sup>. These stresses are partially relieved by viscous flow below 950°C, giving rise to the variation in activation energy, and are completely relieved above 950°C. Generation of compressive stresses in the oxide have also been used to explain the reduced oxide thickness formed over step-edges on nonplanar Si surfaces<sup>(92)</sup>.

The oxidation of Si can be markedly influenced by oxide vapor species at low oxygen pressures. The reason for this may be seen from the volatile species diagram for the Si-O system in Figure 64. A significant pressure of SiO is seen near the dissociation pressure of  $\text{SiO}_2$ (s). This can result in a rapid flux of SiO away from the specimen surface and subsequent formation of a non-protective  $\text{SiO}_2$  smoke.

Wagner<sup>(93,94)</sup> has analysed the conditions under which this 'active' oxidation occurs. This analysis predicts that there is a critical oxygen pressure

$$p_{\text{O}_2}(\text{crit}) \approx \frac{1}{2} P_{\text{SiO}}(\text{eq}) \quad (5)$$



above which a protective  $\text{SiO}_2$  layer forms on the surface (passive oxidation) and below which active oxidation occurs with the rate being controlled by the  $\text{SiO}$  flux away from the surface. Gulbransen et al.<sup>(95)</sup> have tested Wagner's prediction by oxidizing Si over a range of temperatures and oxygen pressures and found good agreement. The rate of Si consumption was approximately 300 times faster for oxygen pressures below  $p_{\text{O}_2}$  (crit) than those above it. Similar active-passive behavior has also been observed for Si-base ceramics such as  $\text{SiC}$  and  $\text{Si}_3\text{N}_4$  during oxidation at low oxygen pressures<sup>(96-98)</sup>. This phenomenon has not been reported for  $\text{SiO}_2$ -forming alloys.

## 1.2 Oxidation of $\text{SiO}_2$ -Forming alloys

The oxidation of Si-containing coatings has been reviewed recently by Grunling and Bauer<sup>(99)</sup>. Most of the work in this area has involved silicide coatings on refractory metals and superalloys in which the coatings are formed by Si-diffusion processes. The oxidation of these coatings is usually complex and difficult to characterize in terms of mechanisms.

Recently the oxidation of the silicides of a number of metals have been studied for use in microelectronic device fabrication. The oxidation of  $\text{TiSi}_2$ ,  $\text{CoSi}_2$ ,  $\text{NiSi}_2$ ,  $\text{Pd}_2\text{Si}$ ,  $\text{PtSi}$ ,  $\text{MoSi}_2$ ,  $\text{W}_2\text{Si}_5$  and  $\text{TaSi}_2$  results in the formation of  $\text{SiO}_2$  films which grow with a parabolic rate constant virtually the same as that for pure Si<sup>(100-102)</sup>. The linear rate constant, however, varies with the metallic element and is generally greater than that for pure Si. As for the case of Si, both rate constants are larger for oxidation in wet oxygen as compared to dry oxygen<sup>(102)</sup>.

Two studies<sup>(103,104)</sup> have been published on the oxidation of alloys in the binary Ni-Si system. Cocking et al.<sup>(103)</sup> studied the oxidation of solid solution alloys containing 0 to 5.2 wt. pct. Si in air at temperatures between 900 and 1200°C. The weight change versus time data at 1100°C are plotted in Figure 65. Increasing Si concentrations are seen to result in slower oxidation rates. The oxidation products were observed to contain  $\text{NiO}$ ,  $\text{SiO}_2$ , and  $\text{Ni}_2\text{SiO}_4$ . Kerr and Simkovich<sup>(104)</sup> studied the oxidation of alloys containing 0 to 10.1 wt. pct. Si at 1000°C in one atm of  $\text{O}_2$ . Small additions of Si up to 1 wt. pct. were observed to accelerate the oxidation rate which was explained as a doping effect of Si in the  $\text{NiO}$  scale. Oxidation rates continually decreased with increasing Si concentration above 2.5 wt. pct. Si. The weight change vs. time data for three of the alloys are plotted in Figure 66. The oxidation products responsible for the slower oxidation rates were not clearly identified.

## 2. Experimental

Binary Ni-Si alloys with nominal Si concentrations between 5 and 22.5 wt. pct. were prepared by tungsten arc melting under an argon atmosphere and drop casting into water cooled copper molds. The dimensions of the molds were 150 mm X 25 mm X 9 mm or 150 mm X 160 mm dia. The ingots were homogenized by heating in argon for 100 hrs. at 1150°C. Specimen shapes were either 12 mm X 9 mm X 2 mm or 16 mm dia. X 2 mm. The specimens were polished through 600 grit and ultrasonically cleaned in alcohol prior to oxidation testing.

Isothermal oxidation testing was performed by using a Cahn microbalance and a furnace assembly consisting of a quartz reaction tube and appropriate glassware to provide a gas tight system. The specimens were oxidized at temperatures between 900 and 1100°C in flowing dry air and weight changes were measured continuously as a function of time. Selected specimens were oxidized in air saturated with water vapor at 25°C.

Long term cyclic oxidation testing was carried out by exposing specimens in laboratory air in an apparatus which automatically removed the specimens from the furnace and reinserted them at selected time intervals. Each cycle consisted of 45 minutes isothermal oxidation followed by cooling for 15 minutes outside the furnace. The specimens were weighed after every 20 to 30 hours exposure time. Oxidation temperatures of 1000 and 1100°C were used. Selected specimens were also cycled in argon with a residual oxygen partial pressure of about  $10^{-5}$  atm.

Specimens were examined routinely by using optical metallography, scanning electron microscopy and x-ray diffraction. Some specimens were occasionally examined by using scanning auger microscopy and transmission electron microscopy.

### 3. Results and Discussion

The nominal and analyzed compositions of the alloys studied are presented in the following table. (Alloys will be referred to using the nominal compositions)

<u>Nominal Alloy Composition</u>	<u>Analyzed Si Content (wt%)</u>
Ni-5 Si	4.93
Ni-10 Si	9.51
Ni-12.5 Si	12.82
Ni-15 Si	14.28
Ni-17.5 Si	16.97
Ni-20 Si	17.83
Ni-22.5 Si	19.52

The analyzed Si contents (determined by atomic absorption analysis) show agreement with a comparison of the phases present and the published phase diagram for all except the 20 and 22.5 Si alloys. The microstructures of these alloys indicate the Si content is close to the nominal composition. This discrepancy is still being investigated.

The weight change vs. time data for alloys at 1100°C are presented in Figure 67. The significant features of these weight change curves are:

- (i) The oxidation data for Ni-5Si (also included in Figure 65) are in good agreement with those of Cocking<sup>(103)</sup>.
- (ii) The oxidation rates generally decrease with increasing Si concentration except for Ni-15Si which oxidizes at a rate greater than that of Ni-10Si and Ni-22.5Si which oxidizes slightly faster than Ni-20Si

- (iii) The rate of oxidation of Ni-20Si is comparable to or slower than that for current  $\text{Al}_2\text{O}_3$ -forming alloys under similar conditions
- (iv) Alloys containing greater than 10 wt% Si exhibit linear oxidation rates after a short initial period.

The oxide scale responsible for the slow kinetics for alloys with 10 percent or more silicon has been identified as  $\text{SiO}_2$ . For lower temperatures and shorter times this  $\text{SiO}_2$  film has been observed to be vitreous<sup>(105)</sup> (Figure 68). For long time exposures at temperatures of 900, 1000, and 1100°C the films were observed by x-ray diffraction to be crystalline with the tridymite structure. Therefore, at lower temperatures e.g. 900°-950°C the film forms as a vitreous layer and then devitrifies. It has not yet been determined if the same sequence occurs at higher temperatures but this is considered likely.

The exception of Ni-15Si to the trend of decreasing weight gains with increased Si content has not been completely explained. However, the error bars in Figure 67, which indicate the data variation for repetitive runs, indicate that this result is not due to experimental scatter. The shape of the weight gain curves in Figure 67 indicate that Ni-15Si may undergo more transient oxidation before the  $\text{SiO}_2$  becomes continuous. This could result from a decreased alloy interdiffusion coefficient in this alloy, which contains a significant fraction of the  $\text{Ll}_2$  - structure  $\beta$ -phase, but diffusion data are not available to test this hypothesis.

The linear oxidation rates for many of the alloys is somewhat surprising for alloys which oxidize as slowly as those in the Ni-Si system. The slopes of the weight change vs. time plots give linear rate constants in the range  $1 - 2 \times 10^{-3} \text{ mg/cm}^2/\text{hr}$  at 1100°C. Published data for the linear rate constant are  $0.1 \text{ mg/cm}^3/\text{hr}$  for oxidation of silicides such as  $\text{MoSi}_2$  and  $\text{WSi}_2$  and  $0.02 \text{ mg/cm}^3/\text{hr}$  for (100) Si. (These conversions were made from oxide thickness measurements using a density for  $\text{SiO}_2$  of  $2.27 \text{ g/cm}^3$ <sup>(101)</sup>). Therefore, it is concluded that the linear rates observed are not associated with the interface reaction for  $\text{SiO}_2$  growth. The linear rate can, however, be understood on the basis of Ni diffusion through a slowly growing  $\text{SiO}_2$  layer as shown schematically in Figure 69. If the Ni diffusion is rapid relative to the growth of the  $\text{SiO}_2$  layer the weight change of the specimen will be linear with time rather than following a parabolic time dependence. The continued formation of NiO on top of an  $\text{SiO}_2$  layer has, indeed, been observed for these alloys as seen in Figure 70 and 71 for a Ni-17.5Si alloy. After 15 minutes oxidation the alloys is covered with a thin, transparent oxide (apparently  $\text{SiO}_2$ , Figure 70, while after 180 hrs. the  $\text{SiO}_2$  layer is covered with crystals of NiO, Figure 71.

The effect of water vapor on the oxidation of two alloys (Ni-17.5Si and Ni-22.5Si) was also investigated by oxidizing both in dry air and air saturated with water at 25°C. As seen in Figure 72 there was no significant effect of water vapor on the oxidation rates. This is further evidence that the observed kinetics are associated with Ni transport rather than  $\text{SiO}_2$  growth since both  $k_p$  and  $K_1$  for  $\text{SiO}_2$  growth have been shown to be strongly influenced by the presence of water vapor in the oxidizing gas<sup>(92,102)</sup>.

The cyclic oxidation of four alloys was investigated in air at 1000 and 1100°C. Figure 73 shows that at 1000°C Ni-12.5Si begins to lose weight almost from the first cycle whereas Ni-15Si and Ni-22.5Si show a net weight loss after 150 and 400 hours respectively. The Ni-17.5Si alloy continued to gain weight for the duration of the experiment. Figure 74 shows that at 1100°C all four alloys show weight losses after a small number of cycles with Ni-12.5Si exhibiting considerably larger losses than the other alloys. (The Ni-22.5Si alloy was observed to change shape and dimensions during cyclic oxidation exposure due to a eutectoid transformation at 800°C). It has been observed at temperatures of 950°C and below the vitreous SiO<sub>2</sub> films formed on Ni-20Si are remarkably adherent and resistant to cyclic oxidation<sup>(105)</sup>. The difference between the observations at higher and lower temperatures is likely due, in part, to the greater thermal stresses generated for the higher temperatures. However, an additional factor is believed to be that the crystalline SiO<sub>2</sub> formed at higher temperatures is more likely to crack on cooling due to possible displacive transformations, e.g. upper tridymite to lower tridymite. Figure 75 shows the effect of reduced pO<sub>2</sub> on the cyclic oxidation of Ni-17.5Si and Ni-22.5Si. Reducing pO<sub>2</sub> by oxidizing in argon (residual pO<sub>2</sub> ≈ 10<sup>-5</sup> atm) is seen to have no measurable effect on Ni-22.5Si while it does decrease the weight loss from Ni-17.5Si. The latter may result from less NiO formation at the lower pO<sub>2</sub>.

Finally the effect of Low pO<sub>2</sub> on the oxidation of Ni-Si alloys and the possible existence of an active-passive transition<sup>(93-95)</sup> were investigated. No features associated with SiO volatilization were observed when the pO<sub>2</sub> was decreased to 10<sup>-5</sup> atm (argon) even at the highest temperatures studied. However, lowering the pO<sub>2</sub> to 10<sup>-15</sup> atm (H<sub>2</sub> - H<sub>2</sub>O) at 1150°C resulted in porosity in the alloy due to the selective volatilization of Si as SiO. This is illustrated in Figure 76 for Ni-20Si<sup>(105)</sup>. At this pO<sub>2</sub>  $P_{SiO} \gg pO_2$  satisfying the Wagner condition for active oxidation.

#### 4. Summary and Concluding Remarks

Alloys in the Ni-Si system (5 to 22.5 wt. pct. Si) have been oxidized in the temperature range 900 to 1100°C. Alloys containing approximately 20 wt. percent Si were found to oxidize extremely slowly at rates as slow or slower than those for α-Al<sub>2</sub>O<sub>3</sub> growth. The influence of alloy Si content, thermal cycling, reduced pO<sub>2</sub>, and the presence of water vapor in the oxidation rates of Ni-Si alloys have been described.

The results obtained from the studies on Ni-Si alloys show that silica barriers can be as effective as Al<sub>2</sub>O<sub>3</sub> in developing resistance to high temperature oxidation. Moreover, it also appears that silica barriers may provide improved protection for some metallic alloys where silica adherence is better than Al<sub>2</sub>O<sub>3</sub>. Of course, factors such as depression of the incipient melting points of alloys containing silicon and the brittle behavior of silicon - containing coatings will have to be evaluated for any new systems.

#### IV. REFERENCES

1. F. S. Pettit and G. W. Goward, "High Temperature Corrosion and Use of Coatings for Protection," Metallurgical Treatises, J. K. Tien and J. F. Elliott, ed., The Metallurgical Society of AIME, 1981, pp. 309-329.
2. R. L. Coble, "A Model for Boundary Diffusion Controlled Creep in Polycrystalline Materials," J. Appl. Phys., Vol. 34, 1963, pp. 1679-1682.
3. A. E. Paladino and R. L. Coble, "Effect of Grain Boundaries on Diffusion-Controlled Processes in Aluminum Oxide," J. Am. Ceram. Soc., Vol. 46, 1963, pp. 133-136.
4. T. S. Chow, "Adhesion of Brittle Films on a Polymeric Substrate," Adhesion, L. H. Lee, ed., American Chemical Society, 1975, pp. 687-705, Vol. 9B, Plenum Press, New York.
5. N. K. Adam, Physics and Chemistry of Surfaces, Oxford University Press, London, 1941, pp. 8.
6. M. Humenik Jr., and W. D. Kingery, "Metal-Ceramic Interactions: III, Surface Tension and Wettability of Metal-Ceramic Systems," J. Am. Ceram. Soc., Vol. 37, 1954, pp. 18-23.
7. J. E. McDonald and J. G. Eberhart, "Adhesion in Aluminum Oxide-Metal Systems," Trans. Met. Soc. of AIME, Vol. 233, 1965, pp. 512-517.
8. A. T. Fromhold Jr., "Stress in Dielectric Contact Layer on Metal," Surface Science, Vol. 22, 1972, pp. 396-410.
9. S. K. Benerji and C. L. Briant, "Intergranular Embrittlement in Steels," Canadian Metall. Quarterly, Vol. 18, 1980, pp. 169-175.
10. J. A. Pask and R. M. Fulrath, "Fundamentals of Glass-to-Metal Bonding: VIII, Nature of Wetting and Adherence," J. Am. Ceram. Soc., Vol. 45, No. 6, 1962, pp. 592-596.
11. H. E. Evans, "The Role of Oxide Grain Boundaries in the Development of Growth Stresses During Oxidation," Corro. Sci., Vol. 23, No. 5, 1983, pp. 495- 506.
12. J. Stringer, "Stress Generation and Relief in Growing Oxide Films," Corros. Sci., Vol. 10, 1970, pp. 513-543.
13. P. Hancock, and R. C. Hurst, "The Mechanical Properties and Breakdown of Surface Films at Elevated Temperatures," Advances in Corrosion Science and Technology, 1970, pp. 1-84, Vol. 4, Ed. Fontant, M. G. and Staehl, R. W., Plenum Press, New York.
14. N. B. Pilling and R. E. Bedworth, "The Oxidation of Metals at High Temperatures," J. Inst. Met., Vol. 29, 1923, pp. 529-591.
15. F. N. Rhines and J. S. Wolf, "The Role of Oxide Microstructure and Growth Stresses in the High-Temperature of Scaling of Nickel," Met. Trans., Vol. 1, 1970 pp. 1701-1710.

16. A. Atkinson, "Conditions for the Formation of New Oxide Within Oxide Films Growing on Metals," Corros. Sci., Vol. 22, No. 4, 1982, pp. 247-357.
17. A. G. Evans, G. B. Crumley, and R. E. Demaray, "On the Mechanical Behavior of Brittle Coatings and Layers," Oxidation of Metals, Vol. 20, No. 5-6, 1983, pp. 193-216.
18. C. H. Hsueh and A. G. Evans, "Oxidation Induced Stresses and Some Effects on the Behavior of Oxide Films," J. Appl. Phys., Vol. 54, No. 11, 1983, pp. 6672-6686.
19. F. A. Golightly, F. H. Stott, and G. C. Wood, "The Influence of Yttrium Additions on the Oxide Scale Adhesion to an Fe-Cr-Al Alloy," Oxidation of Metals, Vol. 10, No. 3, 1976, pp. 163-187.
20. T. E. Strangman, Thermal Fatigue of Oxidation Resistant Overlay Coatings for Superalloys, PhD Dissertation, University of Connecticut, 1978.
21. J. K. Tien and F. S. Pettit, "Mechanims of Oxide Adherence on Fe-25Cr-4Al(Y or Sc) Alloys," Met. Trans., Vol. 3, 1972, pp. 1587-1599.
22. F. H. Stott, G. C. Wood, and F. A. Golightly, "The Isothermal Oxidation Behavior of Fe-Cr-Al and Fe-Cr-Al-Y Alloys at 1200°C," Corros. Sci., Vol. 19, 1979, pp. 869-887.
23. J. L. Smialek and R. Gibala, "Structure of Transient Oxides Fomed on NiCrAl Alloys," Met. Trans. A, Vol. 14A, 1983, pp. 2143-2160.
24. J. E. Harris, "Vacancy Injection During Oxidation - A Reexamination of the Evidence," Acta Metall., Vol. 26, 1978, pp. 1033-1041.
25. D. P. Whittle and D. P. Boone, "Alumina Scale Adherence to CoCrAl Alloys and Coatings," Surfaces and Interfaces in Ceramic and Ceramic-Metal Systems, University of California Berkeley, 1982, pp. 487-502.
26. G. C. Wood and F. H. Stott, "The Development and growth of Protective  $\alpha\text{Al}_2\text{O}_3$  Scales and Alloys," High Temperature Corrosion, National Association of Corrosion Engineers, 1982, pp. 227-250, ed. R. A. Rapp.
27. F. S. Pettit, "Oxidation Mechanisms for Nickel-Aluminum Alloys at Temperatures Between 900 to 1300°C," Trans. Met. Soc. AIME, Vol. 239, 1967, pp. 1296-1305.
28. C. S. Giggins, and F. S. Pettit "Oxidation of Ni-Cr-Al Alloys Between 1000 and 1200°C," J. Electrochem. Soc., Vol. 118, 1971, pp. 1782-1790.
29. F. H. Stott, G. C. Wood, and M. G. Hobby, "A Comparison of the Oxidation Behavior of Fe-Cr-Al, Ni-Cr-Al, Co-Cr-Al Alloys," Oxidation of Metals, Vol. 3, 1971, pp. 103-113.
30. M. Sakiyama, P. Tomaszewicz, and G. R. Wallwork, "Oxidation of Iron-Nickel-Aluminum Alloys in Oxygen at 600-800°C," Oxidation of Metal, Vol. 13, 1979, pp. 311-330.

31. C. Wagner, "Passivity and Inhibition During the Oxidation of Metals at Elevated Temperatures," Corros. Sci., Vol. 5, 1965, pp. 751-764.
32. G. C. Wood, "High-Temperature Oxidation of Alloys," Oxidation of Metals, Vol. 2, 1970, pp. 11-57.
33. C. S. Giggins, and F. S. Pettit, "Oxide Scale Adherence Mechanisms and the Effects of Yttrium, Oxide Particles and Externally Applied Loads on the Oxidation of NiCrAl and CoCrAl Alloys," Tech. Report ARL-TR-75-0234, PWA-5364, Ad-A024104, Pratt & Whitney Aircraft Co., 1975.
34. I. M. Allam, D. P. Whittle, and J. Stringer, "The Oxidation Behavior of CoCrAl Systems Containing Active Element Additions," Oxidation of Metals, Vol. 12, No. 1, 1978, pp. 35-67.
35. I. M. Allam, D. P. Whittle, and J. Stringer, J., "Improvements in Oxidation Resistance by Dispersed Oxide Addition:  $\text{Al}_2\text{O}_3$  - Forming Alloys," Oxidation of Metals, Vol. 13, No. 4, 1979, pp. 381-401.
36. D. P. Whittle, M. E. El-Dahsahn, and J. Stringer, "The Oxidation Behavior of Cobalt-Base Alloys Containing Dispersed Oxides Formed by Internal Oxidation," Corros. Sci., Vol., 17, 1977, pp. 879-891
37. J. Stringer, "The Effect of Alloying and Oxidation - Quantitative Treatments," Metall. Rev., Vol. 11, 1966, pp. 113-128.
38. T. A. Ramanarayanan, M. Raghavan, and R. P. Luton, "The Characteristics of Alumina Scales Formed on Fe-Based Yttria-Dispersed Alloys," J. Electrochem. Soc., Vol. 131, No. 4, 1984, pp. 923-931.
39. H. M. Hindam, and W. W. Smeltzer, "Applications of Auger Electron Spectroscopy and Inert Metal Marker Techniques to Determine Metal and Oxygen Transport in Oxide Films on Metals," Oxidation of Metals, Vol. 14, No. 4, 1980, pp. 337-349.
40. Y. Oishi, and W. D. Kingery, "Self-Diffusion of Oxygen in Single Crystal and Polycrystalline Aluminum Oxide," J. Chemical Physics, Vol. 33, 1962, pp. 480-486.
41. K. P. R. Reddy, Oxygen Diffusion in Close Packed Oxides, PhD Dissertation, Case Western Reserve University, Cleveland, Ohio, 1979.
42. J. L. Smialek, and R. Gibala, "Diffusion Processes in  $\text{Al}_2\text{O}_3$  Scales: Void Growth, Grain Growth, and Scale Growth," High Temperature Corrosion, R. A. Rapp, ed., National Association of Corrosion Engineers, 1982, pp. 274-283.
43. K. P. R. Reddy, J. L. Smialek and A. R. Cooper,  $^{18}\text{O}$  Tracer Studies of  $\text{Al}_2\text{O}_3$  Scale Formation on NiCrAl Alloys," Oxidation of Metals, Vol. 17, No. 5-6, 1982, pp. 429-449.
44. C. S. Giggins and F. S. Pettit, "The Oxidation of TD NiC (Ni-20Cr-2 vol. pct.  $\text{ThO}_2$ ) Between 900 and 1200°C," Met. Trans., Vol. 2, 1971, pp. 1071-1078.

45. J. C. Pivin, et. al., "Oxidn. Mech. of Fe-Ni-20-25Cr-5Al Alloys - Influence of Small Amounts of Yttrium on Oxidn. Kinetics and Oxide Adherence," Corros. Sci., Vol. 20, 1980, pp. 351-373.
46. A. Tadaaki, S. Yajima, and Y. Saito, "High Temperature Oxidation Behavior of Fe-20Cr-4Al Alloys with Small Additions of Cerium," Trans. JIM, Vol. 20, 1979, pp. 431-441.
47. J. L. Smialek, "The Relationship Between Oxide Grain Morphology and Growth Mechanisms for Fe-Cr-Al and Fe-Cr-Al-Y Alloys," J. Electrochem. Soc., Vol. 126, 1979, pp. 2275.
48. F. A. Golightly, G. C. Wood, and F. H. Stott, "The Early Stages of Development of  $\alpha$ -Al<sub>2</sub>O<sub>3</sub> Scales on Fe-Cr-Al and Fe-Cr-Al-Y Alloys at High Temperature," Oxidation of Metals, Vol. 14, No. 3, 1980, pp. 217-234.
49. J. M. Francis and W. H. Whitlow, "The Effects of Yttrium on the High Temperature Oxidation resistance of Some Fe-Cr Base Alloys in CO<sub>2</sub>," Corros. Sci., Vol. 5, 1965, p. 701-710.
50. D. Delaunay, A. M. Huntz, and P. LaCombe, "The Influence of Yttrium on the Sintering of Al<sub>2</sub>O<sub>3</sub>," J. of Less Comm. Met., Vol. 70, 1980, pp. 115-117.
51. D. Delaunay, A. M. Huntz, and P. LaCombe, "Mech. Stress Develop. in High Temp. Resistt. Alloys During Iso. Thermal and Cyclic Oxidn. Treatments," Corros. Sci., Vol. 20, 1980, pp. 1109-1117.
52. R. W. Davidge, Mechanical Behaviour of Ceramics, Cambridge University Press, Cambridge, U. K., 1980.
53. R. M. Cannon, W. H. Rhodes, and A. H. Heuer, "Plastic Deformation of Fine-Grained Alumina Al<sub>2</sub>O<sub>3</sub>: I, Interface-Controlled Diffusional Creep," J. Am. Ceram. Soc., Vol. 63, No. 1-2, 1980, pp. 46-53.
54. S. I. Warshaw, and F. H. Norton, "Deformation Behavior of Polycrystalline Aluminum Oxide," J. Am. Ceram. Soc., Vol. 45, 1962, pp. 479.
55. P. A. Lessing, and R. S. Gordon, "Impurity and Grain Size Effects on the Creep of Polycrystalline Magnesia and Alumina," Deformation of Ceramic Materials, R. C. Bradt, and R. E. Tressler, ed., Pennsylvania State University, 1975, pp. 271-296, Plenum Press, New York.
56. G. W. Hollenberg, and R. S. Gordon, "Effect of Oxygen Partial Pressure on the Creep of Polycrystalline Al<sub>2</sub>O<sub>3</sub> Doped with Cr, Fe, or Ti," J. Am. Ceram. Soc., Vol. 56, 1973, pp. 140-147.
57. M. M. El-Aiat, and F. A. Kroger, "Yttrium, an Isoelectric Donor in  $\alpha$ -Al<sub>2</sub>O<sub>3</sub>," J. Am. Ceram. Soc., Vol. 65, No. 6, 1982, pp. 280-283.
58. H. A. Kumar, M. Nasrallah, D. L. Douglass, "The Effect of Yttrium and Thorium on the Oxidation Behavior of Ni-Cr-Al Alloys," Oxidation of Metals, Vol. 8, 1974, pp. 227-263.



59. H. Pfeiffer, "Über den Einfluß von Spurenelementen auf die Zunderbeständigkeit hitzebeständiger Legierungen," Werkst u Korrr., Vol. 8, 1957, pp. 574-579.
60. H. Pfeiffer and G. Sommer, "Untersuchungen zur Klärung der Wirkungsweise von Zusatzelementen in Heizleiterlegierungen," Z. Metallunde, Vol. 57, 1966, pp. 326-331.
61. A. W. Funkenbusch, and J. G. Smeggil, "A Study of Adherent Oxide Formation," Tech. Report R83-916154-1, United Technologies Research Center, East Hartford, Connecticut 06108, 1983.
62. J. D. Kuenzly, and D. L. Douglass, "The Oxidation Mechanims of  $\text{Ni}_3\text{Al}$  Containing Yttrium," Oxidation of Metals, Vol. 8, No. 3, 1974, pp. 139-178.
63. D. P. Whittle, and J. Stringer, "Improvement in High Temperature Oxidation Resistance by Additions to Reactive Elements or Oxide Dispersions," Phil. Trans. R. Soc. Lond., Vol. A 295, 1980, pp. 309-329.
64. S. Y. Hwang, "The Initial Stages of Oxidation and Hot Corrosion of  $\text{CoCrAlY}$  at  $700^\circ\text{C}$ , Master's Thesis, University of Pittsburgh, 1983.
65. B. Lustmann, "The Intermitent Oxidation of Some Nickel-Chromium Base Alloys," Trans. Metall. Soc. of AIME, Vol. 188, 1950, pp. 995-996.
66. C. S. Wukusick, and J. F. Collins, "Oxidation of an Iron-Chromium-Aluminum Containing Yttrium," Mater. Res. Stand, Vol. 4, 1964, pp. 637-647.
67. D. O. Harris, A. S. Tetelman, and F. A. Darwish, "Detection of Fiber Cracking By Acoustic Emission," Acoustic Emission, ASTM STP 505, American Society for Testing and Materials, 1972, pp. 238-249.
68. A. A. Pollock, "Acoustic Emissions Amplitudes," Non-Destructive Testing, Vol. 6, 1973, pp. 264-269.
69. A. Rotem, and E. Altus, "Fracture Modes and Acoustic Emission of Composite Materials," J. Testing and Evaluation, Vol. 7. No. 1, 1979, pp. 33-40.
70. K. Ono, "Amplitude Distribution Analysis of Acoustic Emission Signals," Material Evaluation, Vol. 34, No. 8, 1976, pp. 177-181, 184.
71. W. W. Gerberich, and C. E. Hartbower, "Some Observations on Stress Wave Emission as a Measure of Crack Growth," Int. J. Fracture Mechanics, Vol. 3, 1976, pp. 185-192.
72. W. W. Gerberich, D. G. Atteridge, and J. F. Lessar, "An Acoustic Emission Investigation of Microscopic Ductile Fracture," Metall. Trans., Vol. 6A, 1975, pp. 797-801.
73. H. Hindam, and D. P. Whittle, "Peg Formation by Short-Circuit Diffusion in  $\text{Al}_2\text{O}_3$  Scales Containing Oxide Dispersions," J. Electrochem. Soc., Vol. 129, 1982, pp. 1147-1149.

74. A. S. Kahn, C. E. Lowell, and C. A. Barrett, "The Effect of Zirconium on the Isothermal Oxidation of Nominal Ni-14Cr-24Al Alloys," J. Electrochem. Soc., Vol. 127, 1980, pp. 670-679.
75. D. Bruce and P. Hancock, "Influence of Mechanical Properties of Surface Oxide Films on Oxidation Mechanisms, I-II," J. of Ins. Metals, Vol. 1969, pp. 140-155.
76. R. A. Perkins, G. H. Meier, "Acoustic Emission Studies on High Temperature Oxidation," High Temperature Materials Chemistry - II, Z. A. Munir and D. Cubicciotti, ed., The Electrochemical Society Inc., Pennington, NJ 08534-2806, 1984, pp. 176-189.
77. H. E. Evans, and R. C. Lobb, "Conditions for the Initiation of Oxide-Scale Cracking and Spallation," Corro. Sci., Vol. 24, No. 3, 1984, pp. 209-222.
78. C. A. Barrett, and C. E. Lowell, "The Cyclic Oxidation Resistance of Co-Cr-Al Alloys at 1100 and 1200°C and a Comparison with the Ni-Cr-Al Alloy Systems," Oxidation of Metals, Vol. 12, No. 4, 1978, pp. 283-311.
79. C. E. Lowell, R. G. Garlic, and B. Henry, "Thermal Expansion in the Ni-Cr-Al and Co-Cr-Al Systems to 1200°C Determined by High-Temperature X-Ray Diffraction," Metall. Trans. A, Vol. 7A, 1976, pp. 655-660.
80. F. S. Pettit, Trans. Met. Soc. AIME, Vol. 239, 1967, p. 1296.
81. G. C. Wood, and F. S. Stott, "The Development and Growth of Protective - Al<sub>2</sub>O<sub>3</sub> Scales on Alloys," High Temperature Corrosion, R. A. Rapp, ed., NACE, 1983, p. 227,
82. B. E. Deal and A. S. Grove, J. Appl. Phys., Vol. 36, 1965, p. 3770.
83. E. Rochet, B. Agins, and S. Rigo, J. Electrochem. Soc., Vol. 131, 1984, p. 914.
84. F. A. Kroger, "Defects and Transport in SiO<sub>2</sub>, Al<sub>2</sub>O<sub>3</sub> and Cr<sub>2</sub>O<sub>3</sub>," High Temperature Corrosion, R. A. Rapp, ed., NACE, 1983, p. 89.
85. A. G. Revezzy and H. A. Schaeffer, J. Electrochem. Soc., Vol. 129, 1982, p. 357.
86. E. A. Irene, J. Electrochem. Soc., Vol. 129, 1982, p. 413.
87. E. A. Irene, J. Appl. Phys., Vol. 54, 1983, p. 5416.
88. J. M. Gibson, and D. W. Dong, J. Electrochem. Soc., Vol. 127, 1980, p. 2722.
89. S. M. Hu, J. Appl. Phys., Vol. 55, 1984, p. 4095.
90. D. R. Wolters, J. Electrochem. Soc., Vol. 127, 1980, p. 2075.
91. A. Fargeix, and G. Ghibaudo, J. Appl. Phys., Vol. 56, 1984, p. 589.
92. R. B. Marcus, and T. T. Sheng, J. Electrochem. Soc., Vol. 129, 1982, p. 1278.
93. C. J. Wagner, Appl. Phys., Vol. 29, 1958, p. 1295.

94. C. Wagner, Corros. Sci., Vol. 5, 1965, p. 751.
95. E. A. Gulbransen, K. F. Andrew, and F. A. Brassrt, J. Electrochem. Soc., Vol. 113, 1966, p. 834.
96. J. W. hinze, W. C. Tupp, and H. C. Graham, "Active Oxidation Phenomena in Silicon and Silicon-Based Materials," in Metal-Slag, Gas Reactions and Processes, Z. A. Foroulis and W. W. Smeltzer, eds., The Electrochem. Soc., 1975, p. 391.
97. L. H. Keys, "The Oxidation of Silicon Carbide," in Properties of High Temperature Alloys, Z. A. Foroulis and F. S. Pettit, eds., The Electrochem. Soc., 1976, p. 681.
98. S. C. Singhal, "Oxidation of Silicon-Based Structural Ceramics," in Properties of High Temperature Alloys, Z. A. Foroulis and F. S. Pettit, eds., The Electrochem. Soc., 1976, p. 697.
99. H. W. Grunling and R. Bauer, Thin Solid Films, Vol. 95, 1982, p. 3.
100. M. Bartur, Thin Solid Films, Vol. 107, 1983, p. 55.
101. M. Bartur, and M. A. Nicolet, J. Electronic Mater., Vol. 13, 1984, p. 81.
102. L. N. Lie, W. A. Tiller, and K. C. Sarasuat, J. Appl. Phys., Vol. 56, 1984, p. 2127.
103. J. L. Cocking, L. D. Palmer, N. A. Burley, and G. R. Johnston, "High Temperature Oxidation of Alpha Nickel-Silicon," to be published in Oxidation of Metals.
104. J. W. Kerr and G. Simkovich, "Hot Corrosion Studies on Nickel-Based Alloys Containing Silicon" in Properties of High Temperature Alloys, Z. A. Foroulis and F. S. Pettit, eds., The Electrochem. Soc., 1976, p. 576.
105. G. M. Kim, and G. H. Meier, unpublished research on Martin Marietta Subcontract 19X-43369C.

**Table I**  
Chemical Compositions of the Alloys Studied :  
(Nominal Weight Percents)

Alloy Designation	Ni	Co	Cr	Al	Y	Hf
NiCrAl	bal	—	20	10	—	—
NiCrAl—0.02Y	bal	—	20	10	0.02(0.0084)	—
NiCrAl—0.2Y	bal	—	20	10	0.2(0.071)	—
NiCrAl—0.8Y	bal	—	20	10	0.8(0.89)	—
NiCrAl—0.3Hf	bal	—	20	10	—	0.3(0.27)
NiCrAl—1.0Hf	bal	—	20	10	—	1.0(0.98)
CoCrAl	—	bal	20	10	—	—
CoCrAl—0.2Y	—	bal	20	10	0.2(0.066)	—
CoCrAl—1.0Hf	—	bal	20	10	—	1.0(1.0)

Numbers in parentheses denote the analyzed alloy content.

**Table II**

AE Counts per Unit Spalled Area

	Total AE Counts	Spalled Area (cm <sup>2</sup> )	AE Count/Spalled Area (counts/cm <sup>2</sup> )
NiCrAl	2.63 10 <sup>6</sup>	2.772	0.95 10 <sup>6</sup>
CoCrAl	1.66 10 <sup>6</sup>	1.431	1.16 10 <sup>6</sup>
NiCrAl-0.2Y	3.20 10 <sup>5</sup>	0.019	16.84 10 <sup>6</sup>
NiCrAl-1.0Hf	4.43 10 <sup>5</sup>	0.018	24.61 10 <sup>6</sup>

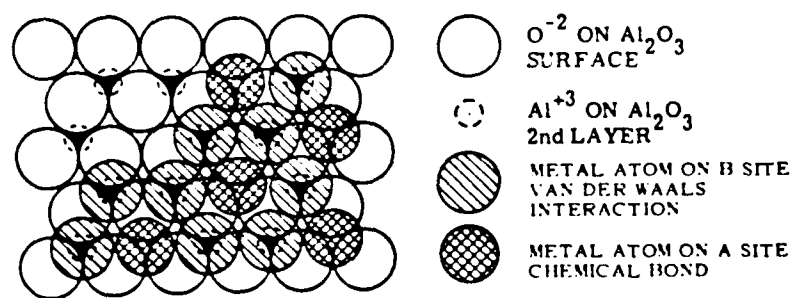


Figure 1: The 0001 surface of sapphire showing the location of type A and B surface sites.

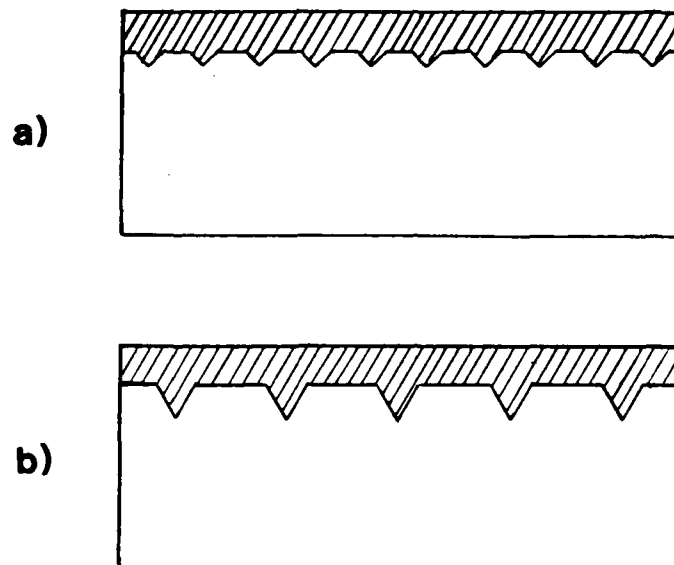


Figure 2: Schematic diagram of oxide intrusions at the scale/substrate interface, (a) small size closely spaced, (b) large size widely spaced.

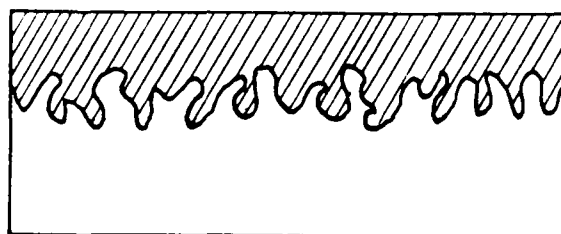


Figure 3: Mechanical interlocking of scale and substrate via a geometrically irregular interface.

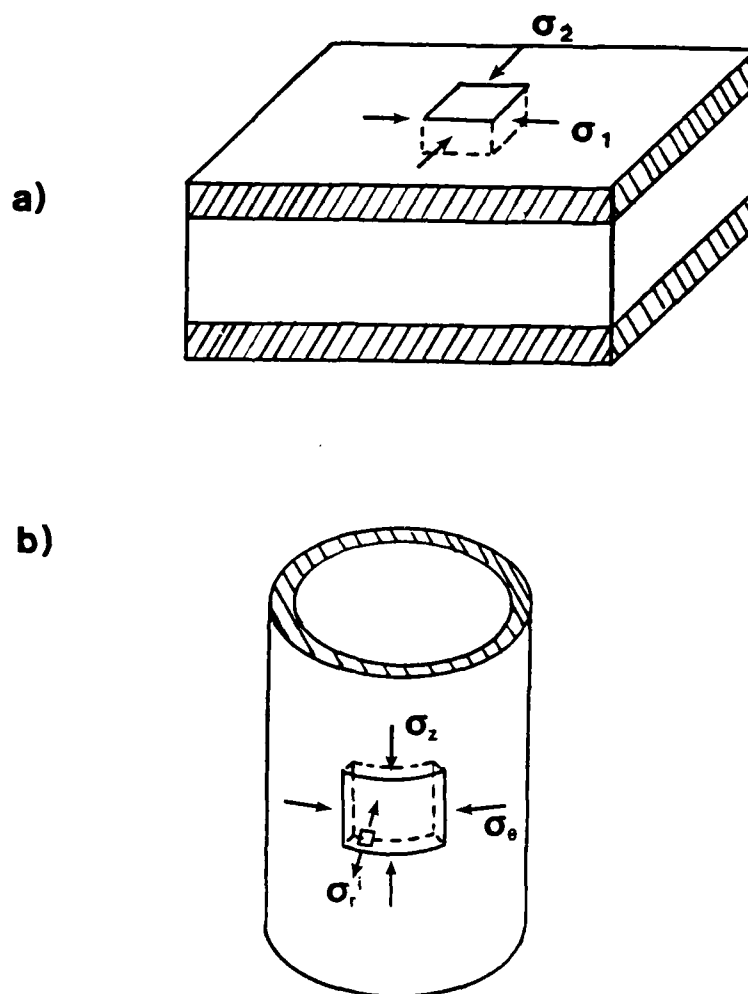


Figure 4: Biaxial compressive stresses in oxide scales, (a) scale on a flat substrate, (b) scale on a cylindrical substrate.



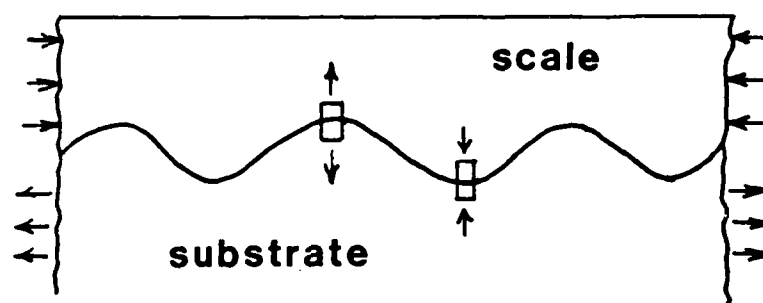
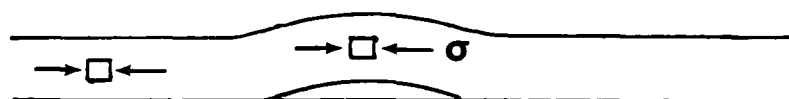
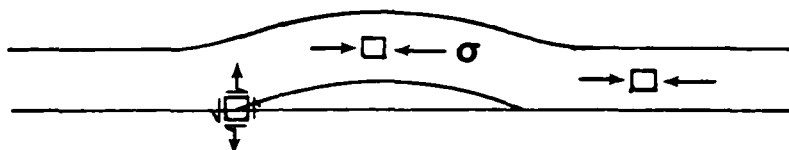


Figure 5: Stress distribution along a wavy scale/substrate interface.

a)



b)



c)

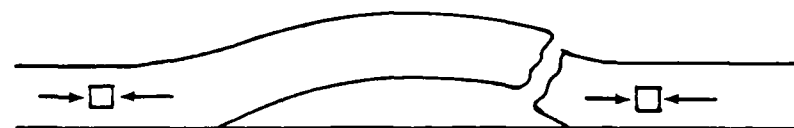


Figure 6: Schematic representation of the steps involved in the oxide scale failure process under biaxial compression.

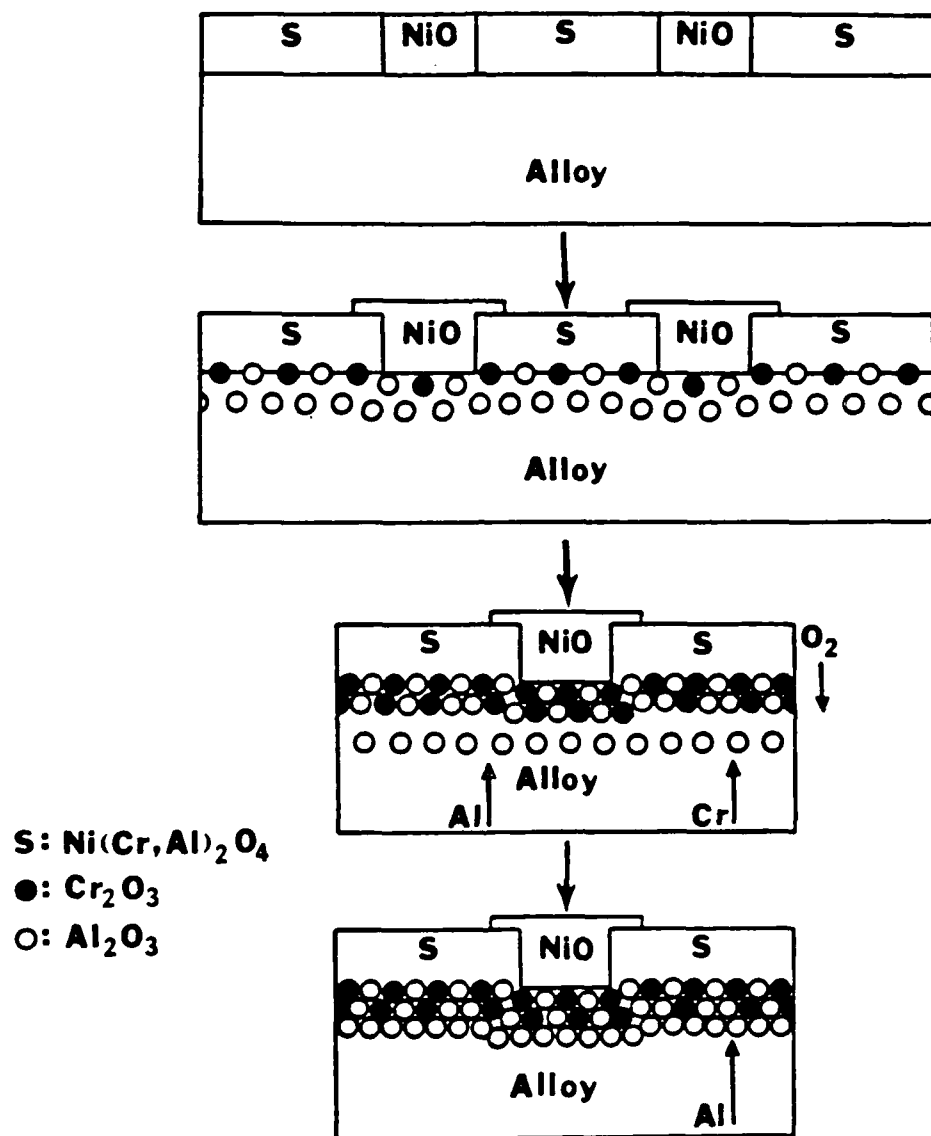


Figure 7: Schematic diagram illustrating the processes by which continuous  $\text{Al}_2\text{O}_3$  layers developed on NiCrAl alloys.

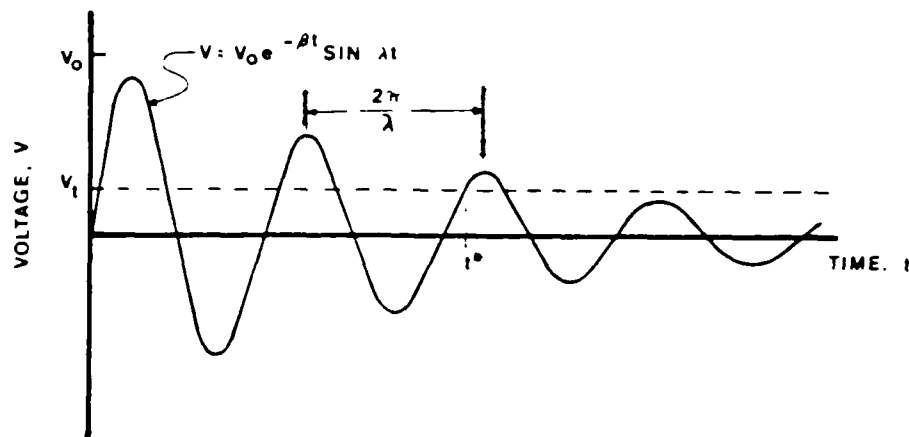


Figure 8: Schematic of a damped sinusoid signal, showing threshold voltage, and the multiple counts from a single event within the test piece.

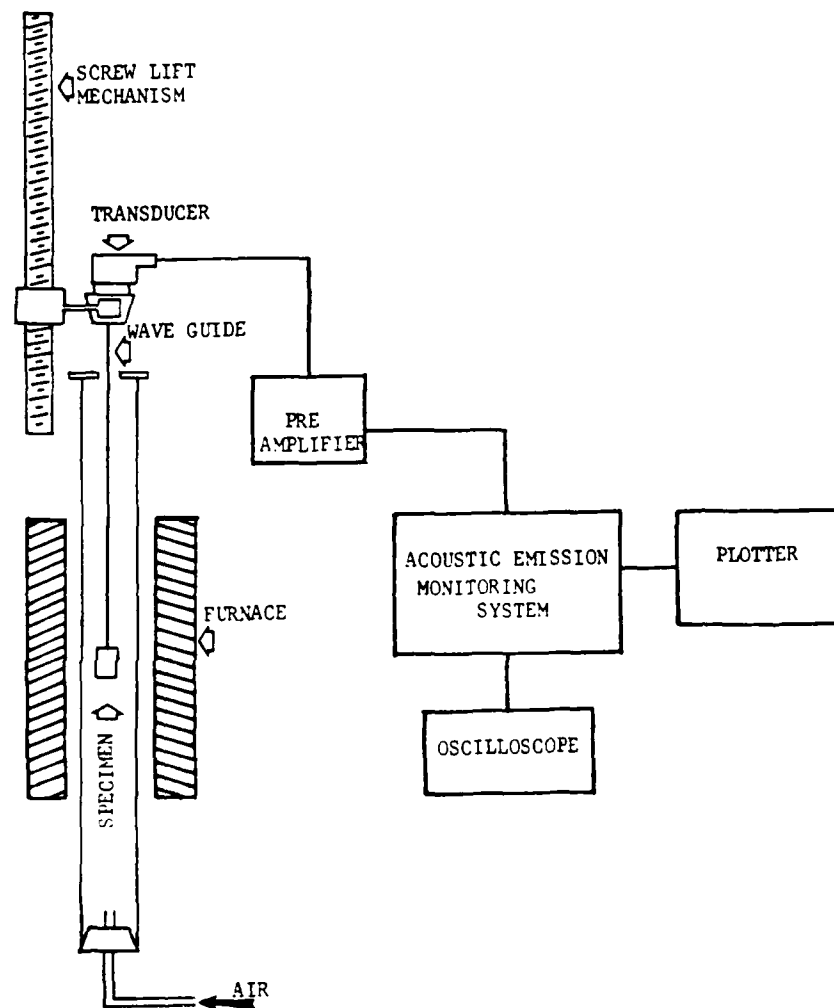


Figure 9: Experimental setup for the acoustic emission study of oxide scale failure.

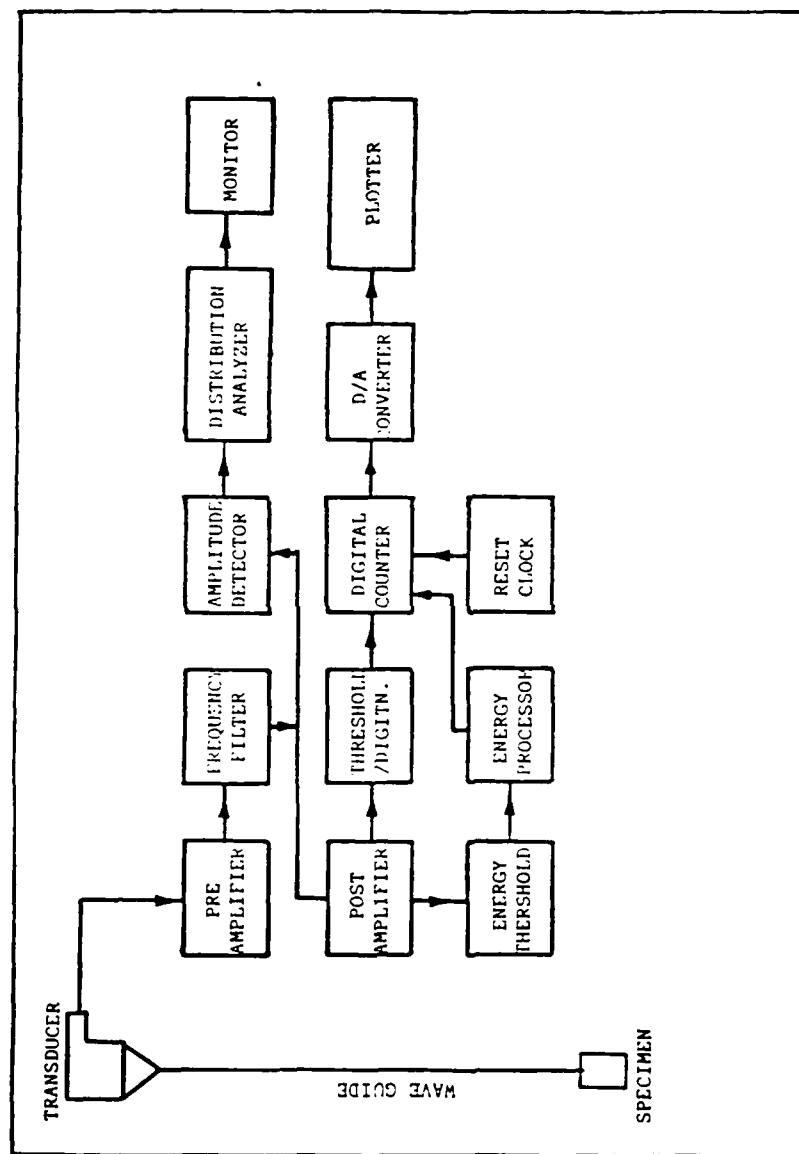


Figure 10: Function block diagram of the acoustic emission detection system.

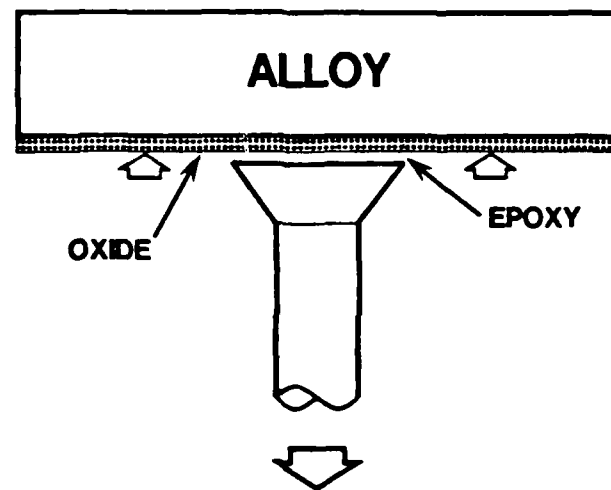


Figure 11: Schematic diagram illustrating the mechanical stripping of oxide scale.

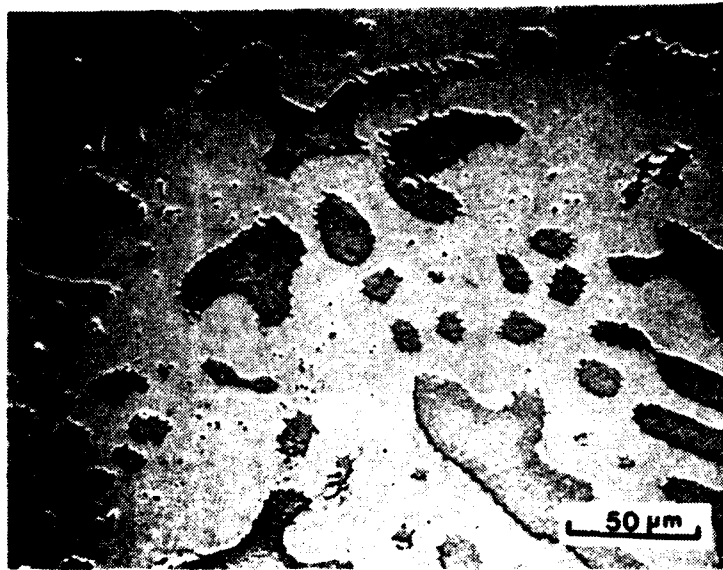


Figure 12: A typical microstructure of the NiCrAl alloys.  
Primary dendrites of  $\beta$  (NiAl) in  $\gamma+\gamma'$  matrix.



Figure 13: Microstructure of a NiCrAl alloy at higher magnification.



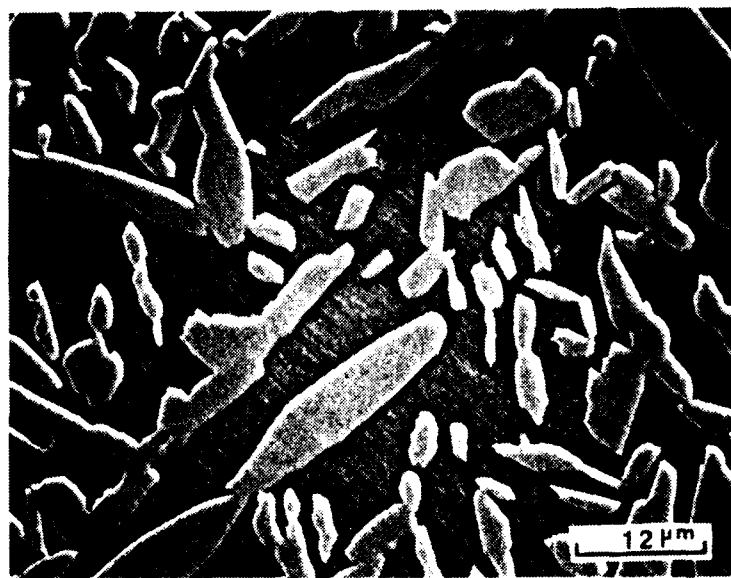


Figure 14: A typical microstructure of the CoCrAl alloys.

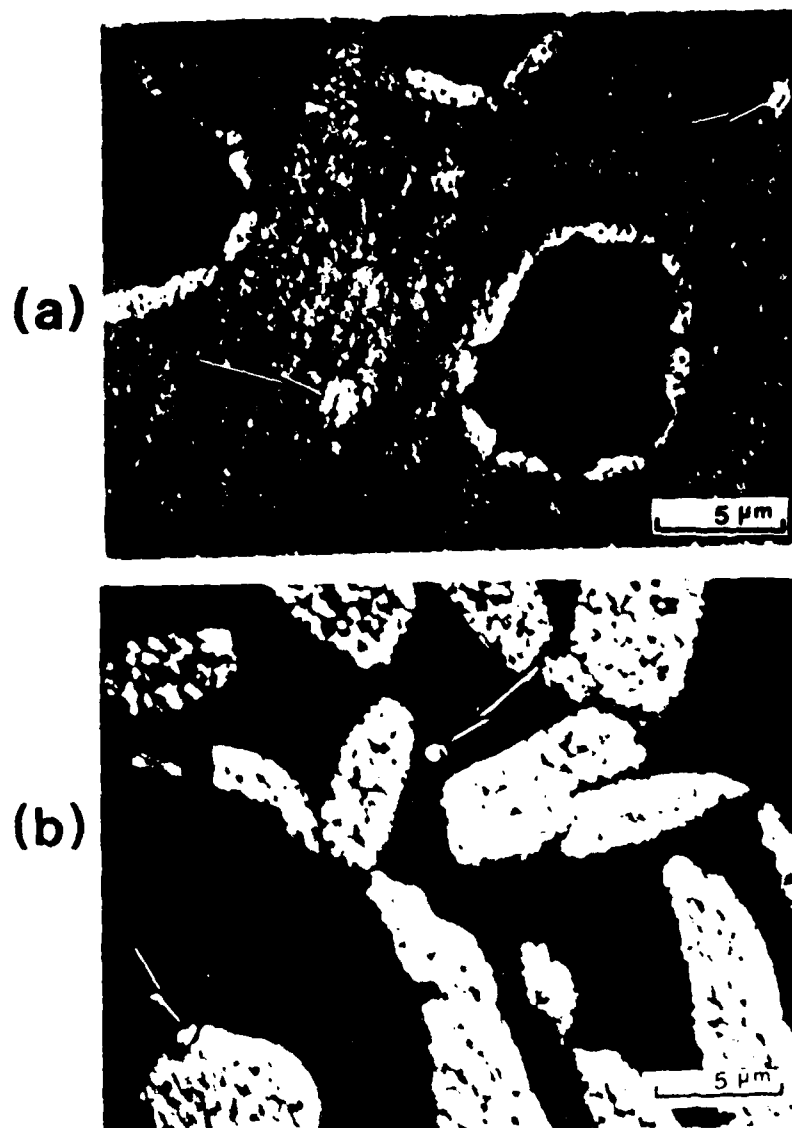


Figure 15: Photomicrographs showing the yttride particles in the heat-treated specimens. (a) NiCrAl-0.2Y, 1100°C/100h/air.

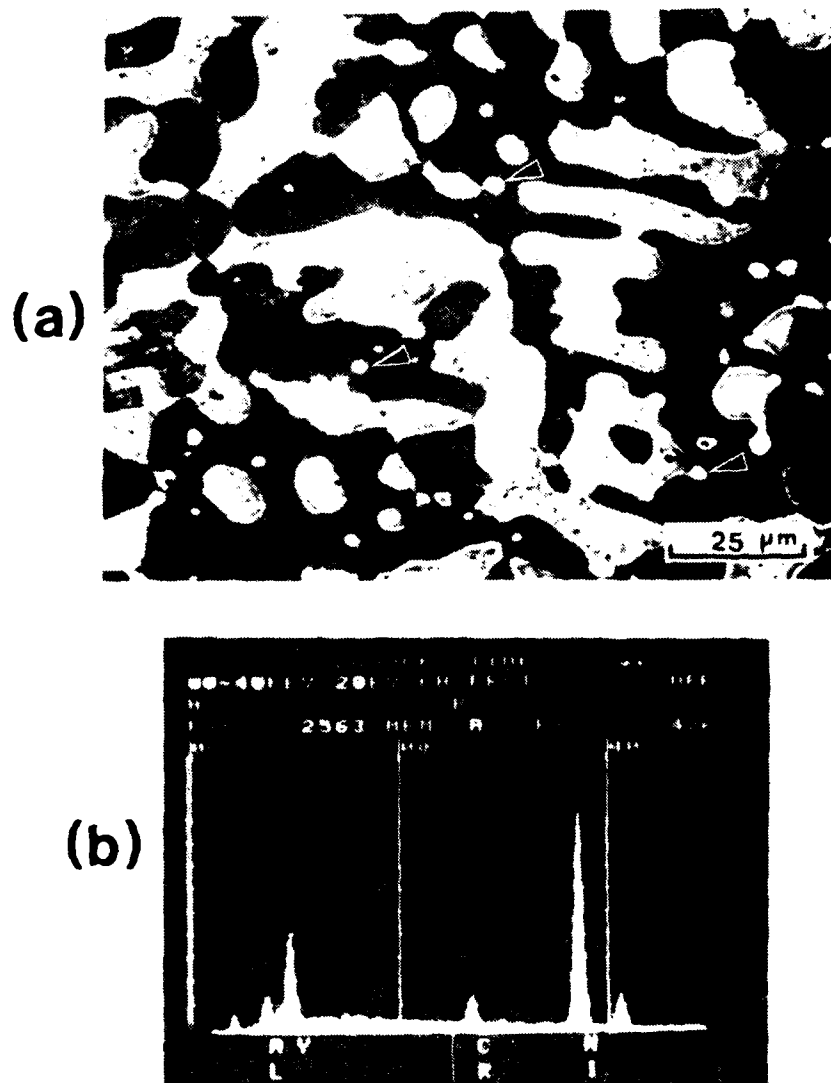
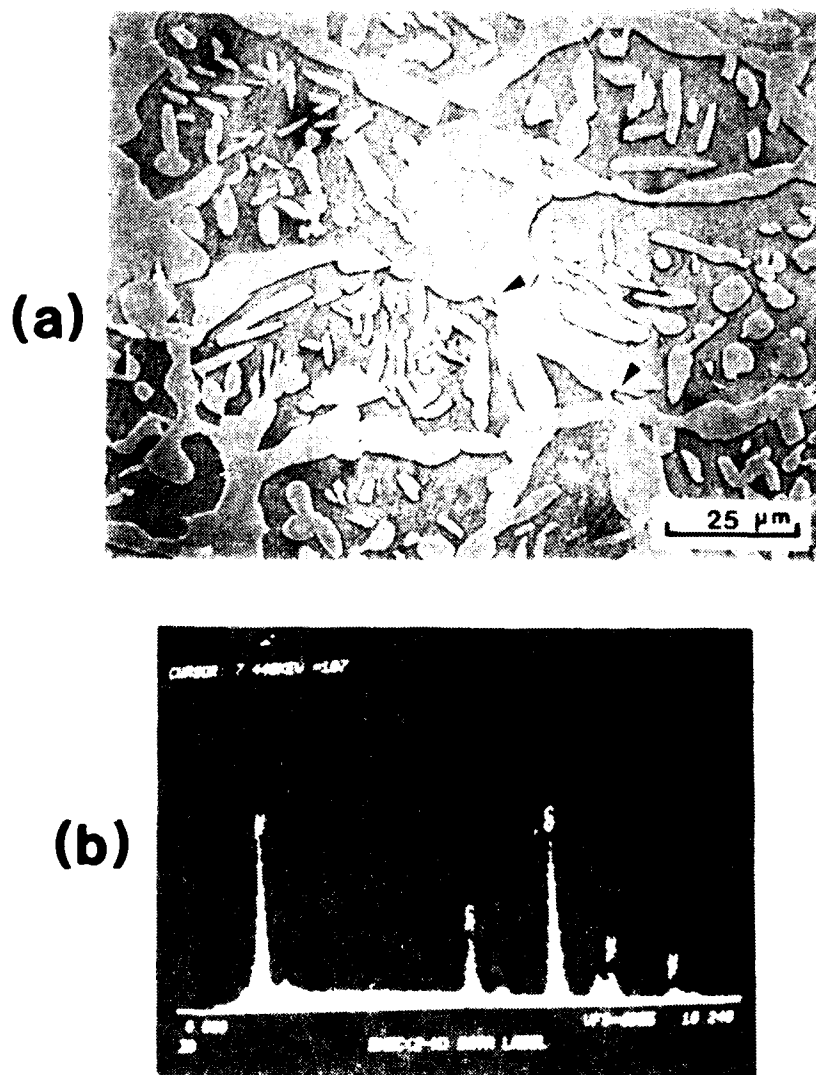


Figure 16: Yttre phase in NiCrAl-0.6Y alloy. (a) Photograph showing the microstructure of the alloy containing yttre phase (round white particles). (b) EDAX spectrum of the yttre phase in (a).



**Figure 17:** Intermetallic hafnium phase in  $\text{Cu-7Al-1.0Hf}$  alloy.  
 (a) Photograph showing the microstructure of the alloy, arrows indicating the intermetallic phase of hafnium.  
 (b) EDAX spectrum of an intermetallic phase in (a).

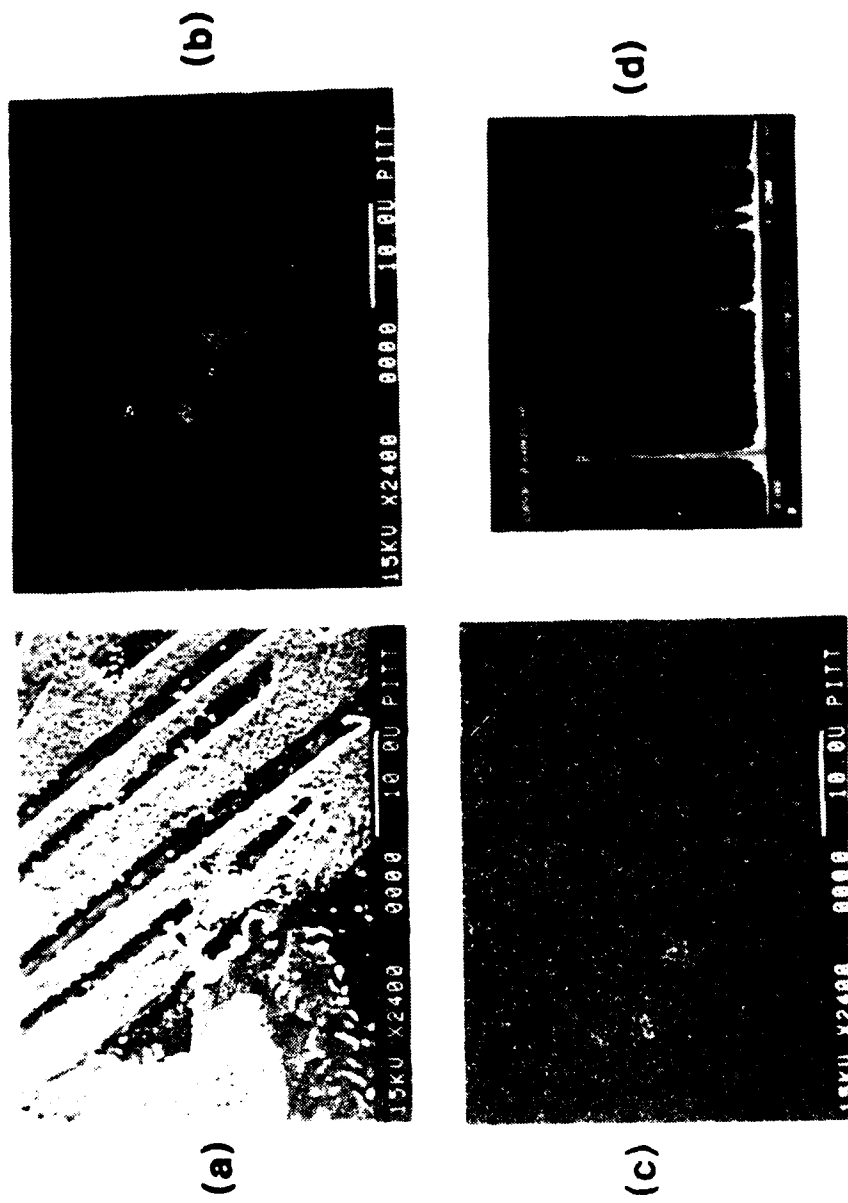


Figure 18: Hafnium oxide particles in NiCrAl-1.0Hf alloy. (a) Photograph showing the microstructure of the alloy, arrows indicating the hafnium oxide particles, (b) and (c) are the X-ray maps of hafnium and oxygen, respectively; (d) EDAX of the oxide particles.

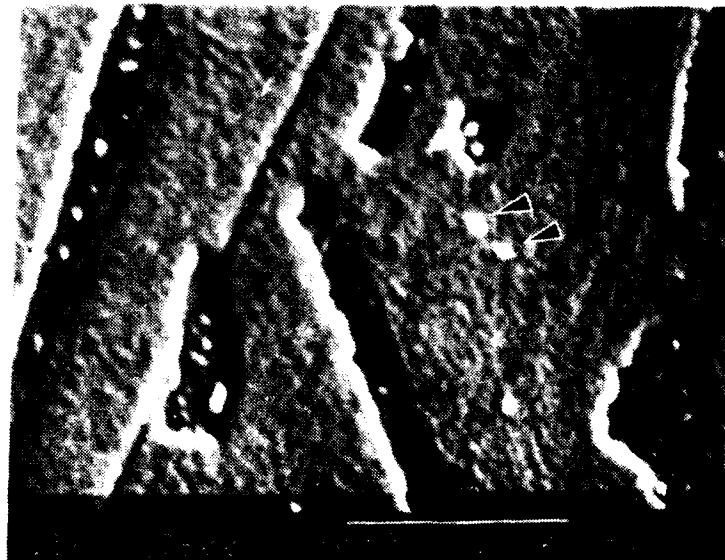


Figure 19: Hafnium oxide particles (arrows) in NiCrAl-0.3Hf alloy.

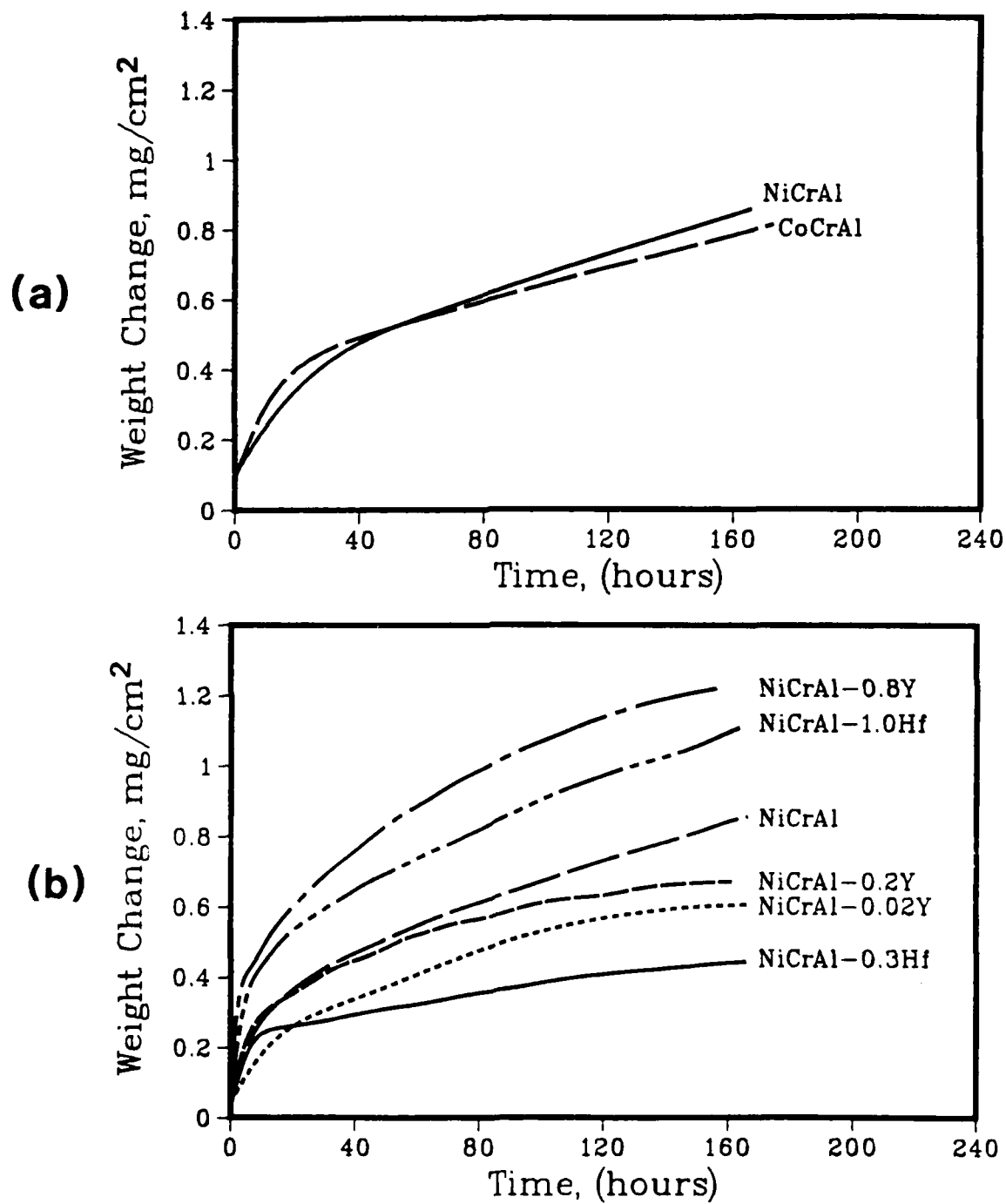


Figure 20: Weight change data for the isothermal oxidation of specimens at 1100°C, (a) undoped NiCrAl and CoCrAl alloys, (b) NiCrAl alloys doped with yttrium or hafnium, (continued).

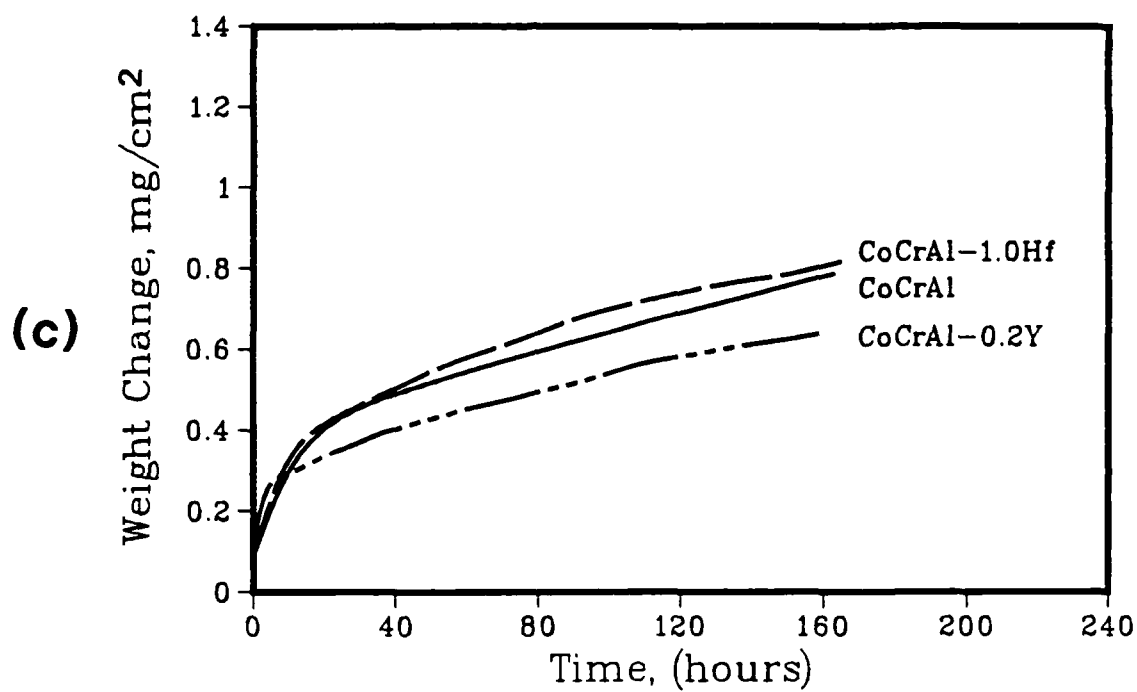


Figure 20: (Continued), weight change data for the isothermal oxidation of specimens at 1100°C, (c) CoCrAl alloys doped with yttrium or hafnium.



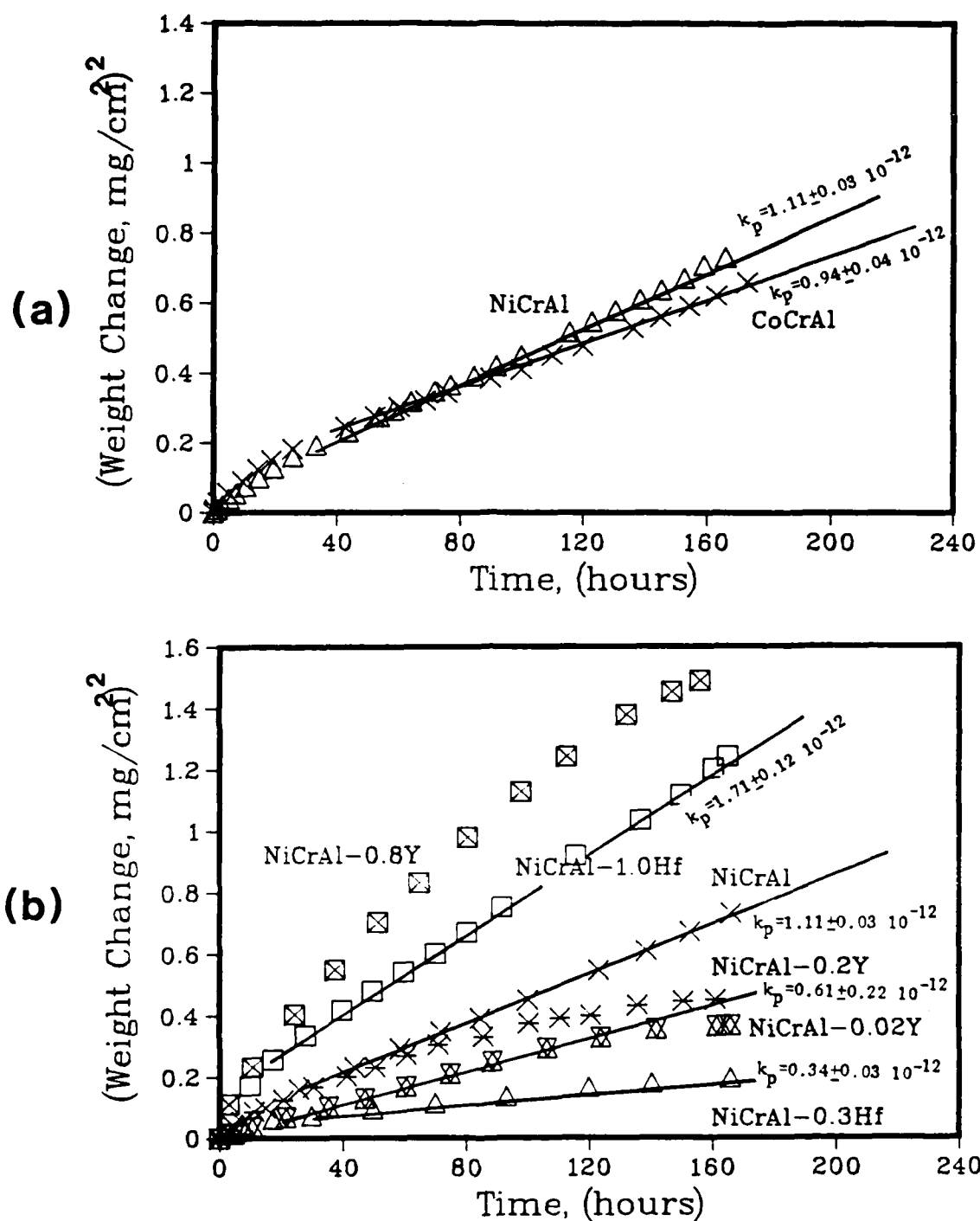


Figure 21: Weight change squared vs time plot for the isothermally oxidized specimens at 1100°C, (a) undoped NiCrAl and CoCrAl alloys, (b) NiCrAl alloys doped with yttrium or hafnium. Values of parabolic rate constant ( $k_p$ ) are given in gm<sup>2</sup>/cm<sup>4</sup>-sec, (continued).

(c)

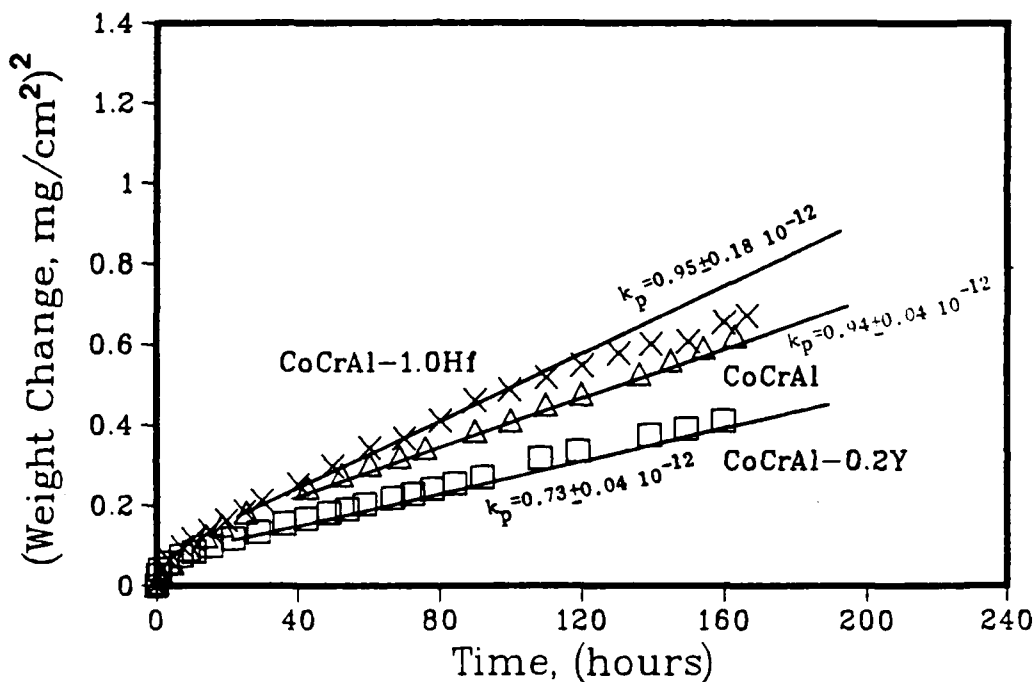


Figure 21: (Continued), weight change squared vs time plot for isothermally oxidized specimens at  $1100^\circ\text{C}$ , (c) CoCrAl alloys doped with yttrium or hafnium. Values of parabolic rate constant ( $k_p$ ) are given in  $\text{gm}^2/\text{cm}^4\text{-sec}$ .

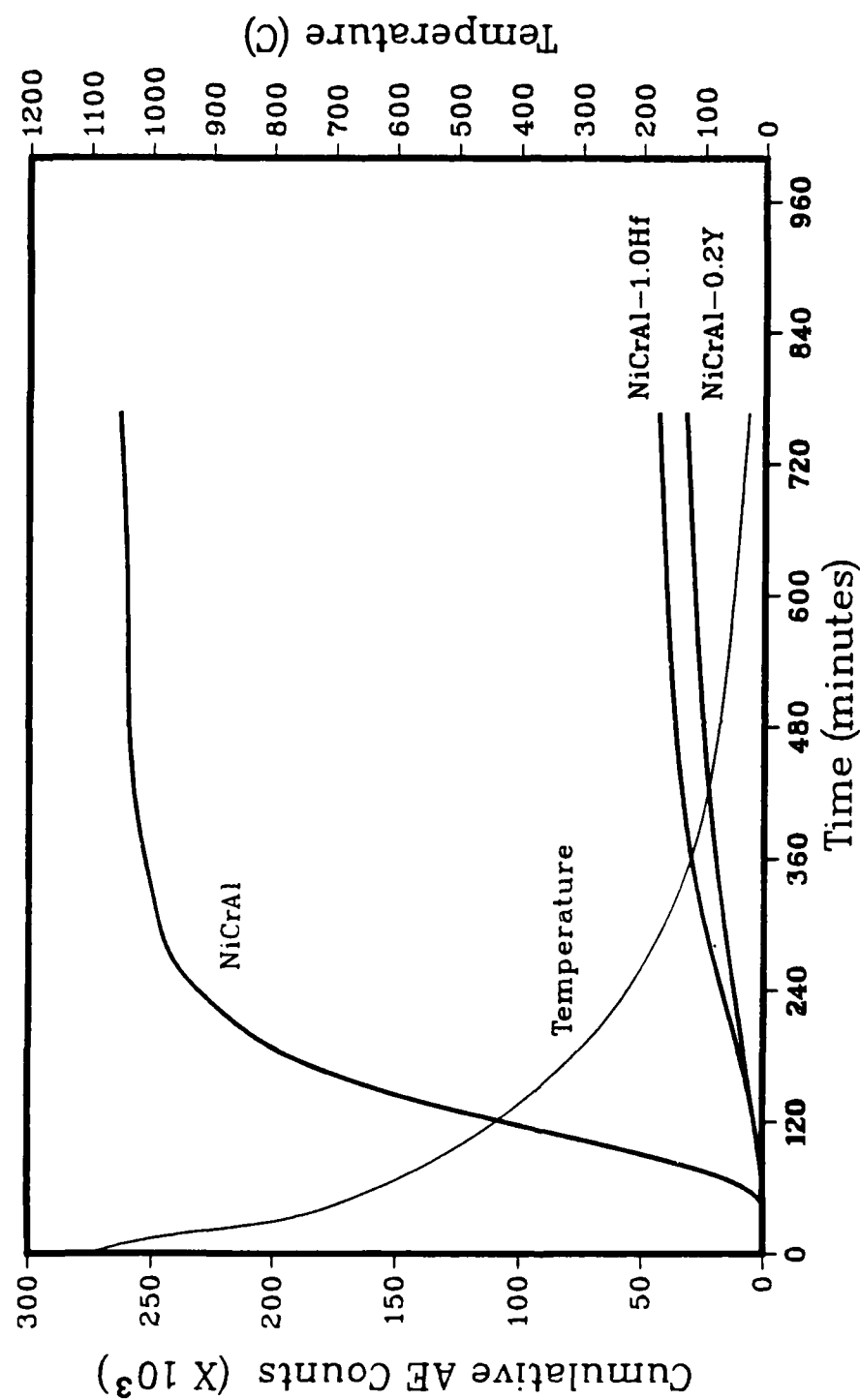


Figure 22: Cumulative AE counts during the cooling of NiCrAl, NiCrAl-0.2Y, and NiCrAl-1.0Hf specimens oxidized for 24 hours at 1100°C.

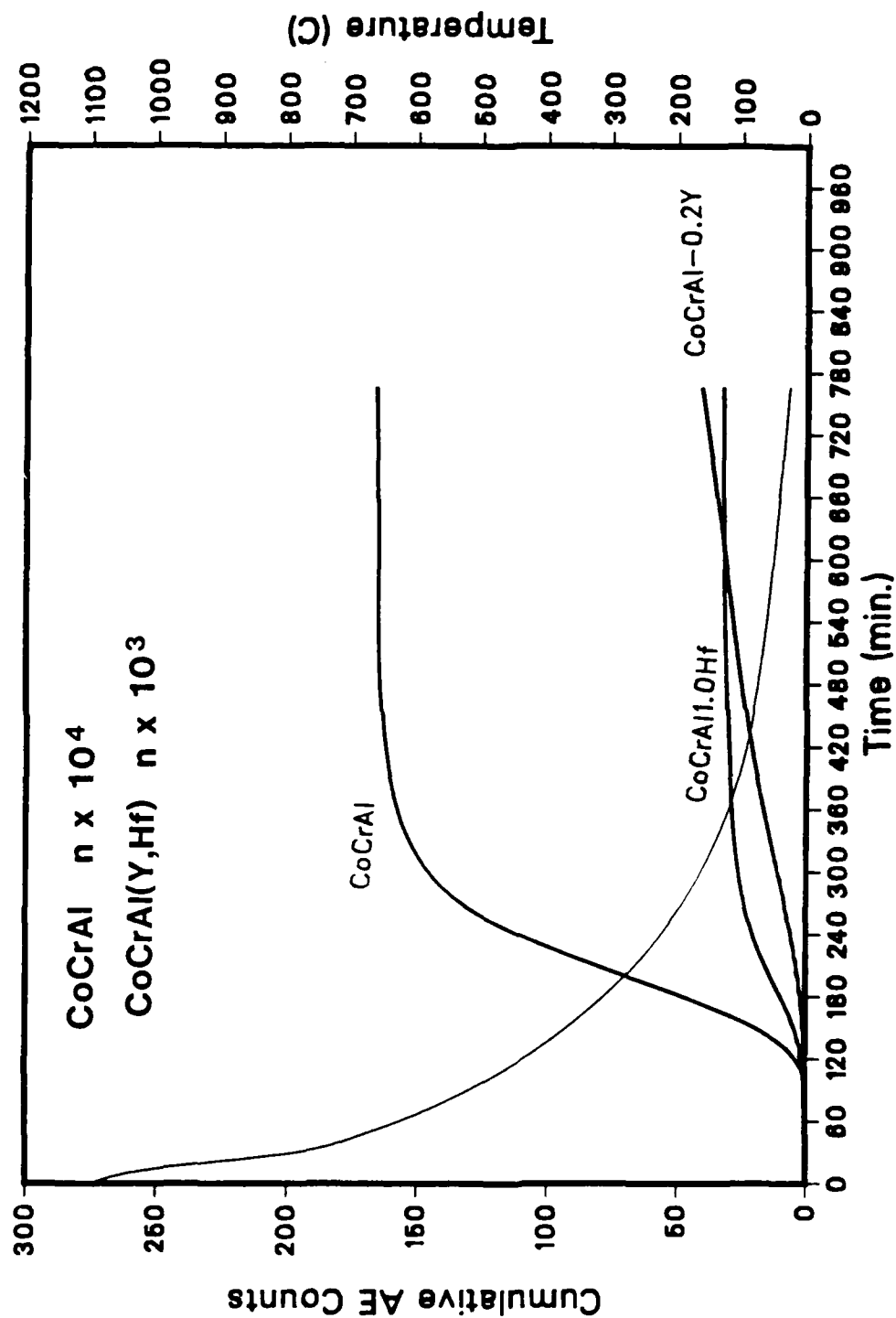
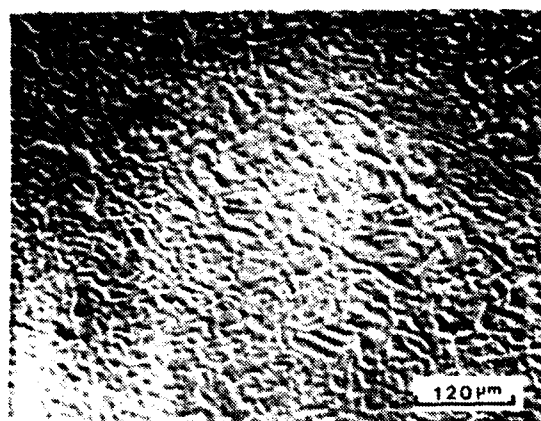
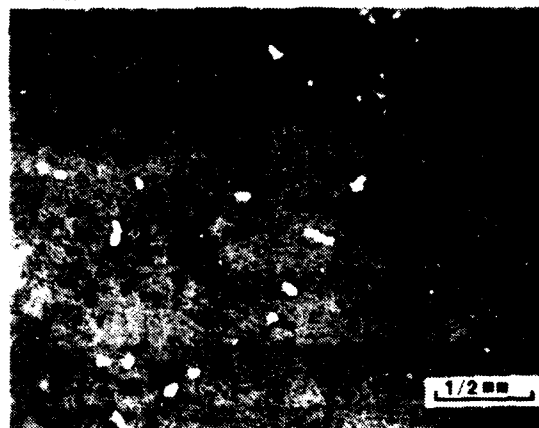


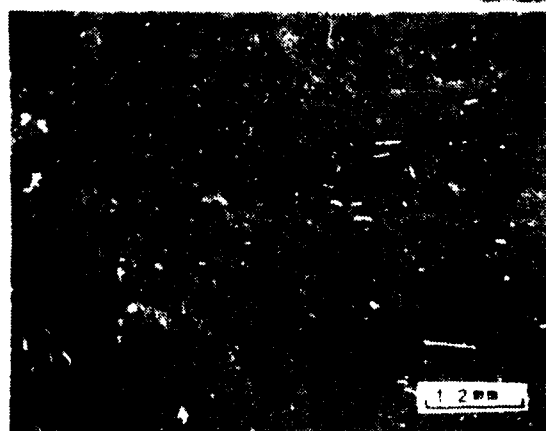
Figure 23: Cumulative AE counts during the cooling of CoCrAl, CoCrAl-0.2Y, and CoCrAl-1.0Hf specimens oxidized for 24 hours at 1100°C.



(a)

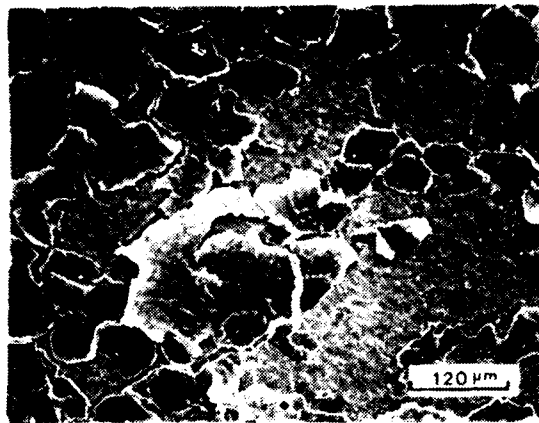


(b)

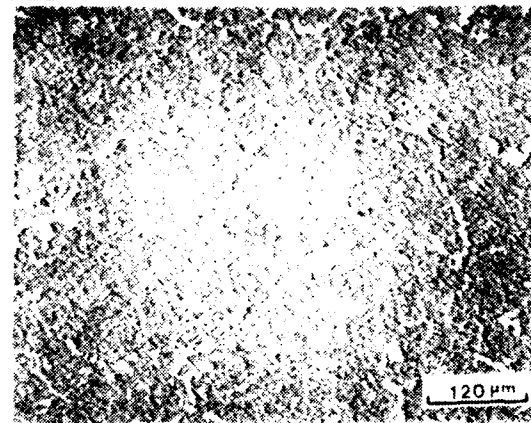


(c)

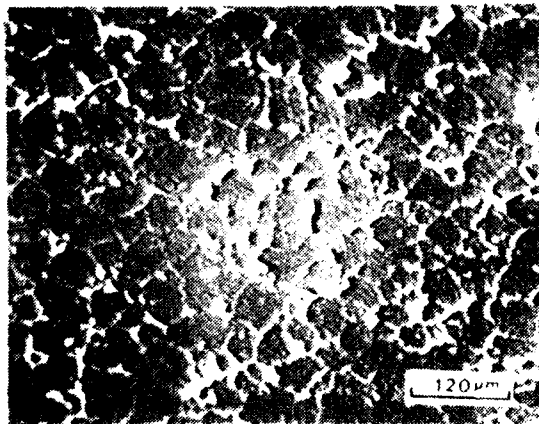
Figure 24: SEM micrographs of the surfaces of NiCrAl, NiCrAl-0.2Y, and NiCrAl-1.0Hf specimens oxidized for 24 hrs. at 1100°C, in the short term AE experiments.



(a)



(b)



(c)

Figure 25: SEM micrographs of the surfaces of CoCrAl, CoCrAl-0.2Y and CoCrAl-1.0Hf specimens oxidized for 24 hrs. at 1100°C, in the short term AE experiments.

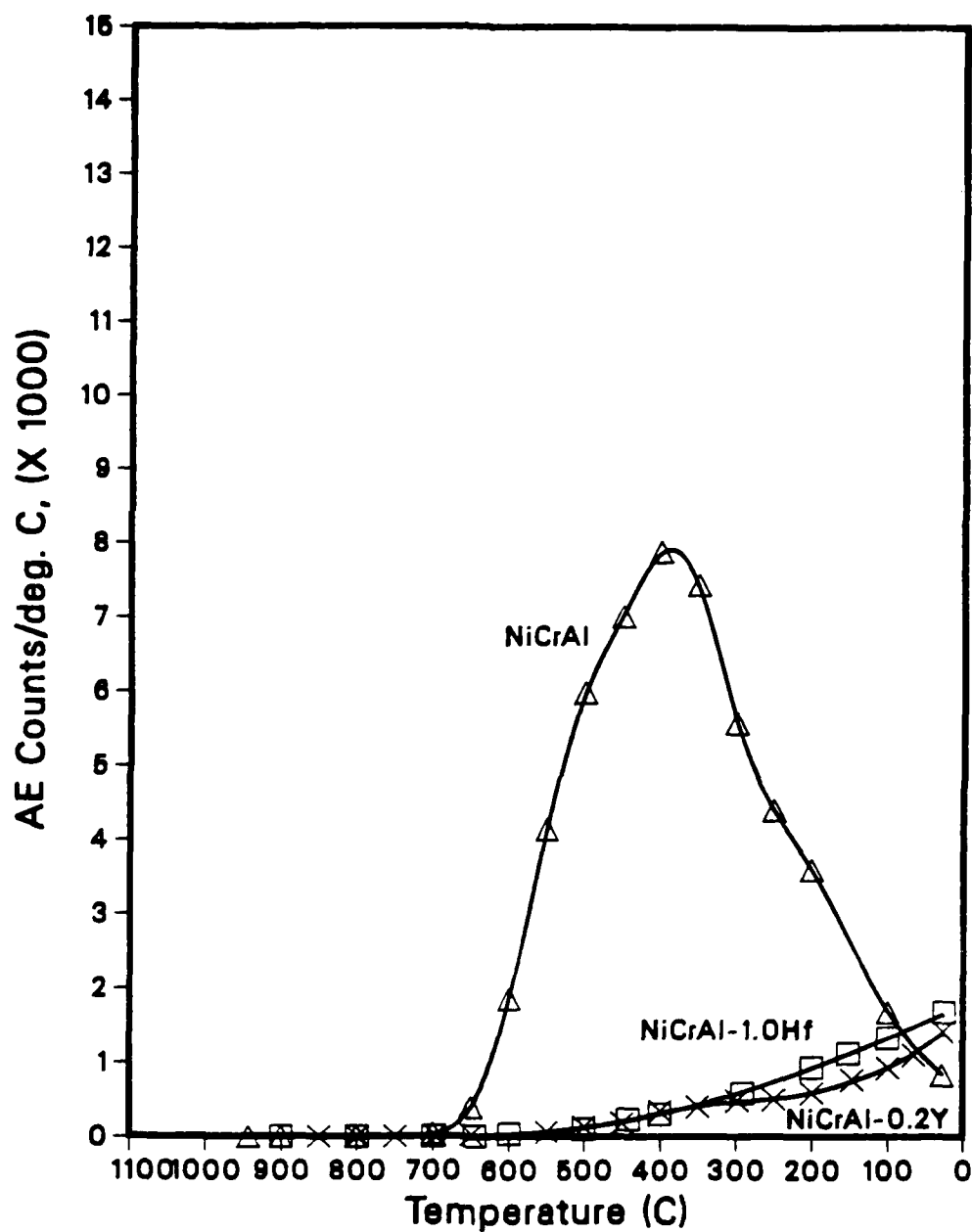


Figure 26: Acoustic emission count rate during cooling of NiCrAl, NiCrAl-0.2Y, and NiCrAl-1.0Hf specimens as a function of the temperature of the specimens. Prior to the cooling the specimens were oxidized isothermally at 1100°C.

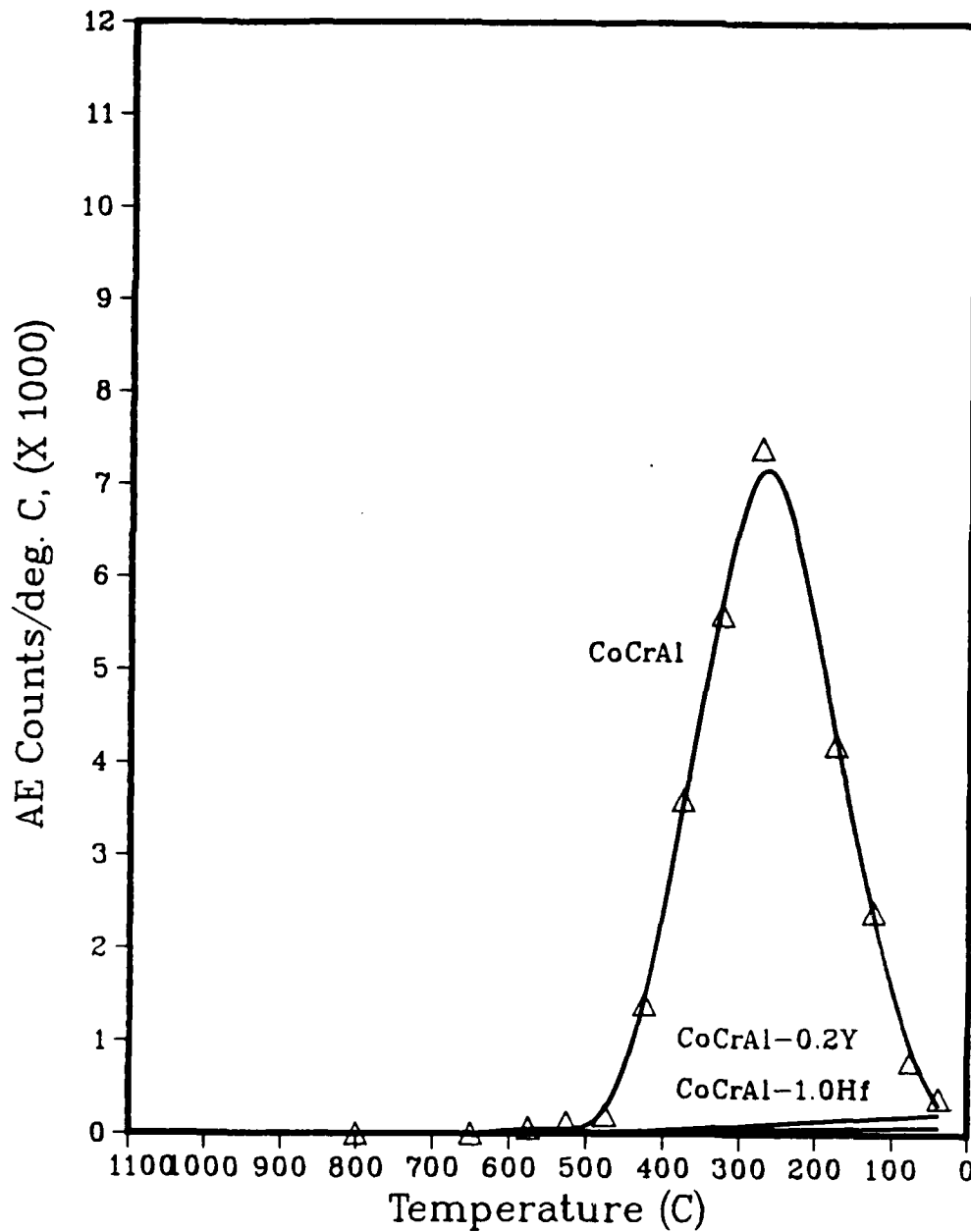


Figure 27: Acoustic emission count rate during cooling of CoCrAl, CoCrAl-0.2Y and CoCrAl-1.0Hf specimens as a function of the temperature of the specimens. Prior to the cooling the specimens were oxidized isothermally at 1100°C.



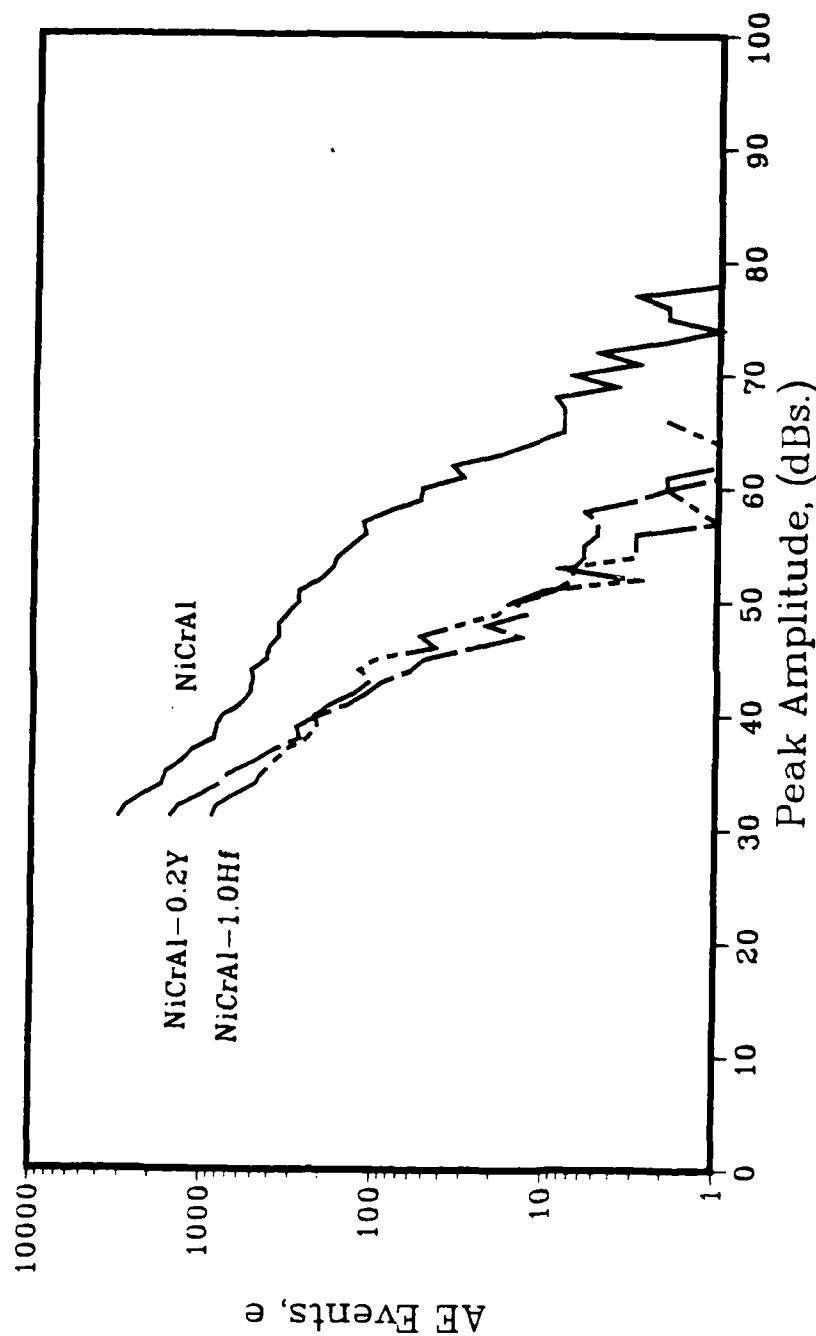


Figure 28: Frequency distribution of AE events with respect to their peak amplitudes during the cooling of NiCrAl, NiCrAl-0.2Y and NiCrAl-1.0Hf specimens after 24 hours of oxidation at 1100°C.

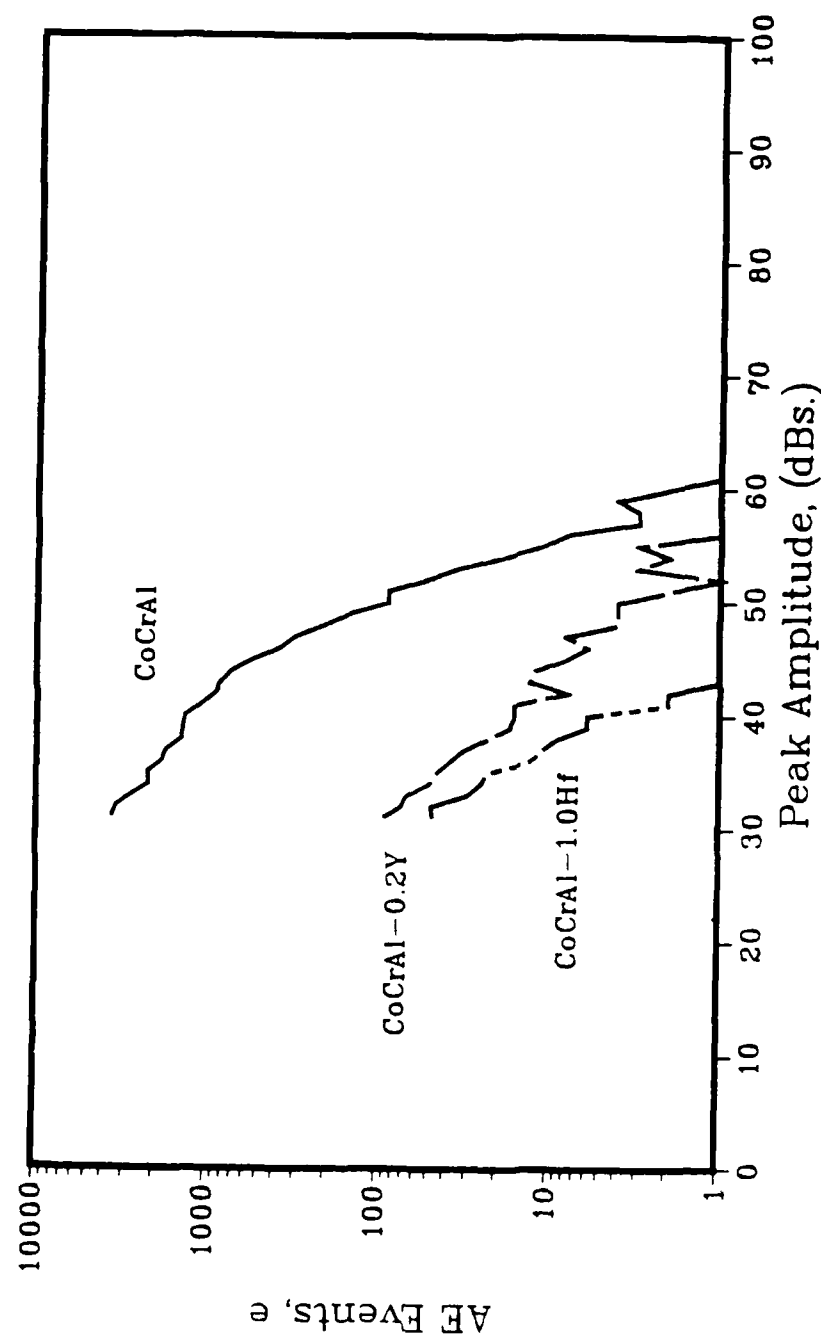


Figure 29: Frequency distribution of AE events with respect to their peak amplitudes during the cooling of CoCrAl, CoCrAl-0.2Y and CoCrAl-1.0Hf specimens after 24 hours of oxidation at 1100°C.

AD-A170 192

ADVANCED HIGH TEMPERATURE COATING SYSTEMS BEYOND  
CURRENT STATE OF THE ART. (U) PITTSBURGH UNIV PA DEPT  
OF MATERIALS SCIENCE AND ENGINEERING. A ASHARY ET AL.

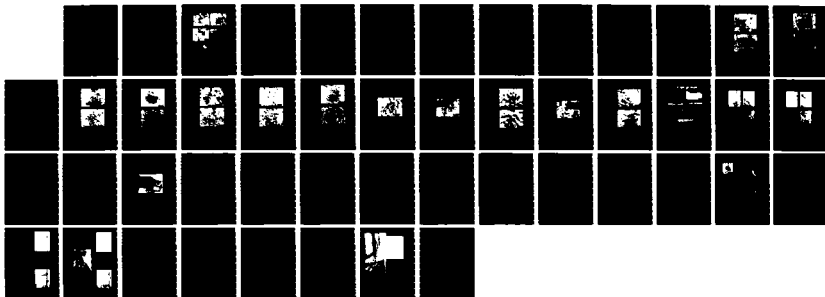
2/2

UNCLASSIFIED

15 APR 86 AFOSR-TR-86-0481 AFOSR-80-0089

F/G 11/3

NL





1.0



2.8



2.5



3.15



2.2



1.1



3.5



2.0



4.0



1.8



1.25



1.4



1.6

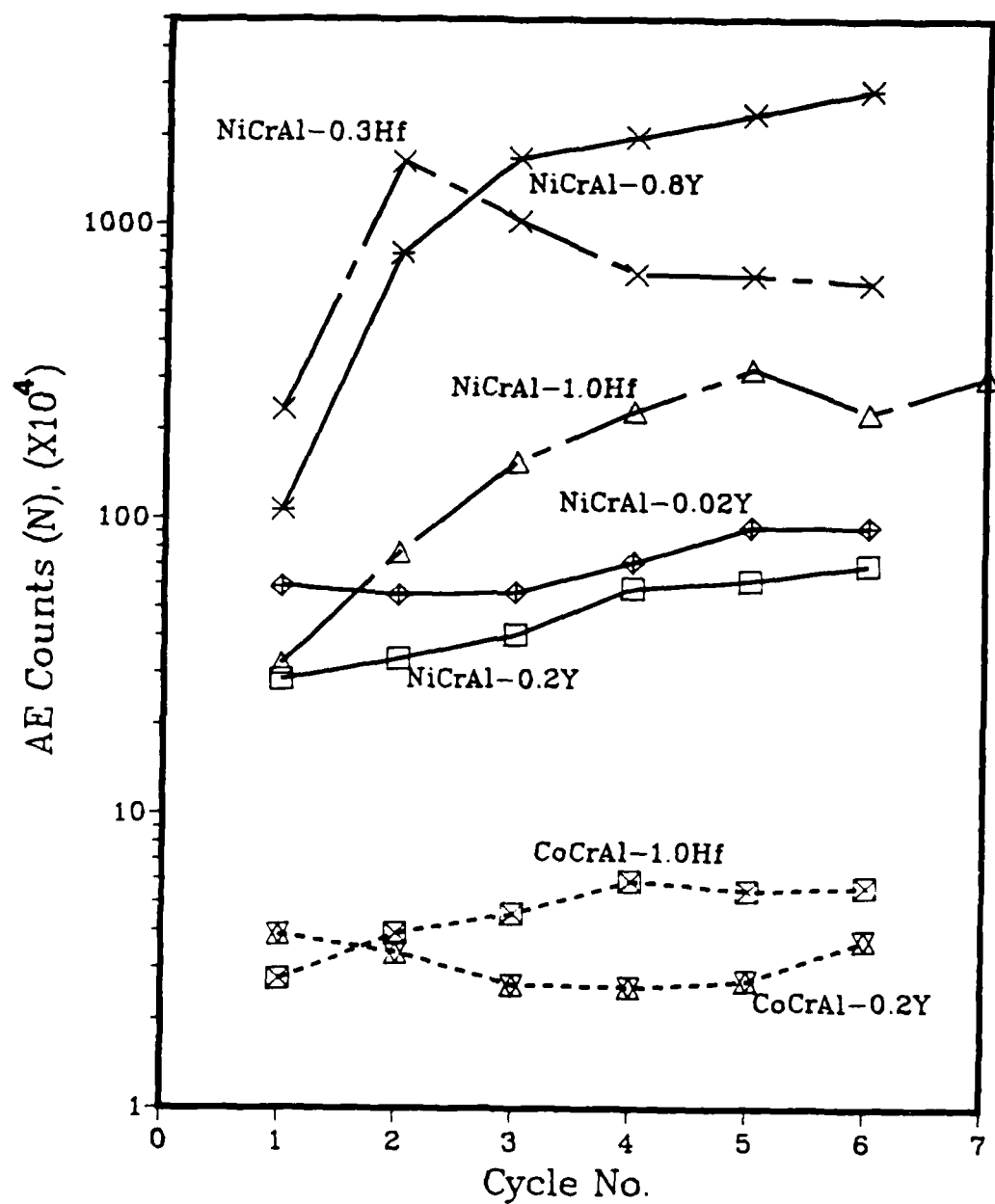
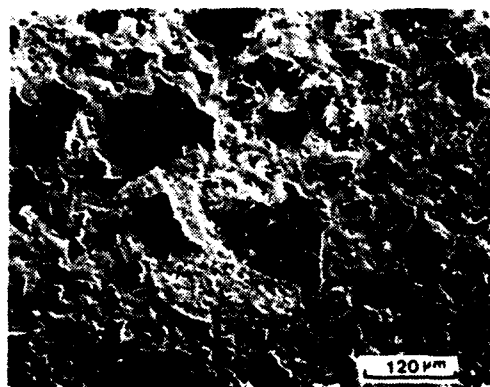
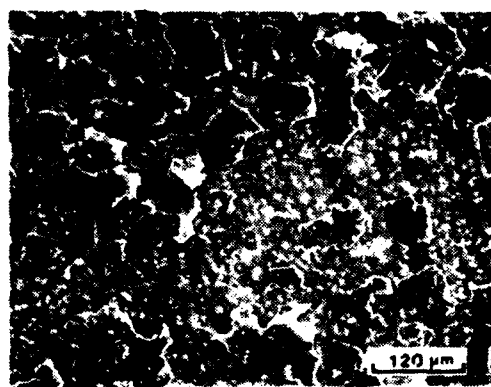


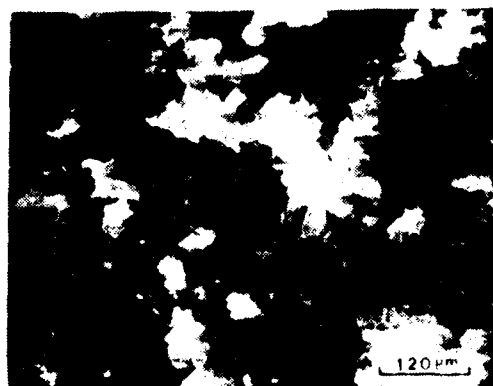
Figure 30: Cumulative AE counts generated during each cooling period during the cyclic oxidation of the specimens at 1100°C. Each cycle consisted of 24 hours isothermal oxidation followed by half an hour cooling.



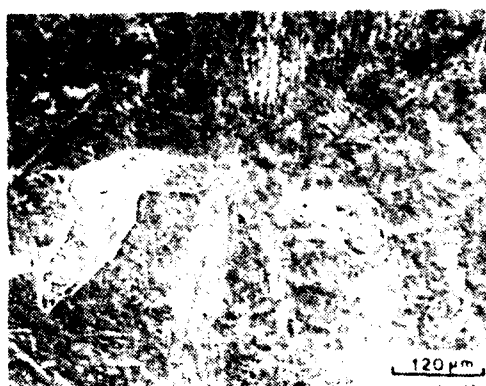
(a) NiCrAl-0.8Y



(b) NiCrAl-0.3Hf



(c) NiCrAl-1.0Hf



(d) NiCrAl-0.2Y



(e) CoCrAl-0.2Y

Figure 31: SEM micrographs showing the surface of some of the specimens after the cyclic oxidation in the AF experiment.

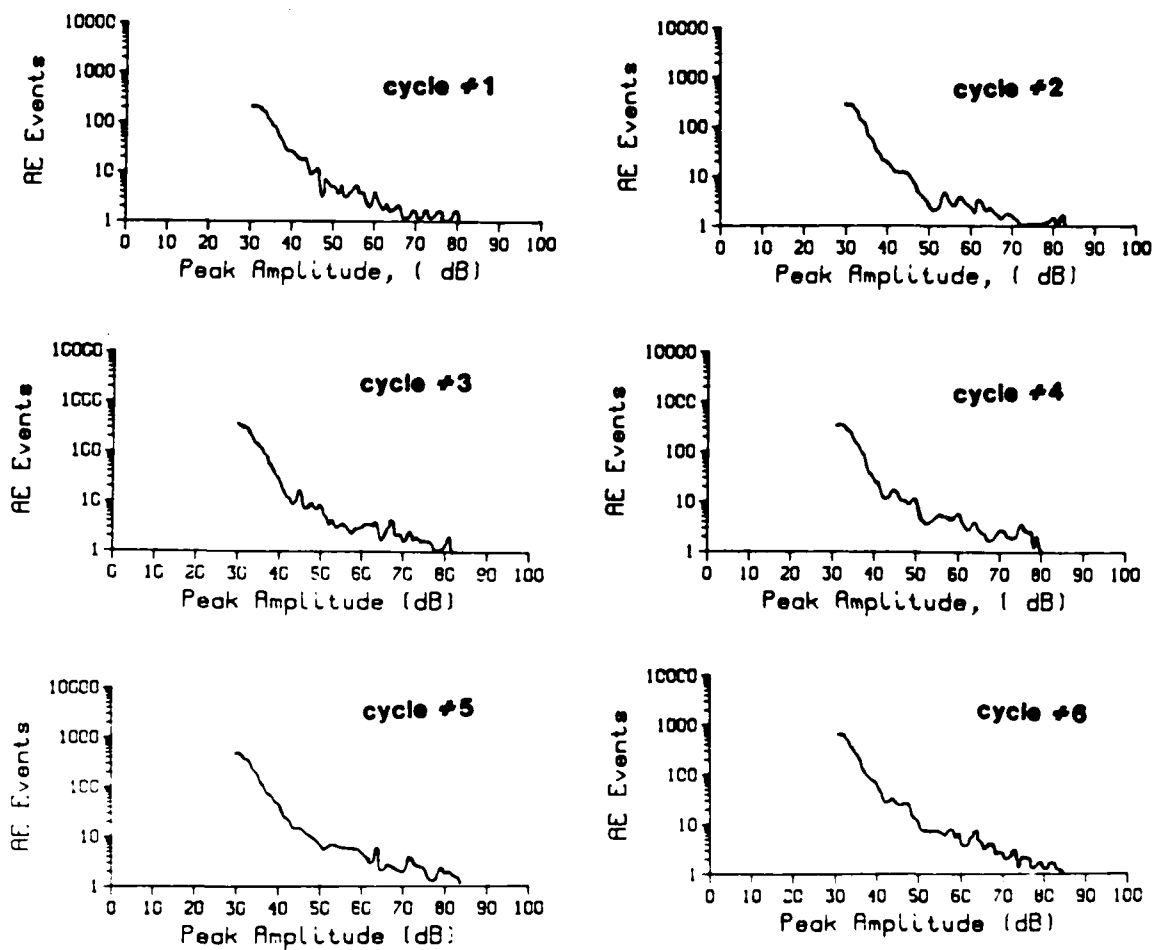
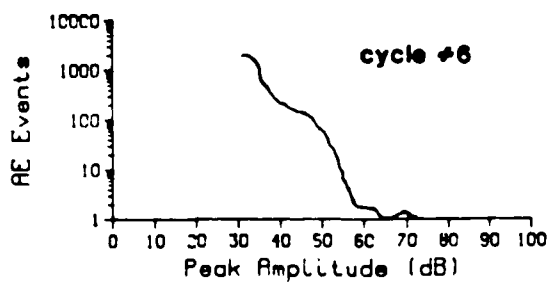
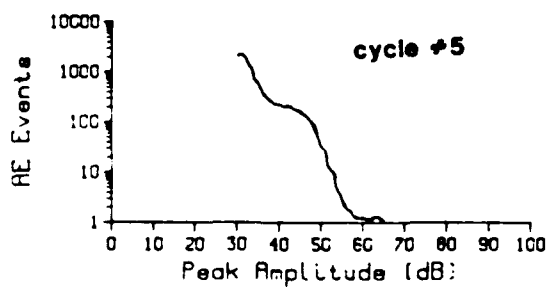
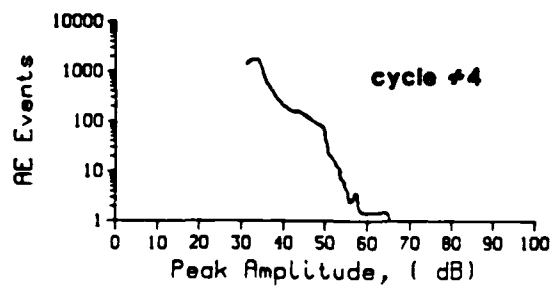
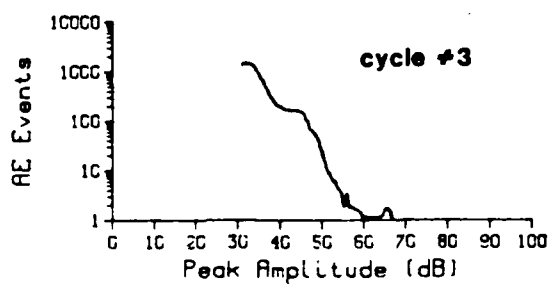
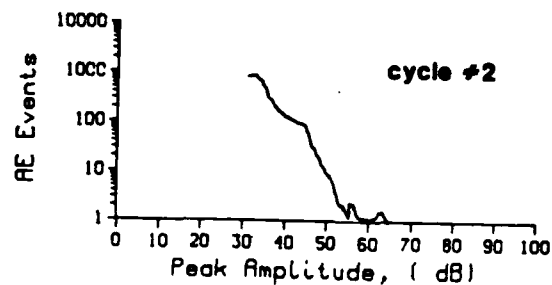
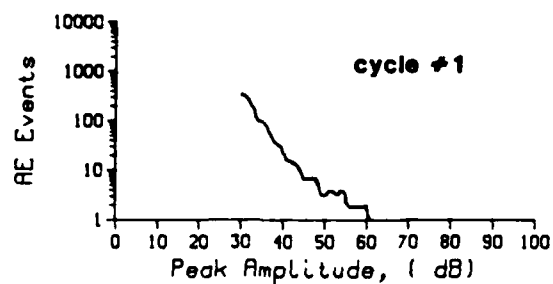


Figure 32: Peak amplitude distributions of AE events obtained during the cooling of NiCrAl-0.2Y specimen undergone cyclic oxidation at 1100°C.



**Figure 33:** Peak amplitude distributions of AE events obtained during the cooling of NiCrAl-1.0Hf specimen undergone cyclic oxidation at 1100°C.



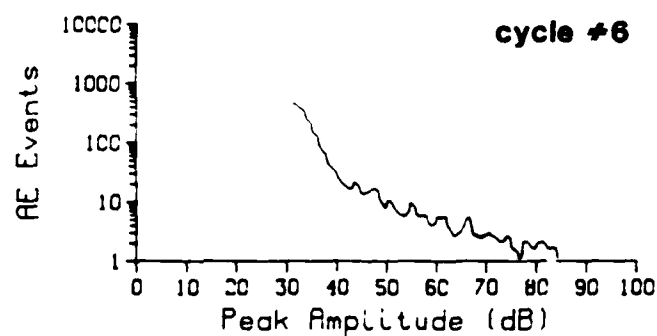
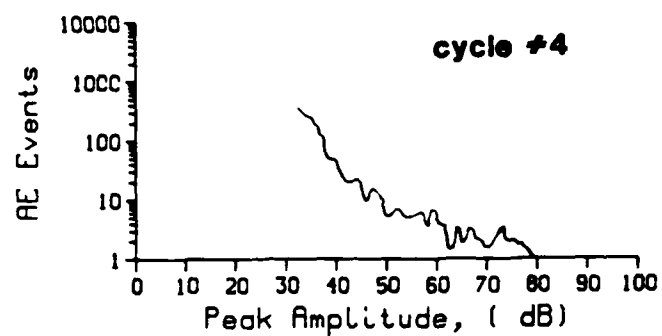
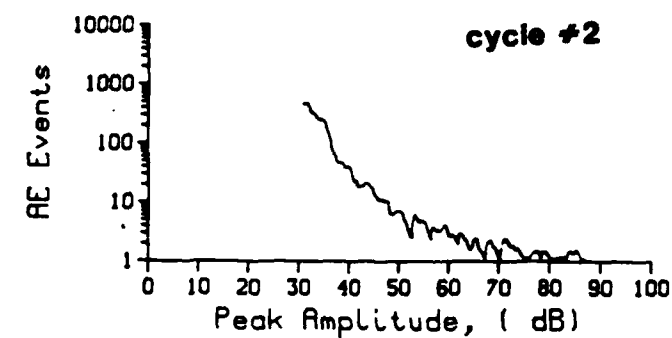
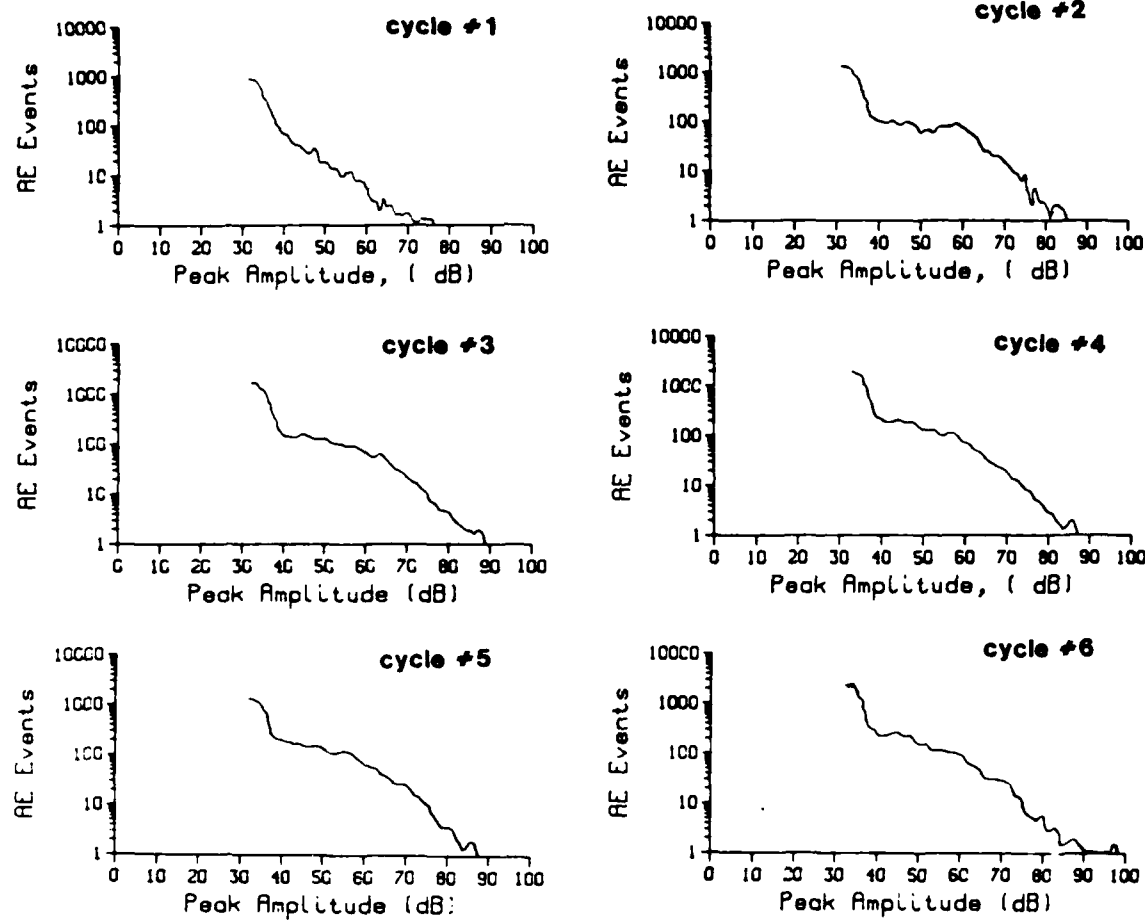


Figure 34: Peak amplitude distributions of AE events obtained during the cooling of NiCrAl-0.02Y specimen undergone cyclic oxidation at 1100°C.



**Figure 35:** Peak amplitude distributions of AE events obtained during the cooling of NiCrAl-0.8Y specimen undergone cyclic oxidation at 1100°C.

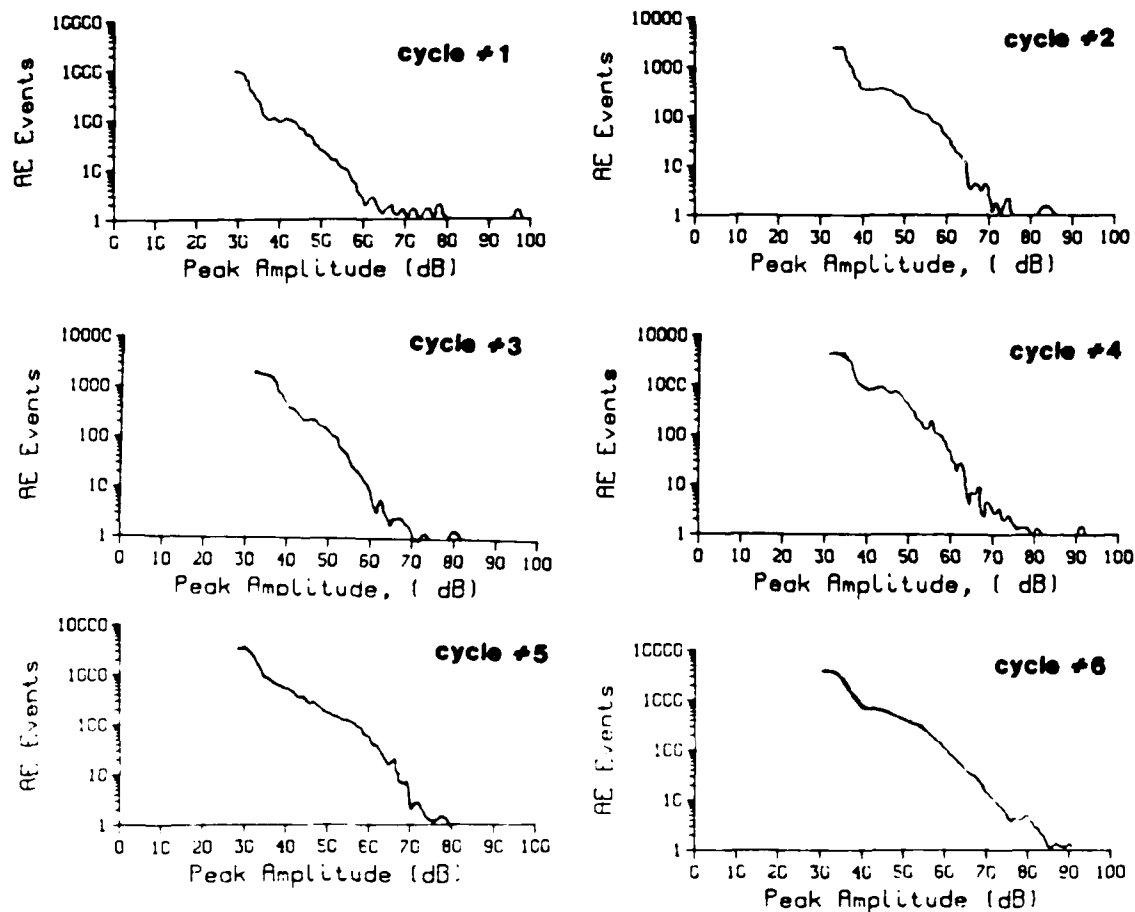


Figure 36: Peak amplitude distributions of AE events obtained during the cooling of NiCrAl-0.3Hf specimens undergone cyclic oxidation at 1100°C.

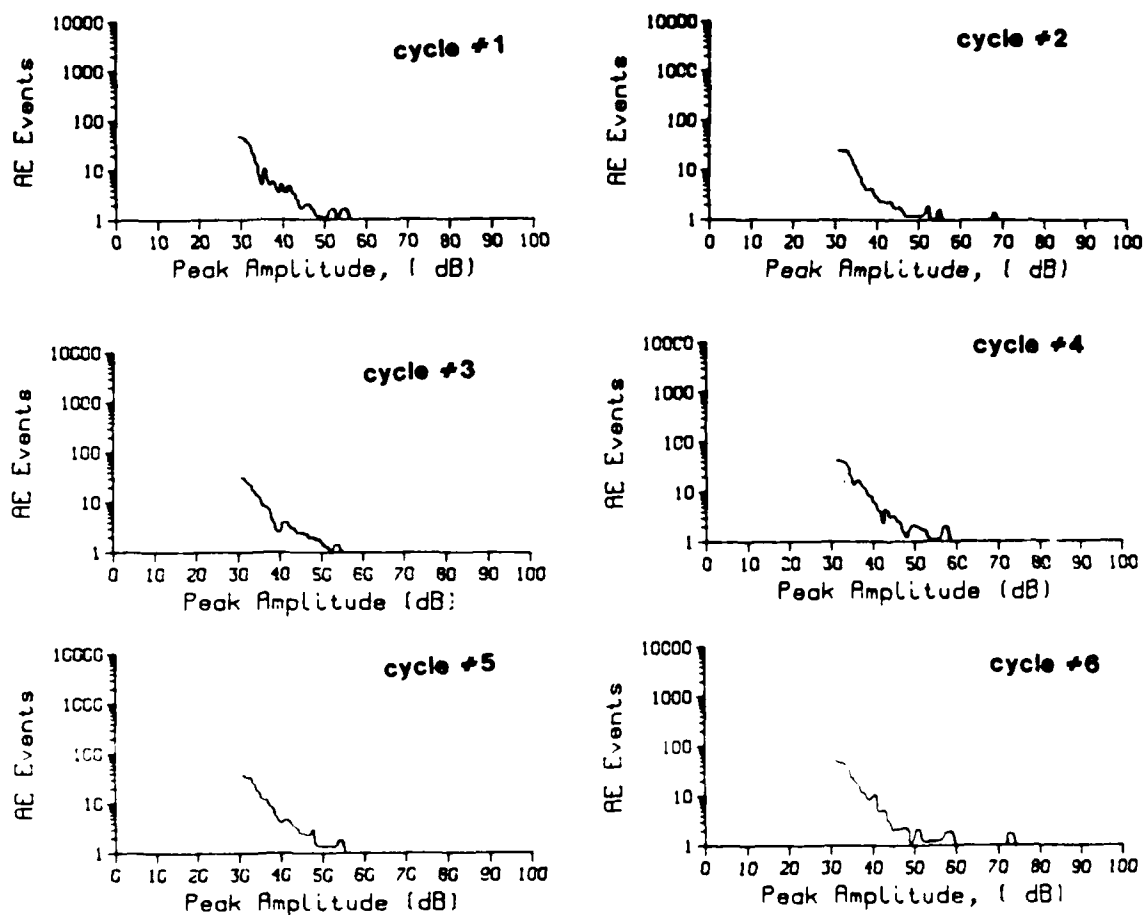


Figure 37: Peak amplitude distributions of AE events obtained during the cooling of CoCrAl-0.2Y specimen undergone cyclic oxidation at 1100°C.

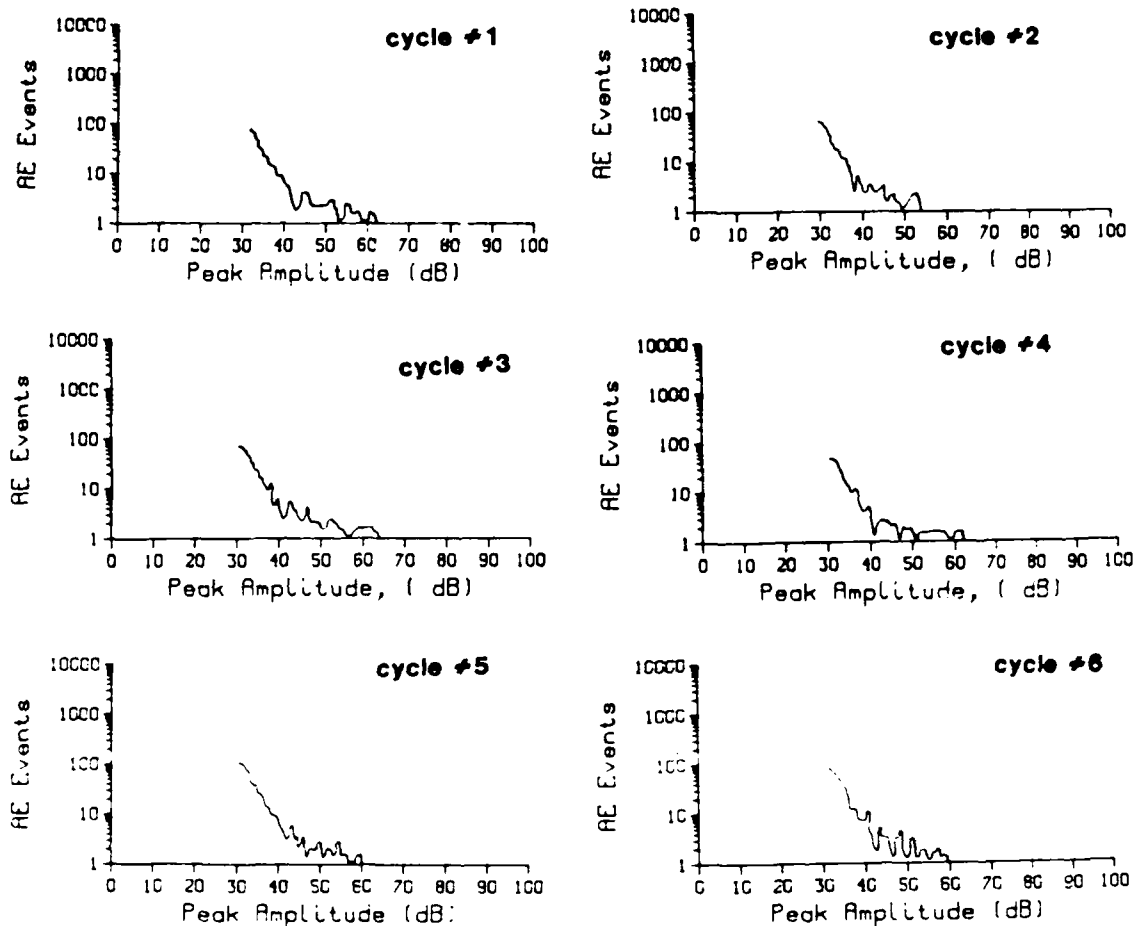


Figure 38: Peak amplitude distributions of AE events obtained during the cooling of CoCrAl-1.0Hf specimen undergone cyclic oxidation at 1100°C.

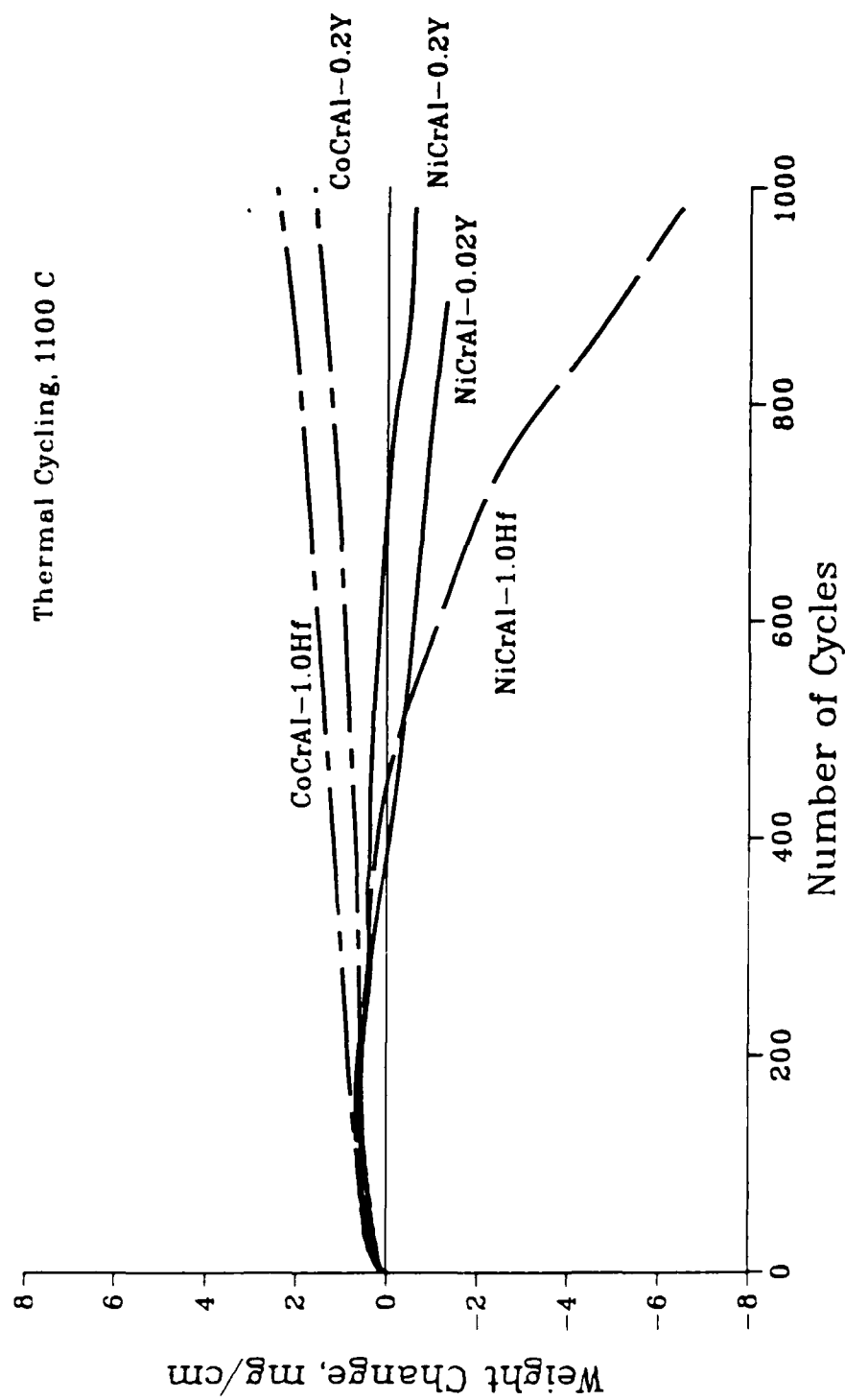
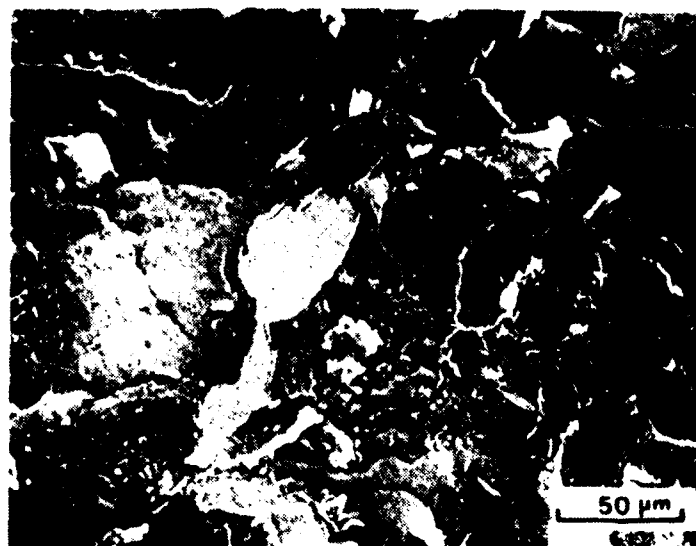


Figure 39: Long term cyclic oxidation weight change data for some of the active element containing alloys.

(a)



(b)

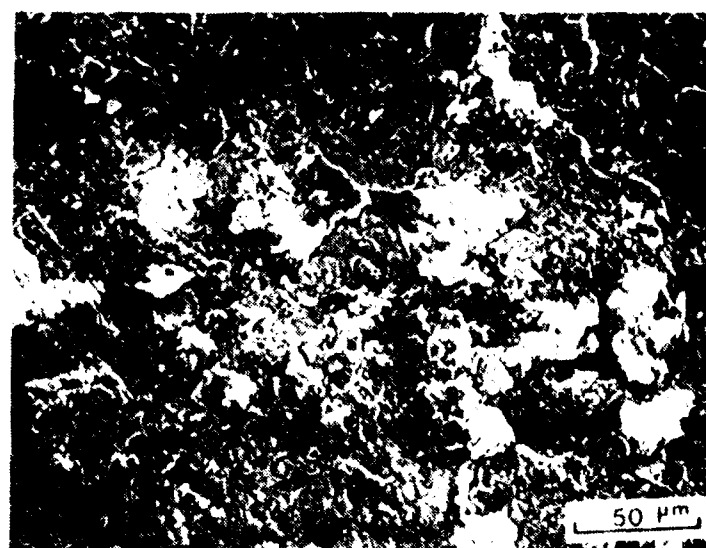
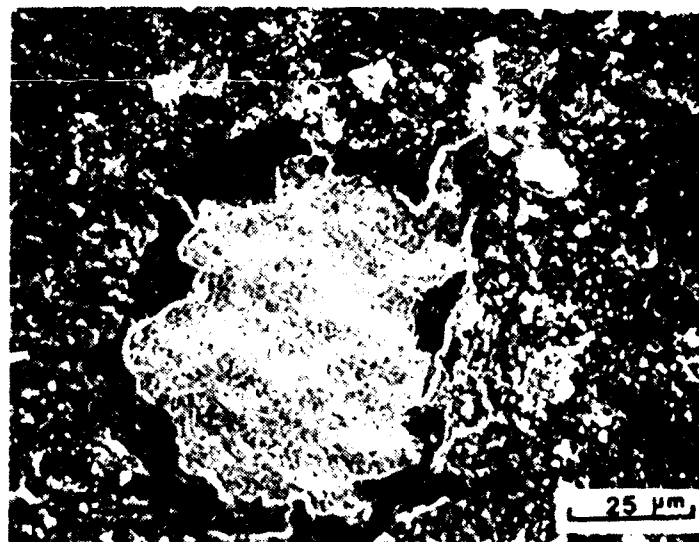


Figure 40: SEM micrographs showing the surface of the specimens undergone 1000 hrs. thermal cycling. (a) NiCrAl-0.2Y and (b) NiCrAl-1.0Y.

(a)



(b)

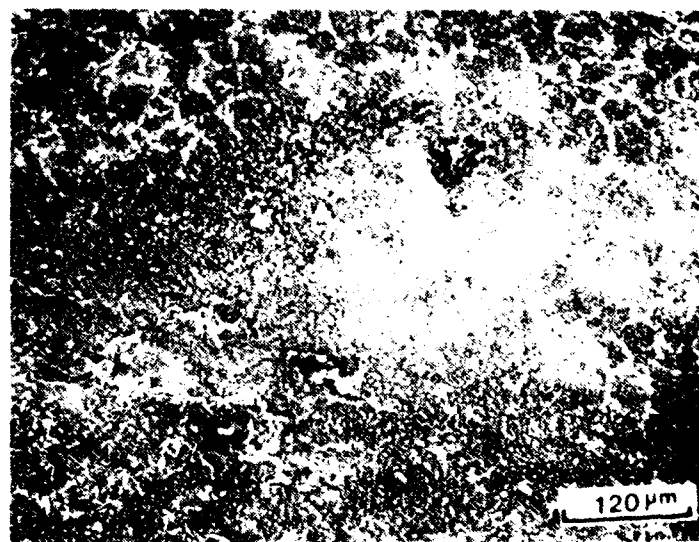


Figure 41: SEM micrographs showing the surfaces of the specimens undergone 100 hrs. thermal cycling: (a) Cu-1Al-0.2Y and (b) Cu-1Al-1.3Hf.



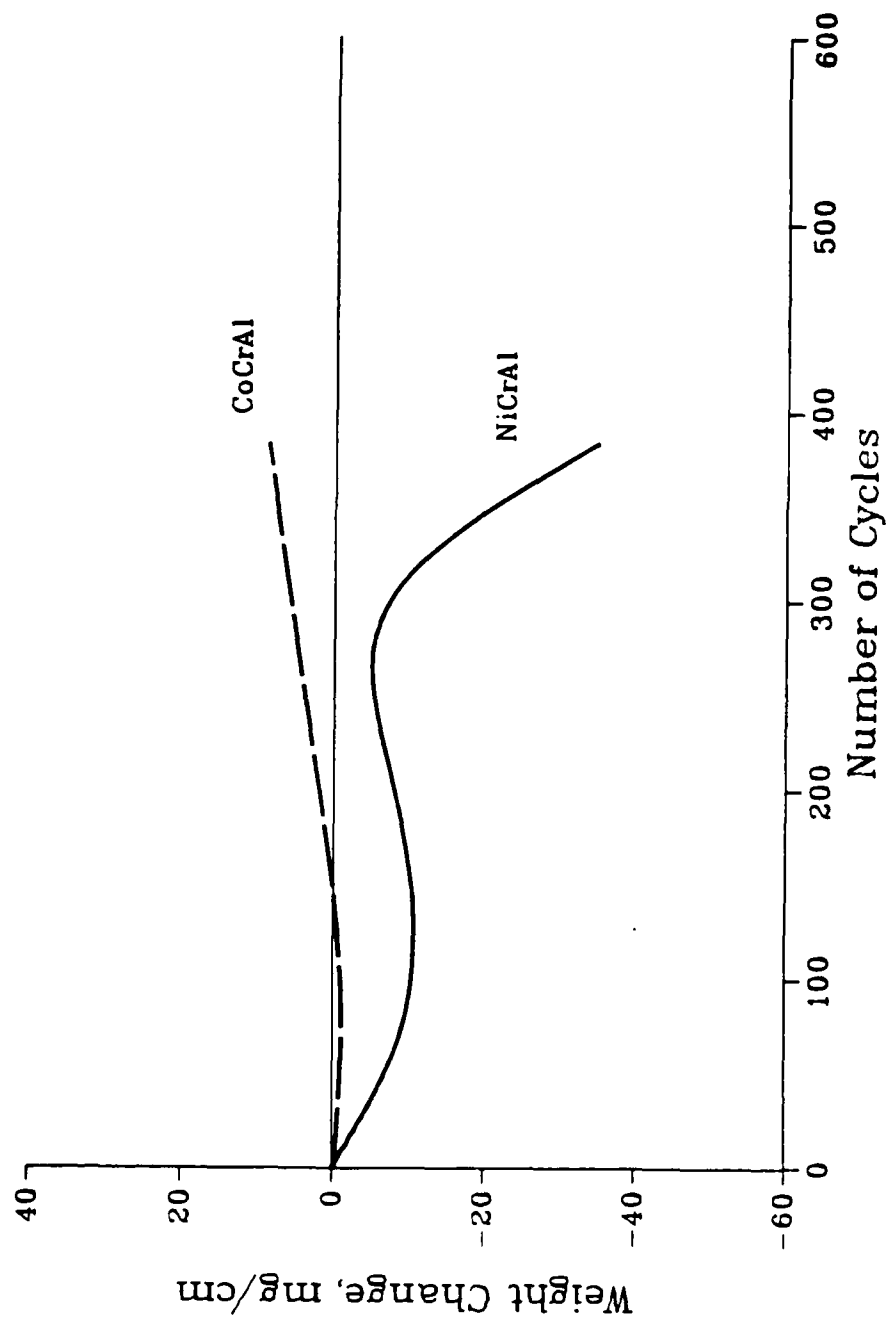
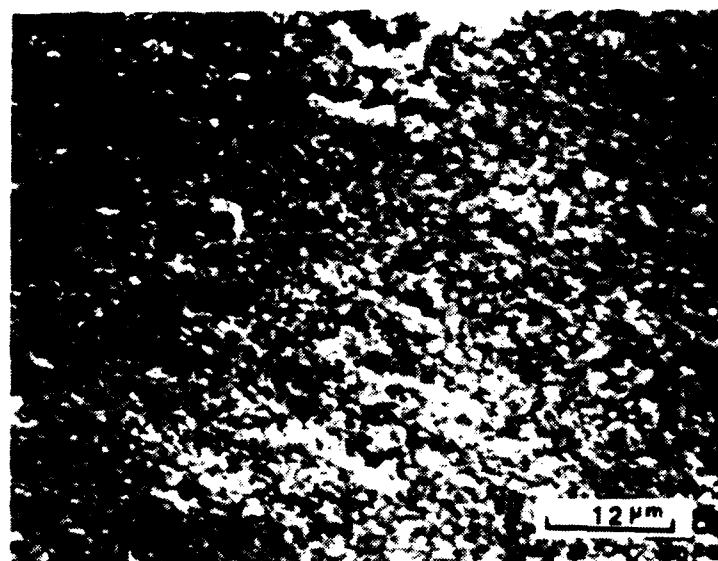


Figure 42: Long term cyclic oxidation weight change data for the undoped alloys.

(a)



(b)

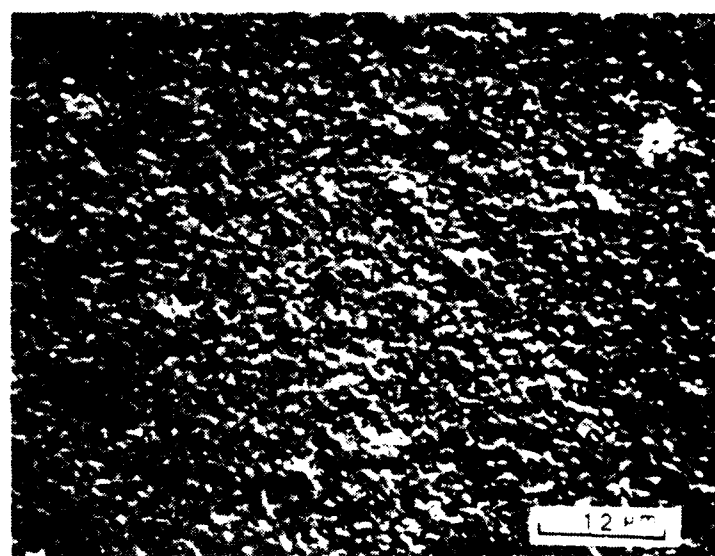
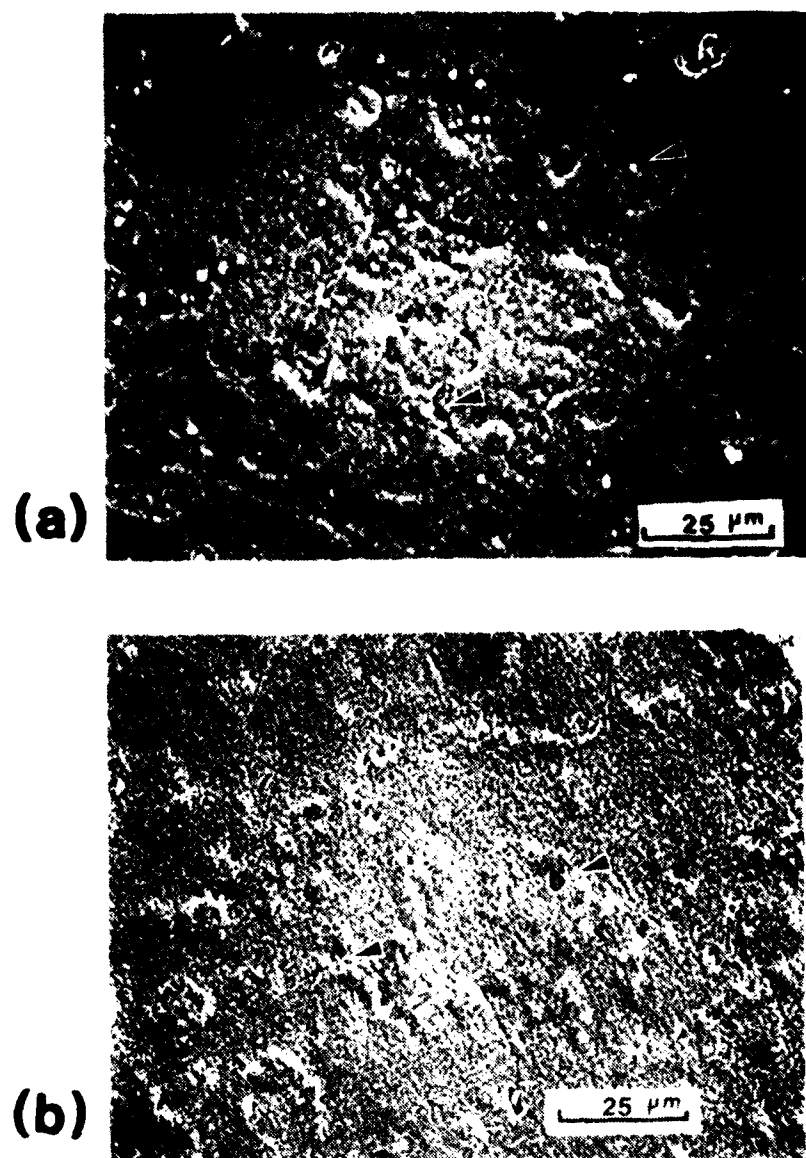


Figure 43: Surfaces exposed as a result of the mechanical stripping of the  $\text{Al}_2\text{O}_3$  scale from the NiCrAl-0.02Y specimen, oxidized for 48 hours at 1100°C, (a) underside of  $\text{Al}_2\text{O}_3$  scale, (b) substrate.



**Figure 44:** Surfaces exposed as a result of the mechanical stripping of the  $\text{Al}_2\text{O}_3$  scale from the Ni-4Al-0.2Y specimen, oxidized for 48 hours at 1100°C. Arrows indicating the yttrium rich particles, (a) underside of  $\text{Al}_2\text{O}_3$  scale, (b) substrate.

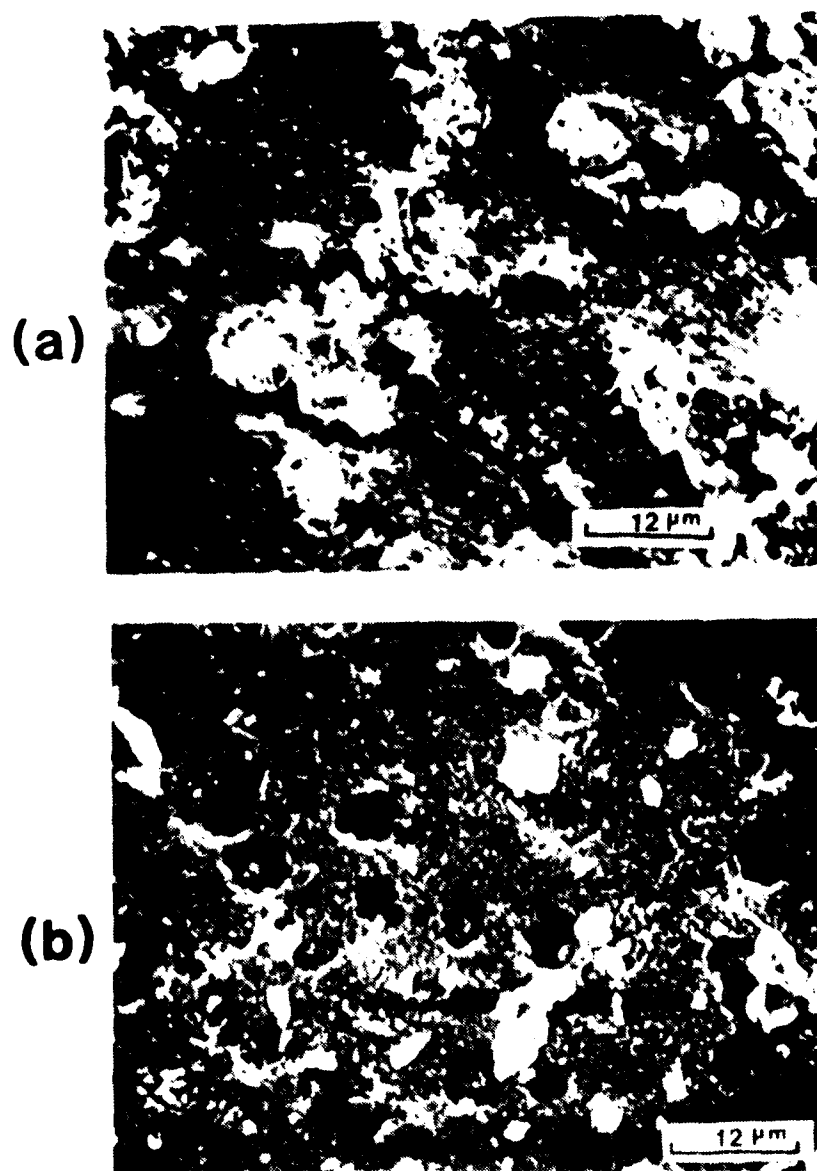


Figure 45: Surfaces exposed as a result of the mechanical stripping of the  $\text{Al}_2\text{O}_3$  scale from the NiCrAl-0.8Y specimen, oxidized for 48 hours at 1100°C, (a) underside of  $\text{Al}_2\text{O}_3$  scale, (b) substrate.

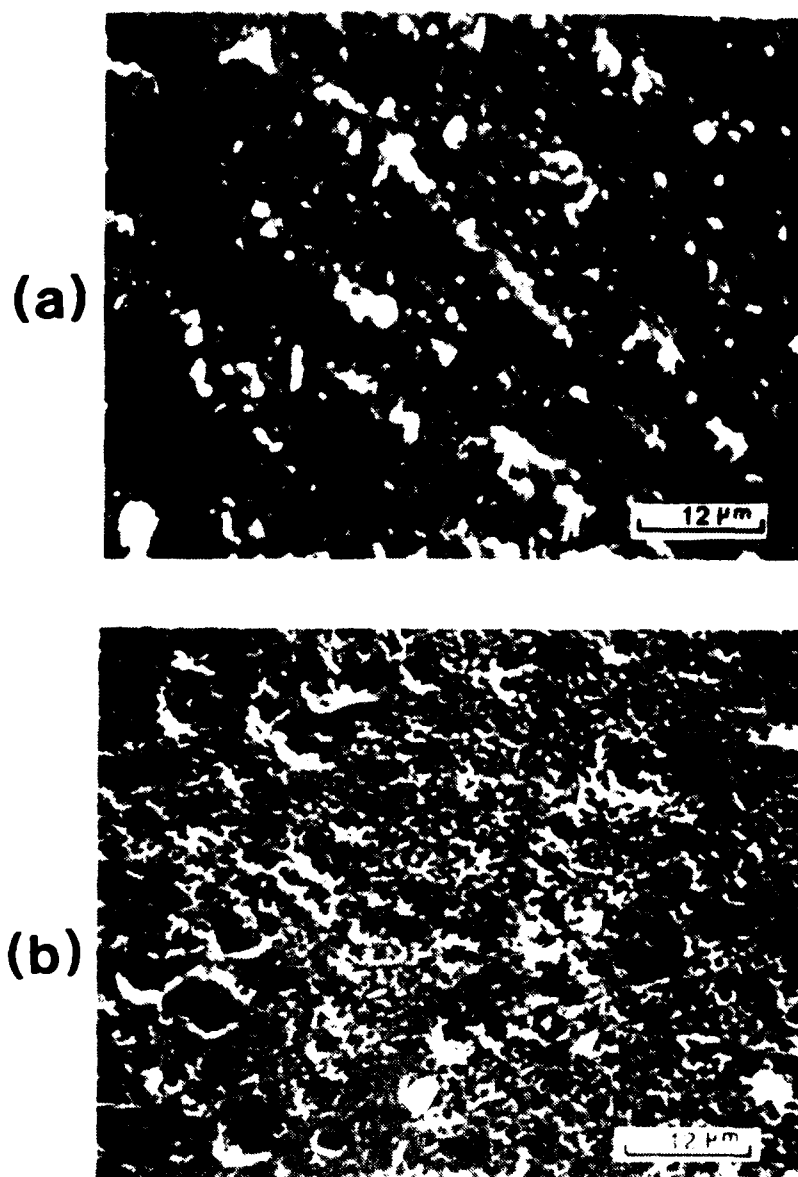
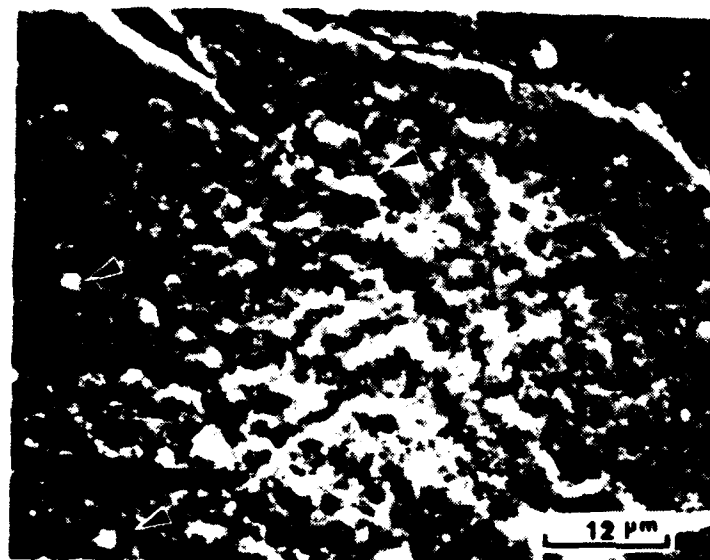


Figure 46: Surfaces exposed as a result of the mechanical stripping of the  $\text{Al}_2\text{O}_3$  scale from the Ni-7Al-0.3Hf specimen, oxidized for 48 hours at 1100°C, (a) underside of  $\text{Al}_2\text{O}_3$  scale, (b) substrate.

(a)



(b)

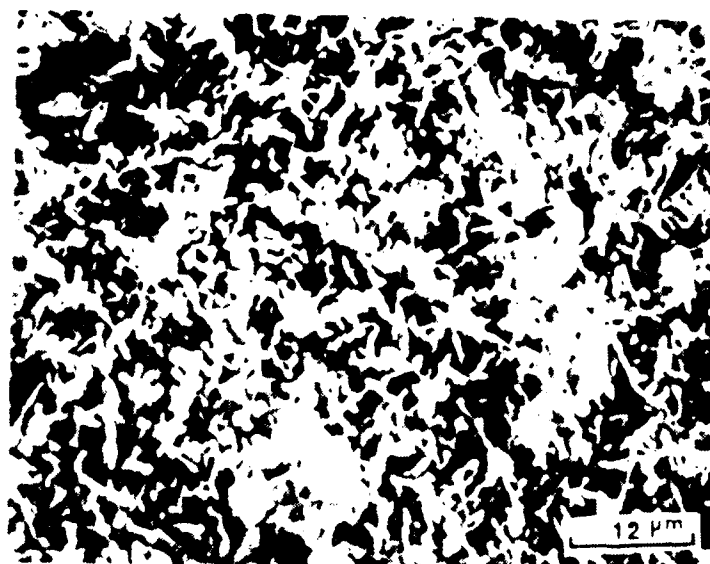


Figure 47: Underside of the  $\text{Al}_2\text{O}_3$  scales obtained by the chemical dissolution of the substrates (oxidized for 48 hours at  $1100^\circ\text{C}$ ), (a) CoCrAl-0.2Y arrows indicating the yttrium rich particles, (b) CoCrAl-1.0Hf.

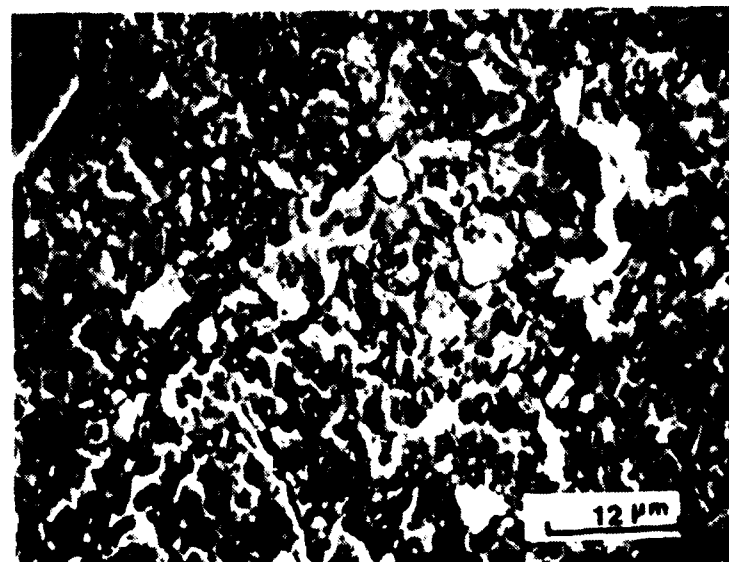


Figure 48: Spalled area on the surface of NiCrAl-1.0Hf specimen oxidized for 48 hours at 1100°C.

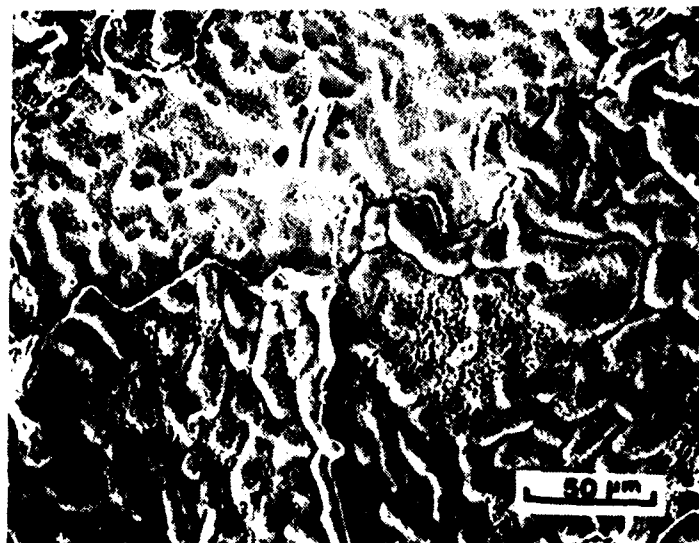
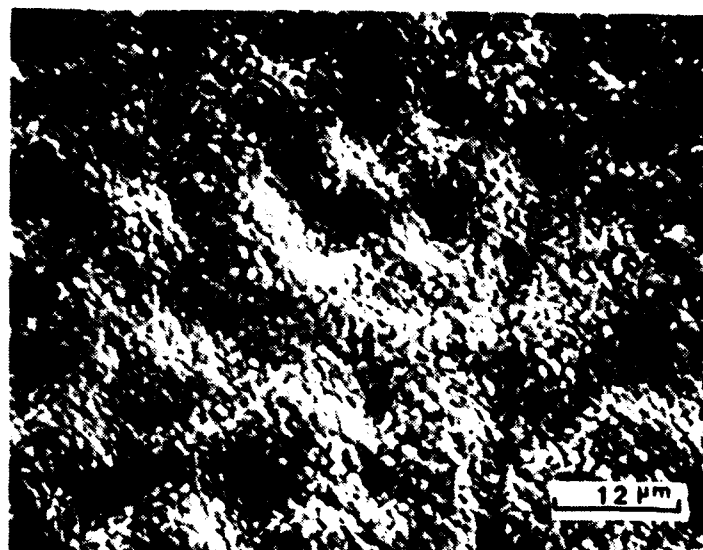


Figure 49: SEM micrograph showing the surface of NiCrAl specimen oxidized for one week at 1100°C.



(a)



(b)

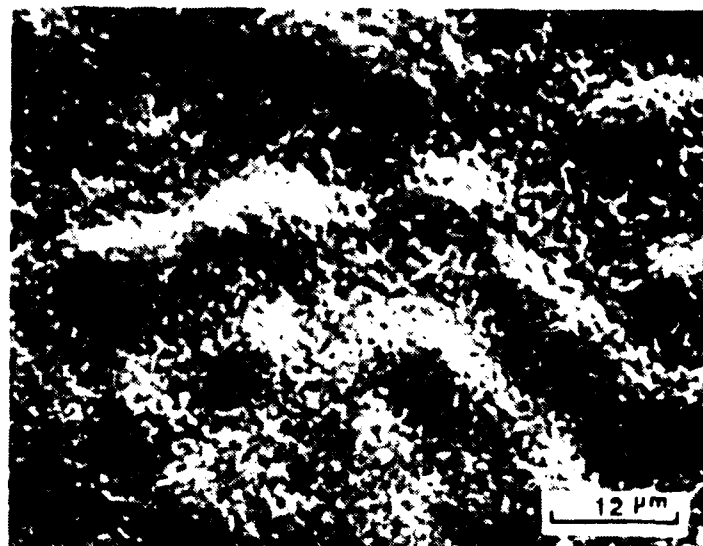


Figure 50: (a) The underside of the Al<sub>2</sub>O<sub>3</sub> scale spalled from the undoped NiCrAl specimen after 24 hours of oxidation at 1100°C, (b) the exposed substrate surface.

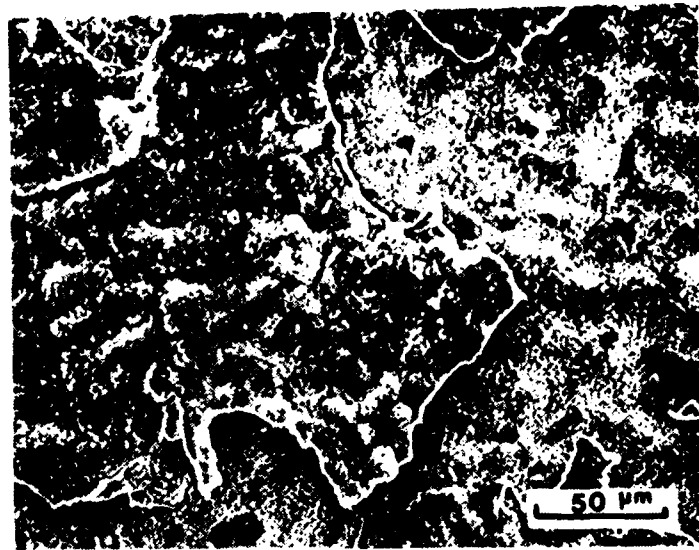
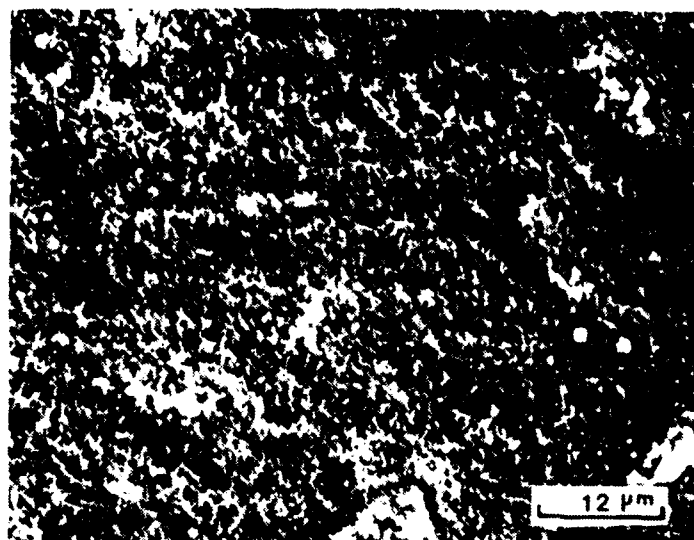
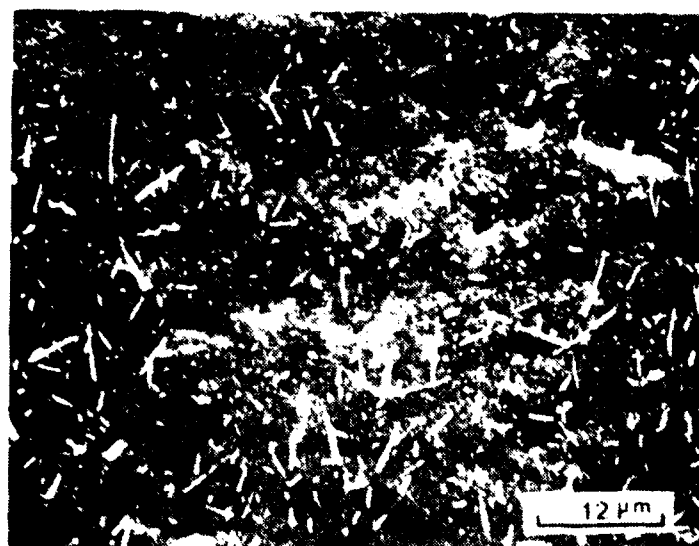


Figure 51: SEM micrograph showing the surface of CoCrAl specimen oxidized for one week at 1100°C.

(a)



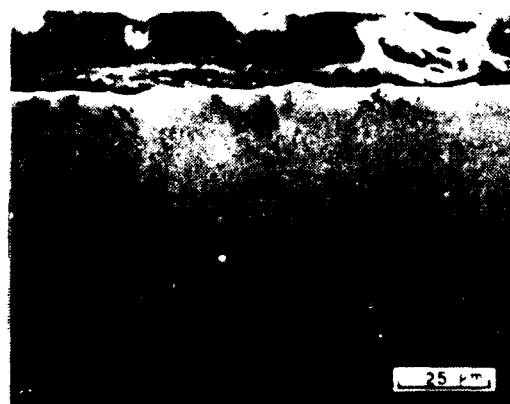
(b)



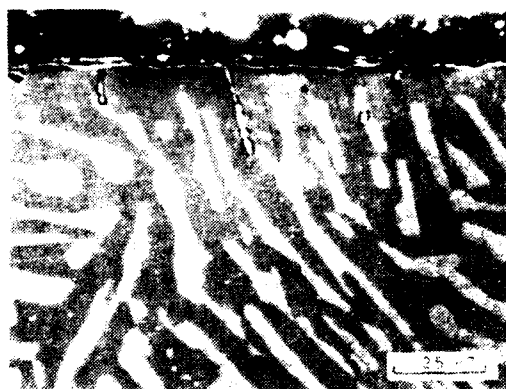
**Figure 52:** Scale/gas interface of the specimens after one week of isothermal oxidation at 1100°C, (a) Ni-7Al-0.02Y, (b) CoCrAl-0.02Y.



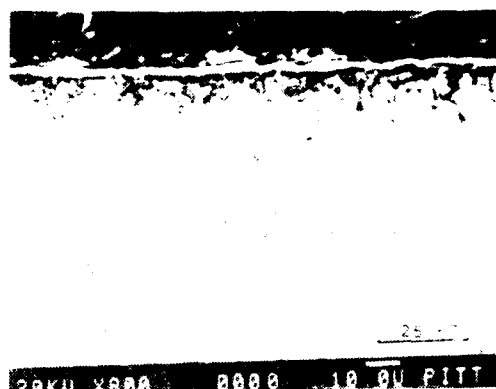
**(a) NiCrAl-0.2Y**



**(b) NiCrAl-0.8Y**



**(c) NiCrAl-0.3Hf**



**(d) CoCrAl-1.0Hf**



**(e) NiCrAl-1.0Hf**

**Figure 53:** Transverse sections of some of the specimens containing specimens oxidized for 1000 hours at 1100°C.

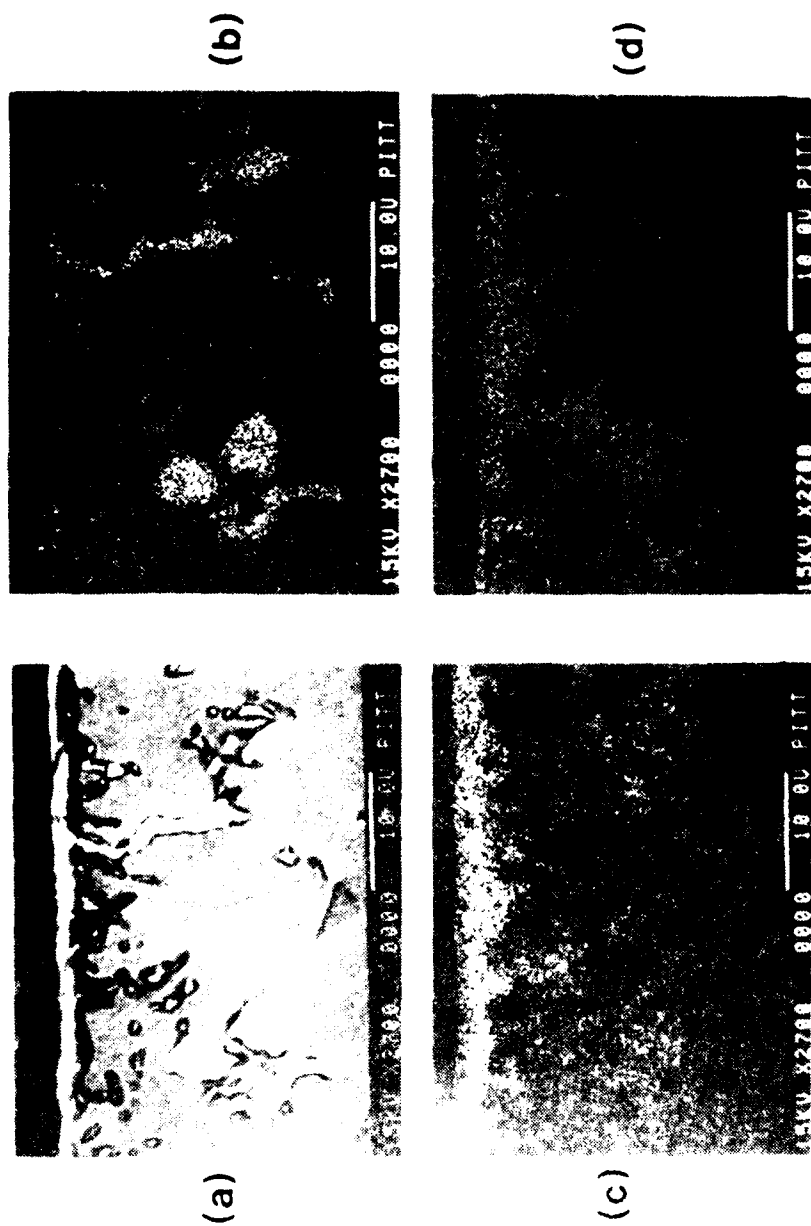


Figure 54: Transverse section of the CoCrAl-1.0Hf specimen (oxidized for one week at 1100°C) showing deep hafnium oxide protrusions at the interface, (b), (c) and (d) show the X-ray maps of Hf, Al, and O, respectively.

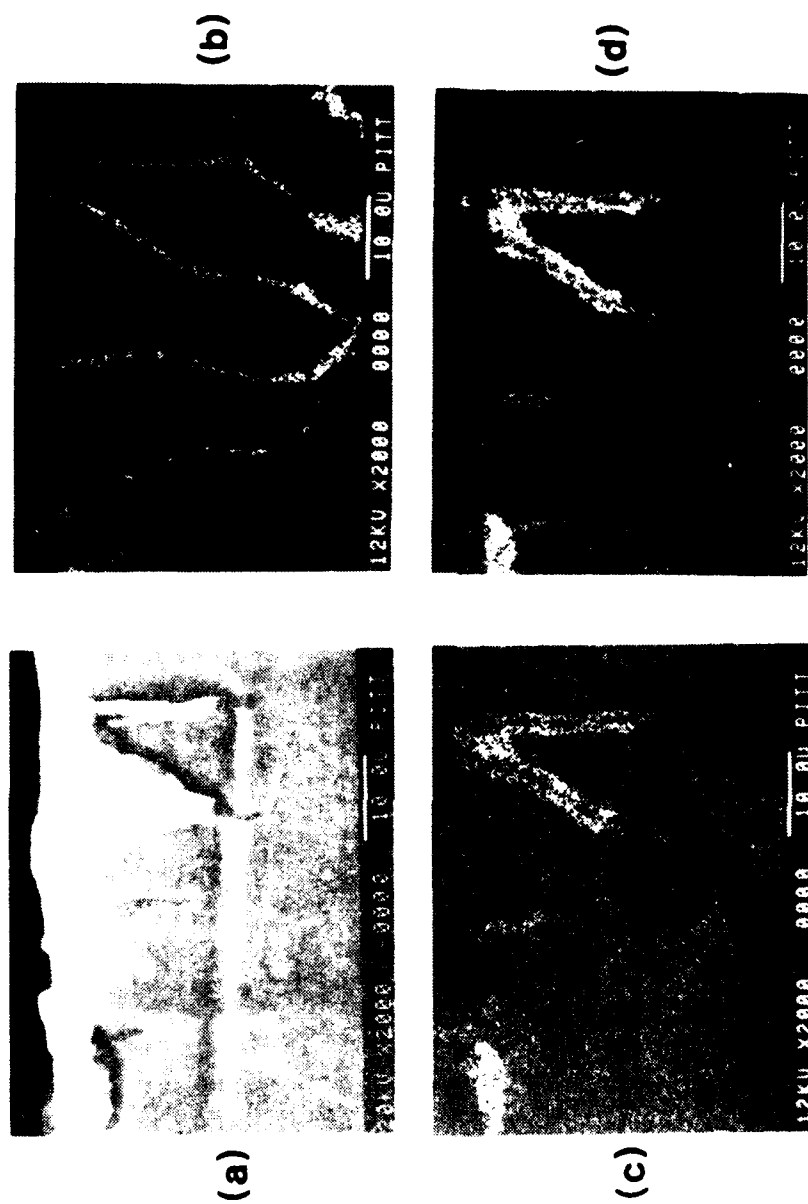


Figure 55: Transverse section of the NiCrAl-0.8Y specimen (oxidized for one week, at 1100°C) showing deep yttrium oxide protrusions at the interface, (b), (c) and show the X-ray maps of Y, Al and O, respectively.

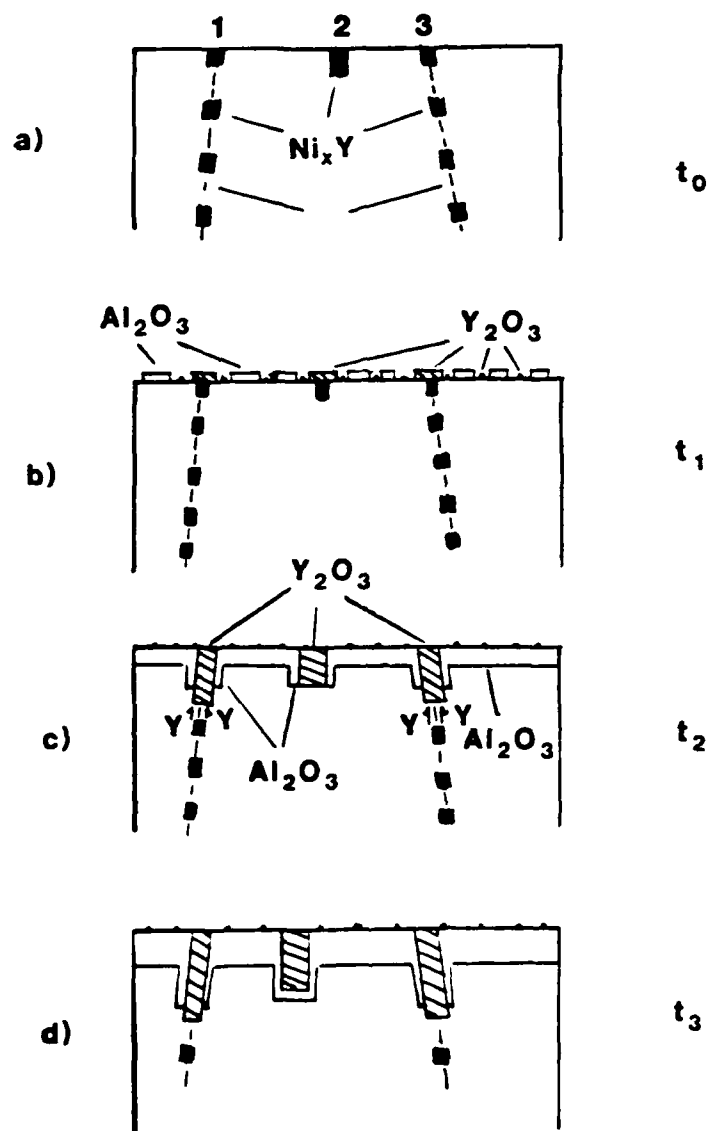


Figure 56: Schematic representation of the development of the yttrium oxide pegs during the oxidation of an alloy containing yttride phase.

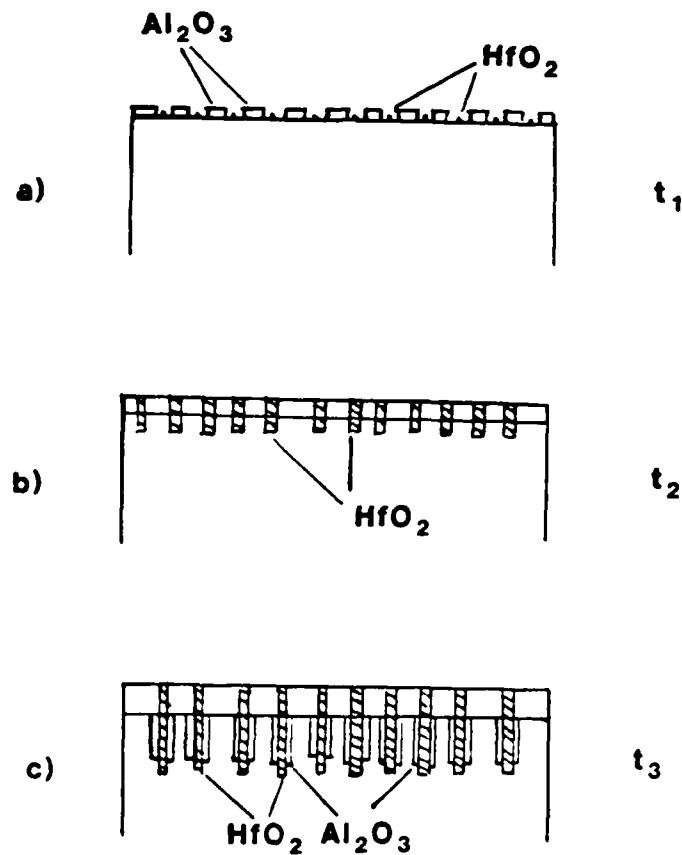


Figure 57: Schematic representation of the development of the hafnium oxide pegs during the oxidation of an alloy containing sufficient hafnium in solution prior to the oxidation.



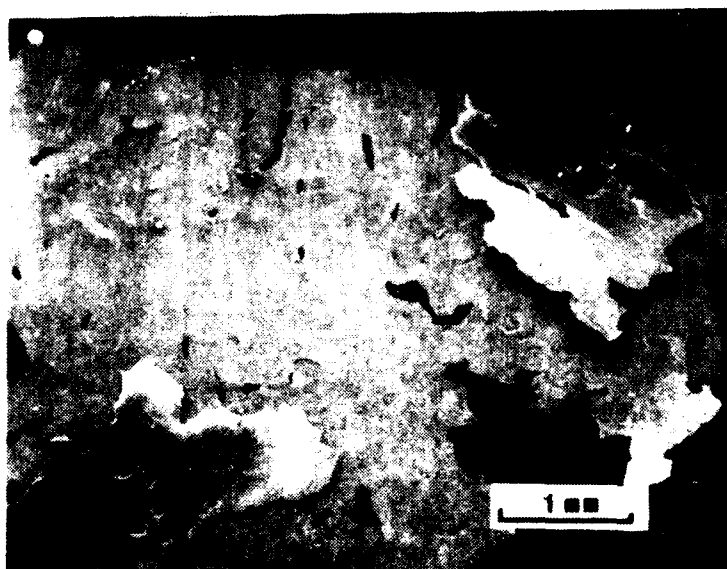


Figure 58:

Photograph showing some of the large Al<sub>2</sub>O<sub>3</sub> scale flakes spalled off from the undoped NiCrAl specimen oxidized for 24 hours at 1100°C.

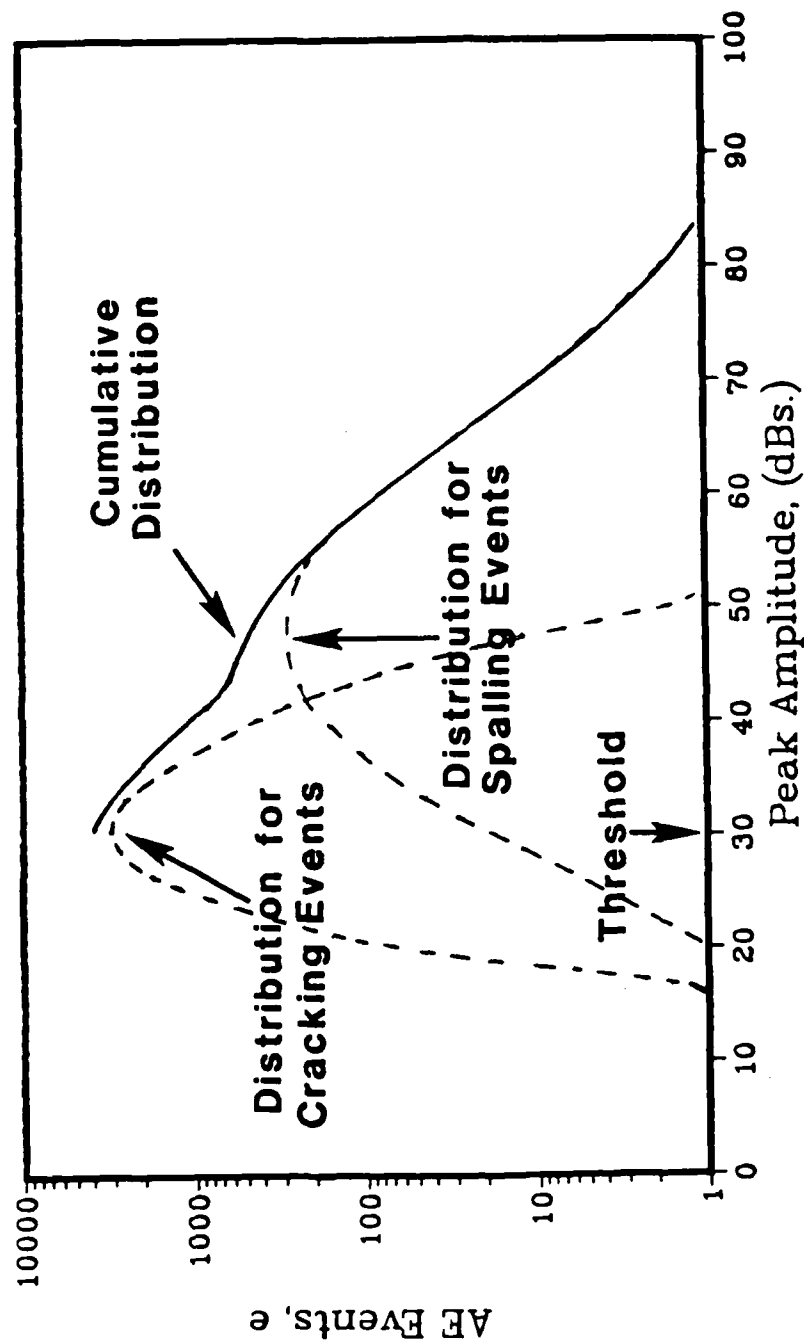


Figure 59: Schematic diagram showing a bimodal distribution of the AE events with respect to their peak amplitudes, generated during the oxide scale failure process.

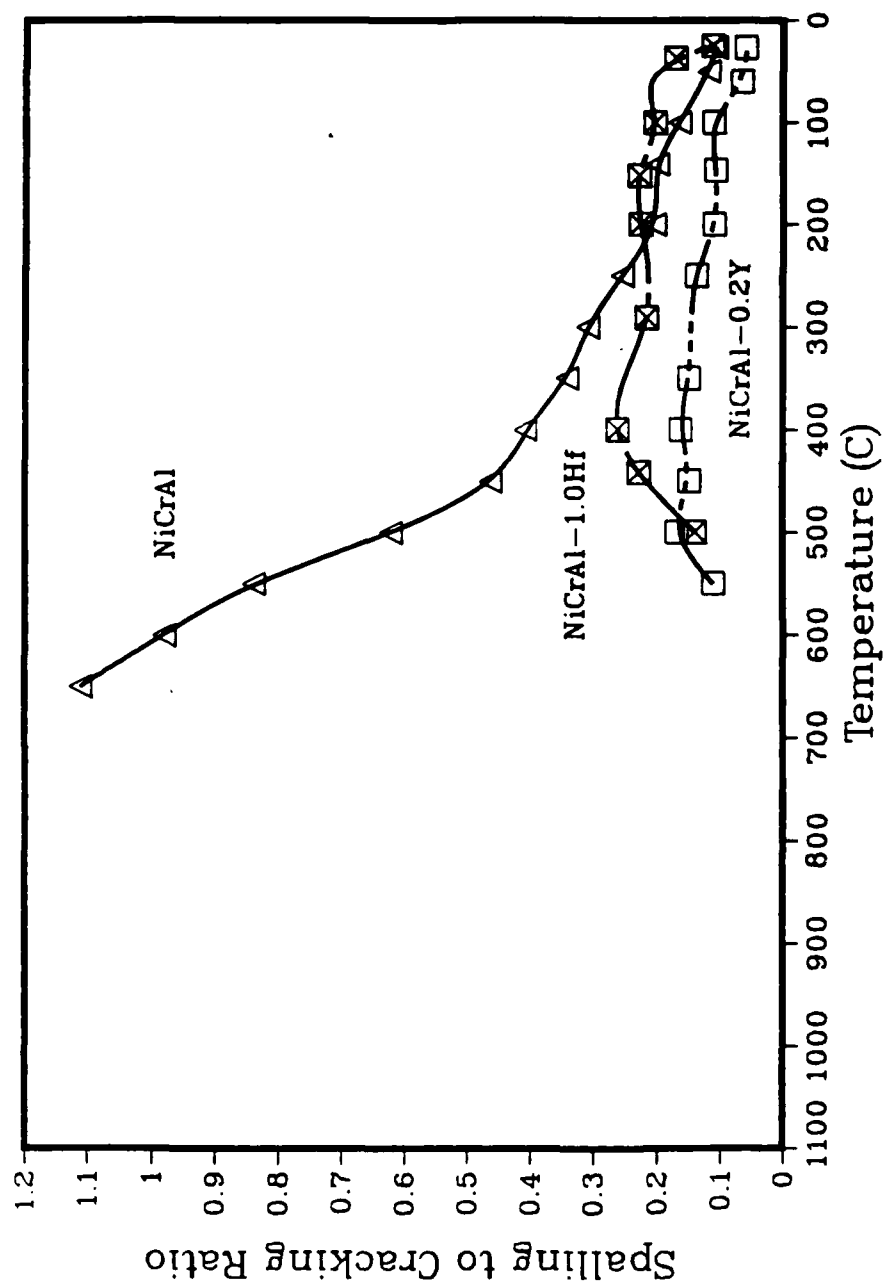
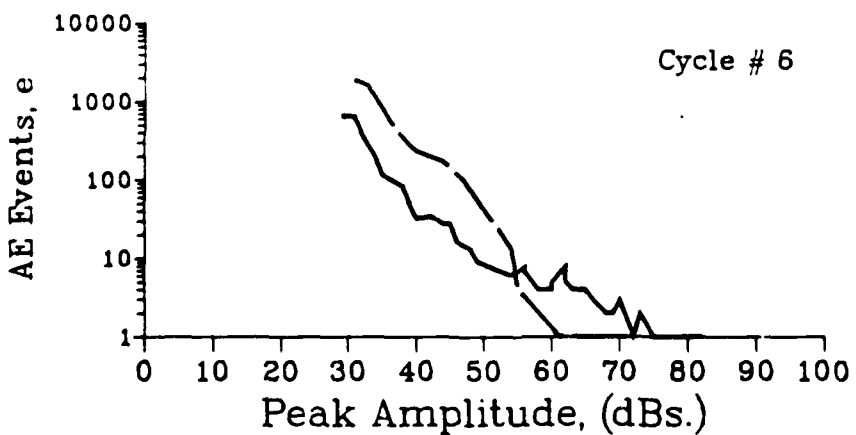
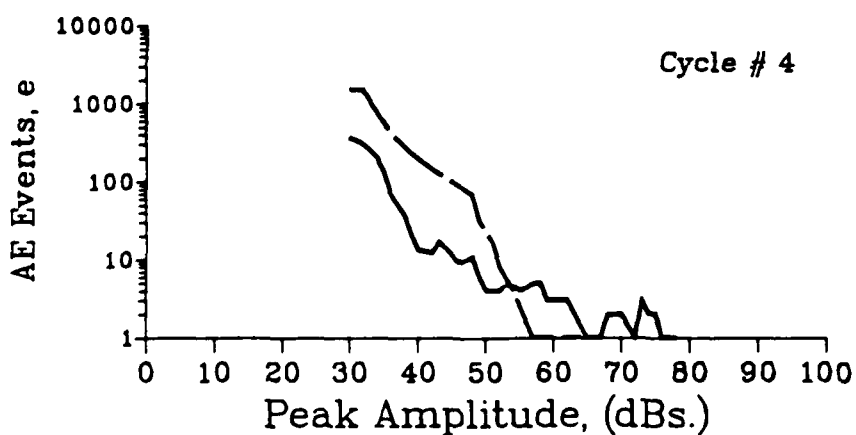
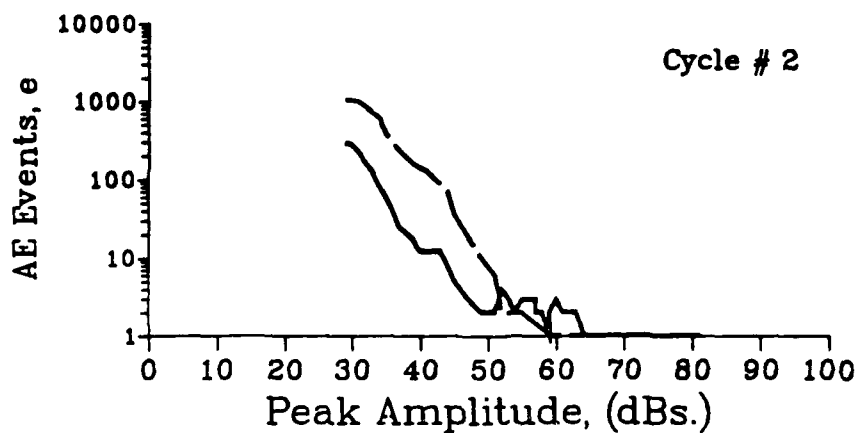


Figure 60: Spalling to cracking ratio during the cooling of NiCrAl, NiCrAl-0.2Y and NiCrAl-1.0Hf specimens after 24 hours of isothermal oxidation at 1100°C.

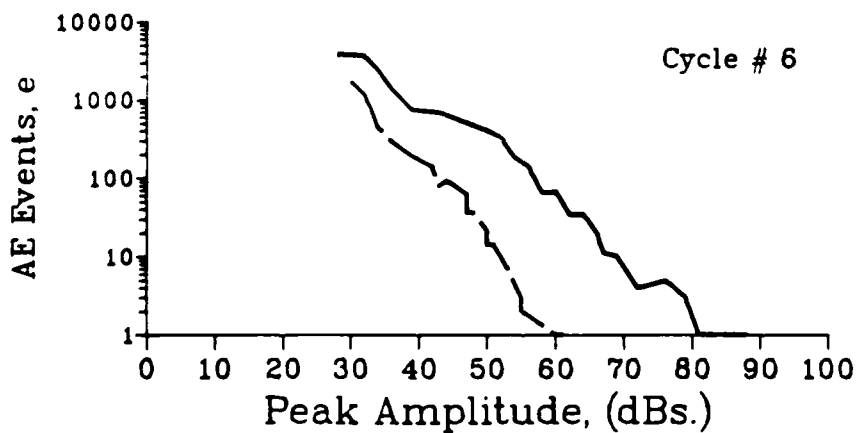
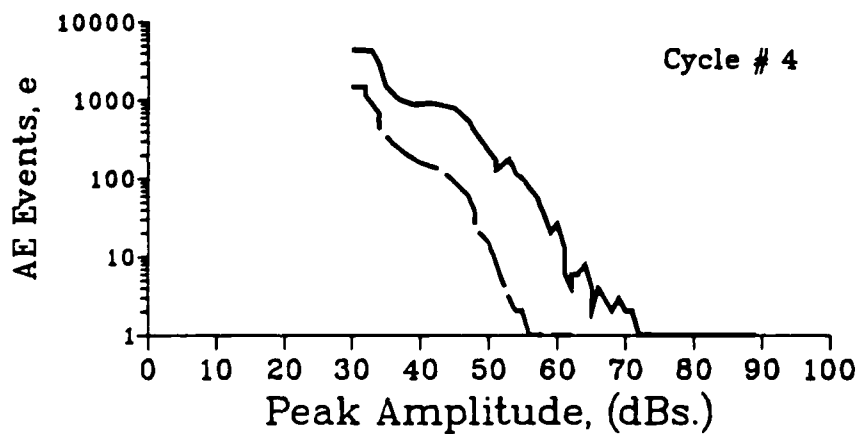
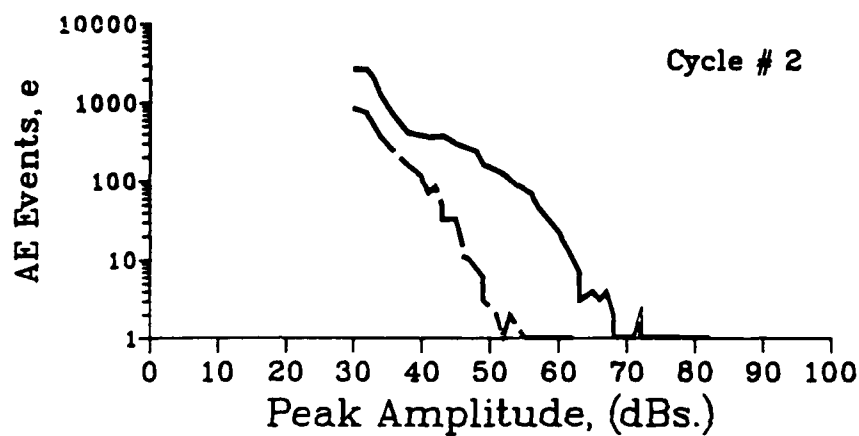


Legend

NiCrAl-0.2Y

NiCrAl-1.0Hf

Figure 61: Comparison of the peak amplitude distributions between the cyclically oxidized NiCrAl-0.2Y and NiCrAl-1.0Hf specimens.

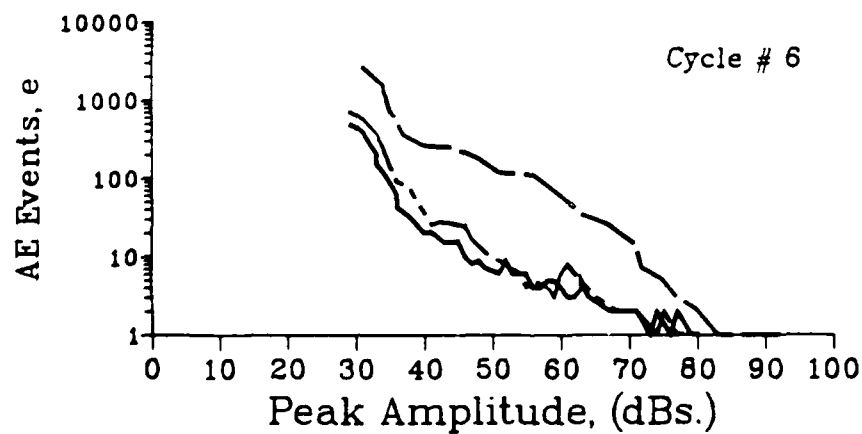
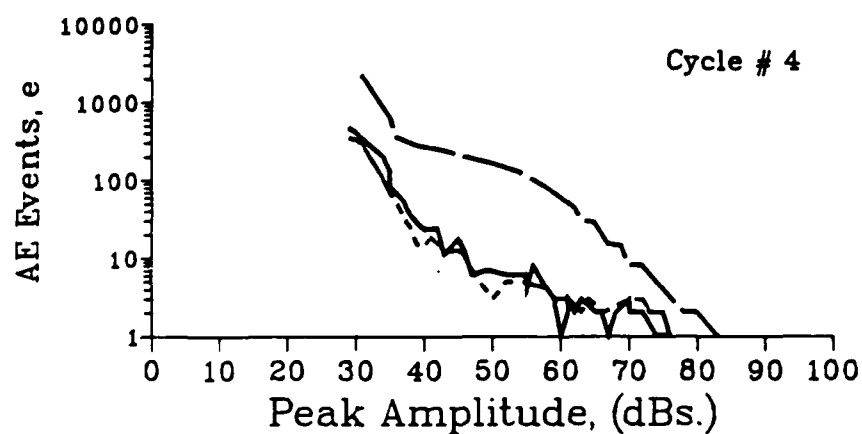
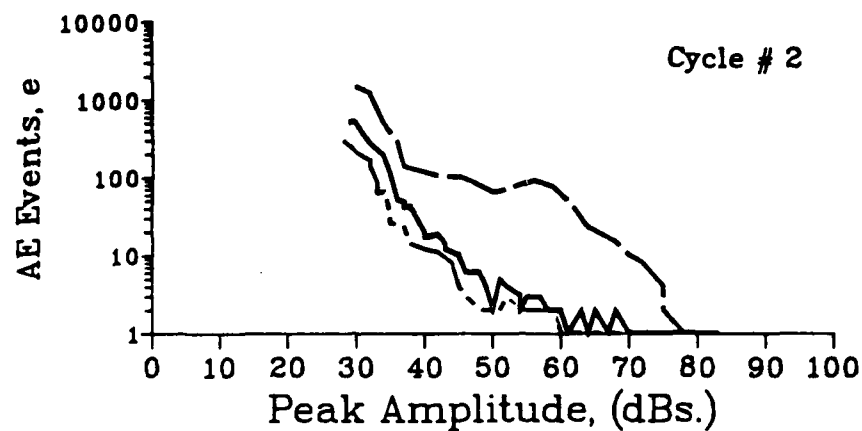


Legend

NiCrAl-0.3Hf

NiCrAl-1.0Hf

Figure 62: Comparison of the peak amplitude distributions between the cyclically oxidized NiCrAl-1.0Hf and NiCrAl-0.3Hf specimens.



### Legend

NiCrAl-0.02Y

NiCrAl-0.8Y

NiCrAl-0.2Y

Figure 63: Comparison of the peak amplitude distributions between the cyclically oxidized NiCrAl-0.2Y, NiCrAl-0.02Y and NiCrAl-0.8Y specimens.

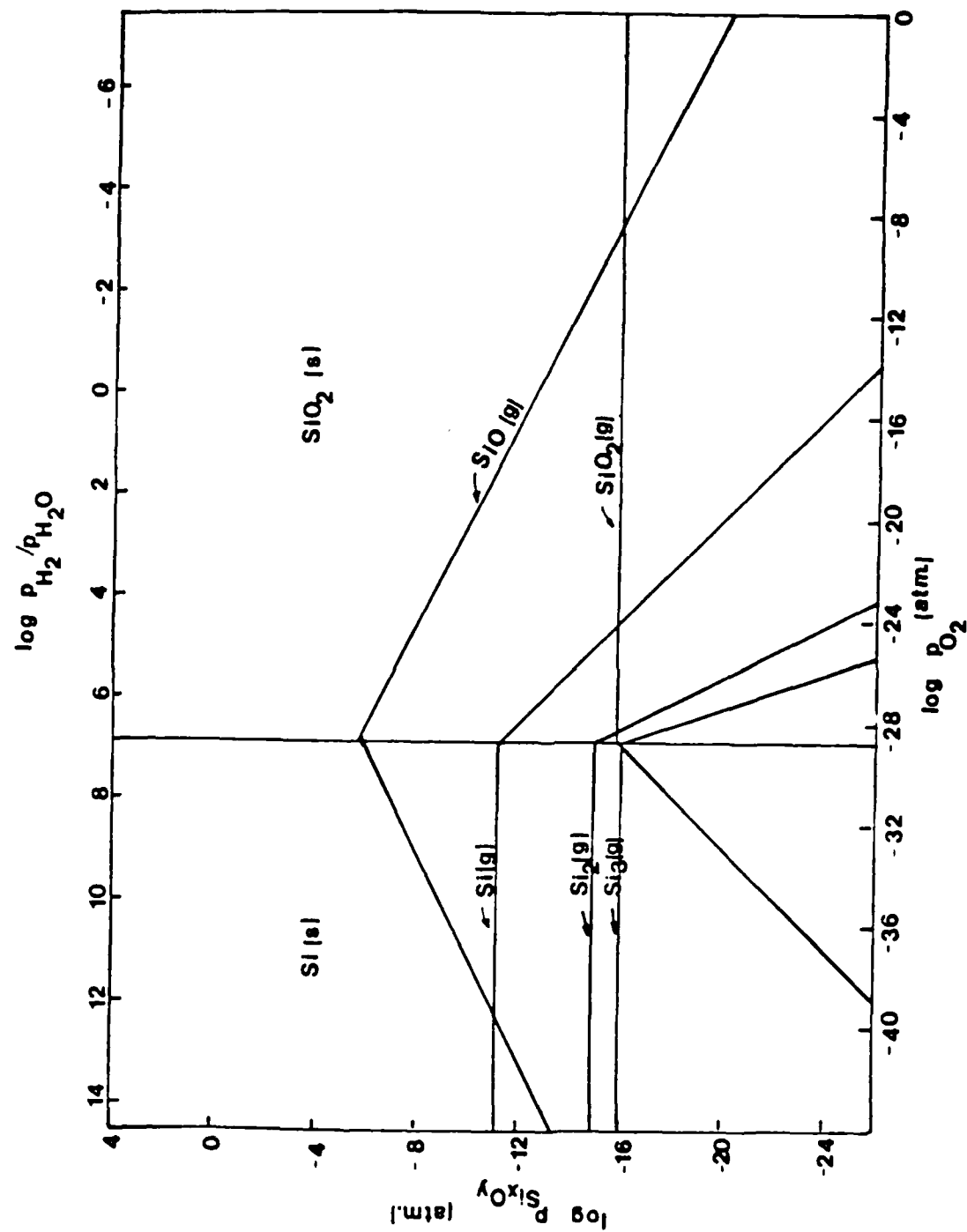


Figure 64: Si-O system volatile species at 1250°K.

# OXIDATION of Ni-Si ALLOYS in AIR at 1100 C

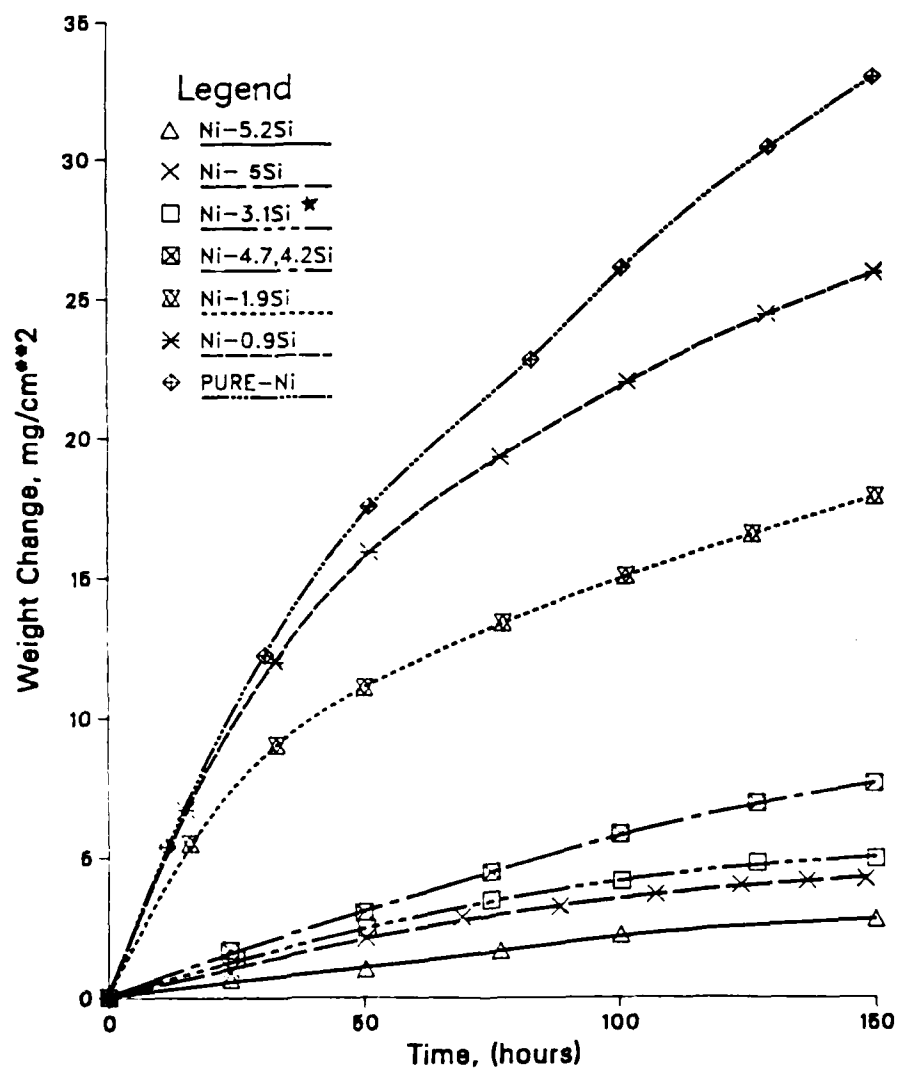


Figure 65: Weight change versus time data for the isothermal oxidation of some nickel-silicon alloys at 1100°C in air.



# OXIDATION of Ni-Si ALLOYS at 1000 C

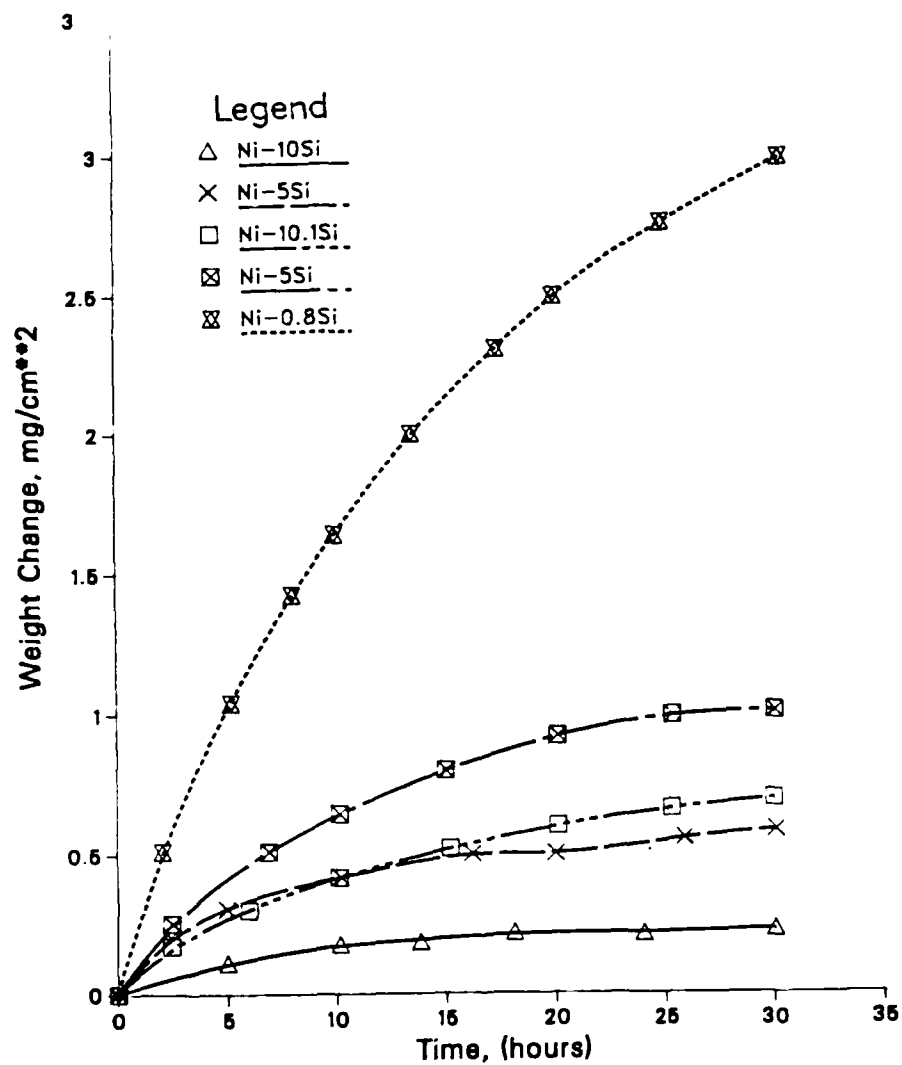


Figure 66: Weight change versus time data for oxidation of nickel-silicon alloys at 1000°C in air.

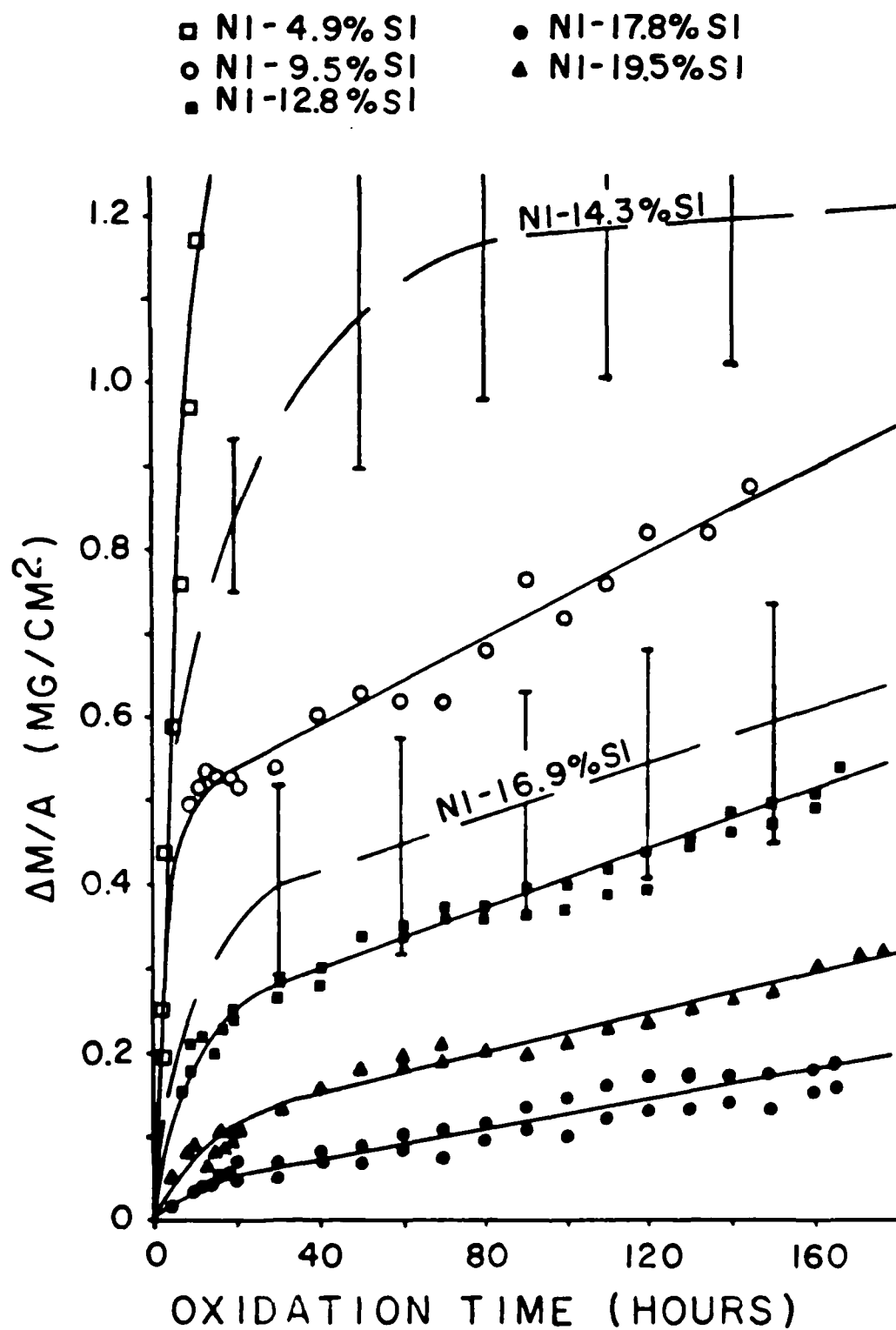


Figure 67: Weight change versus time data for the oxidation of some of the alloys used in this program at 1100°C in air (compositions are given in analyzed values).



### Ni-20Si, Oxidized at 950 C for 1 hr.

Figure 4a: Transmission micrograph of oxide stripped from two phase region of a Ni-20Si alloy, the light phase is continuous vitreous silica. The dark phase is transient oxide identified as Ni<sub>3</sub>SiO<sub>4</sub>, see superimposed SAD pattern.

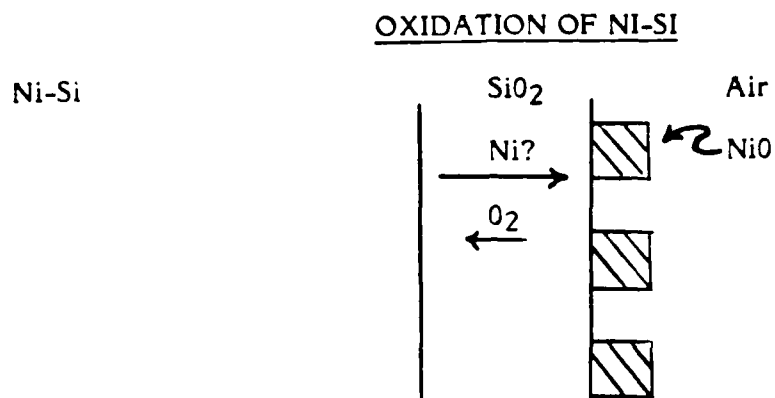
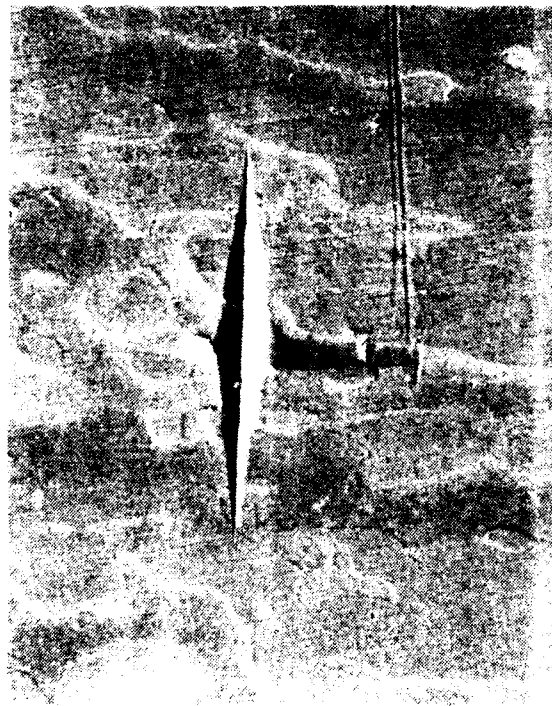
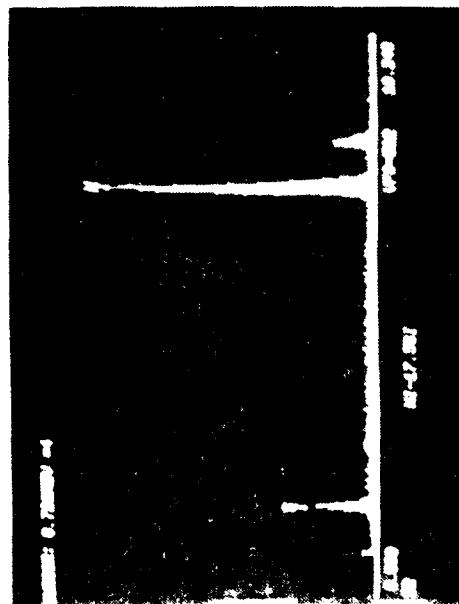


Figure 69: Schematic showing nickel diffusion through SiO<sub>2</sub> to form NiO at the SiO<sub>2</sub> - gas interface.



(B)

(C)



(A)

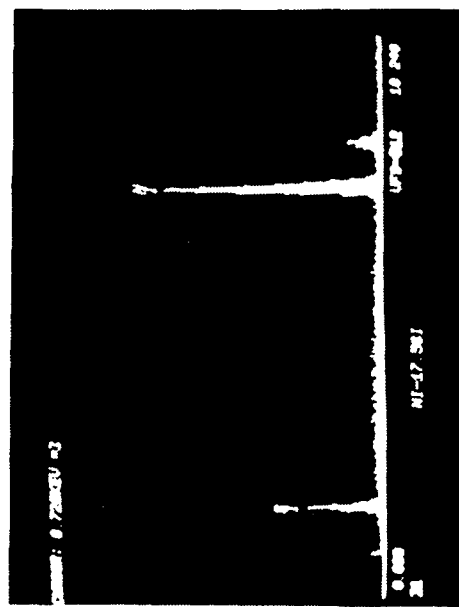


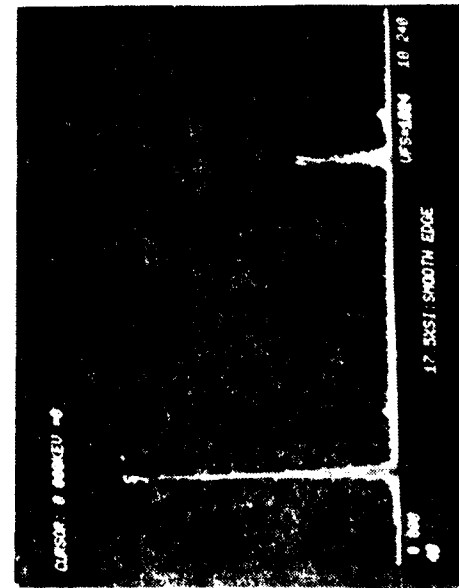
Figure 70:

Photograph of the surface of a Ni-17.5Si specimen after 15 minutes of oxidation at 1100°C, (A), and energy dispersive X-ray spectra from the light phase, (B), and the dark phase, (C), visible on this specimen.



(B)

(C)



(A)

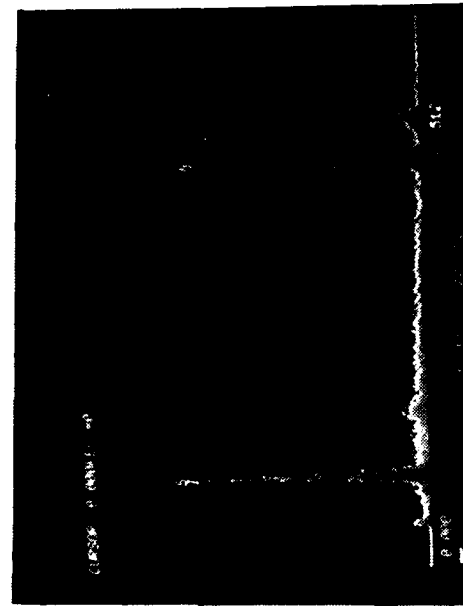


Figure 21:  
Photograph of the oxide formed on a Ni-17.5Si specimen after 180 hours of oxidation at 1100°C, (A), and energy dispersive X-ray spectrum for the inner portion of this oxide, (B), and the outer portion, (C), that appears as discontinuous white particles in (A).

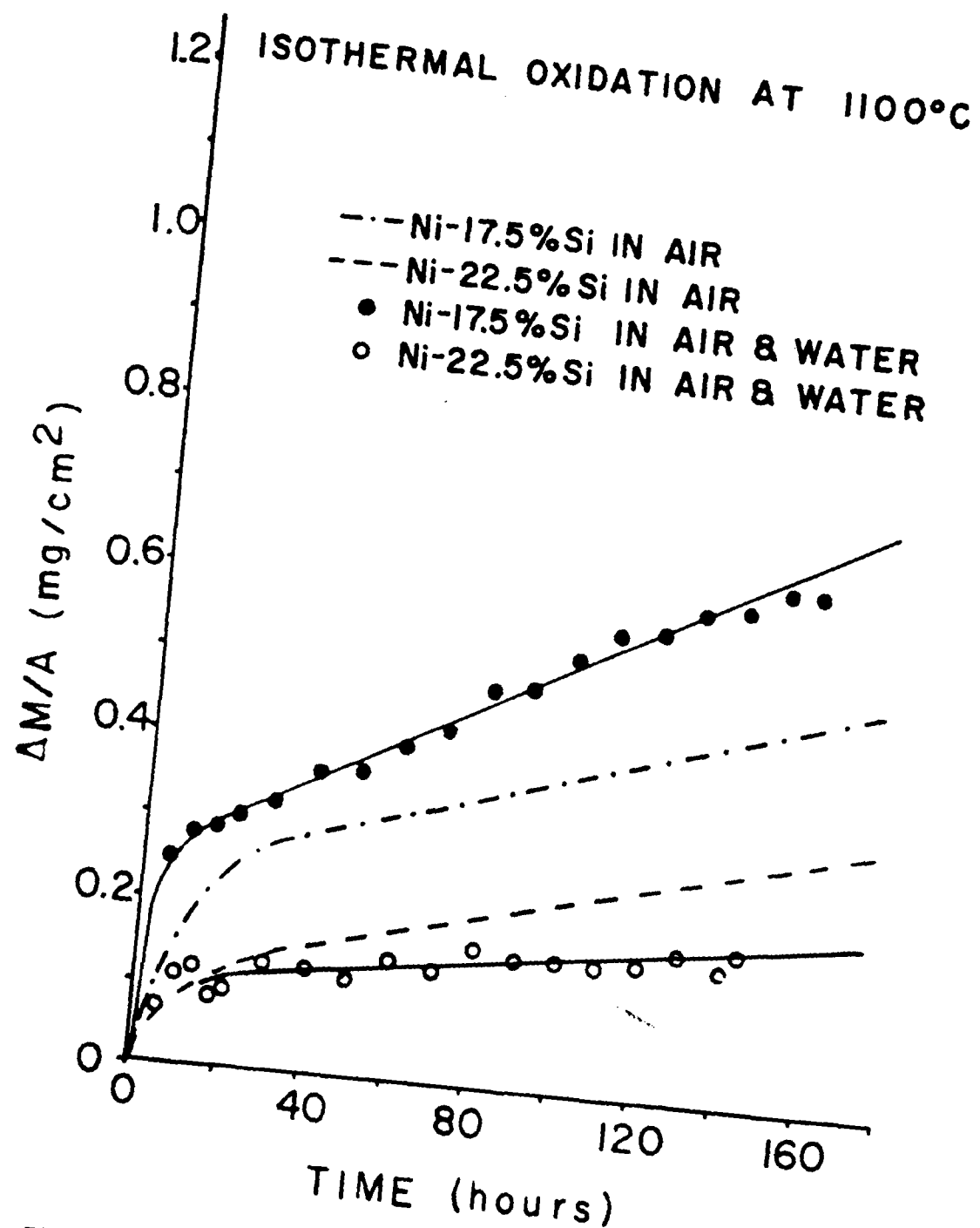


Figure 72: Weight changes versus time data for oxidation of some Ni-Si alloys in air and in air containing water vapor.

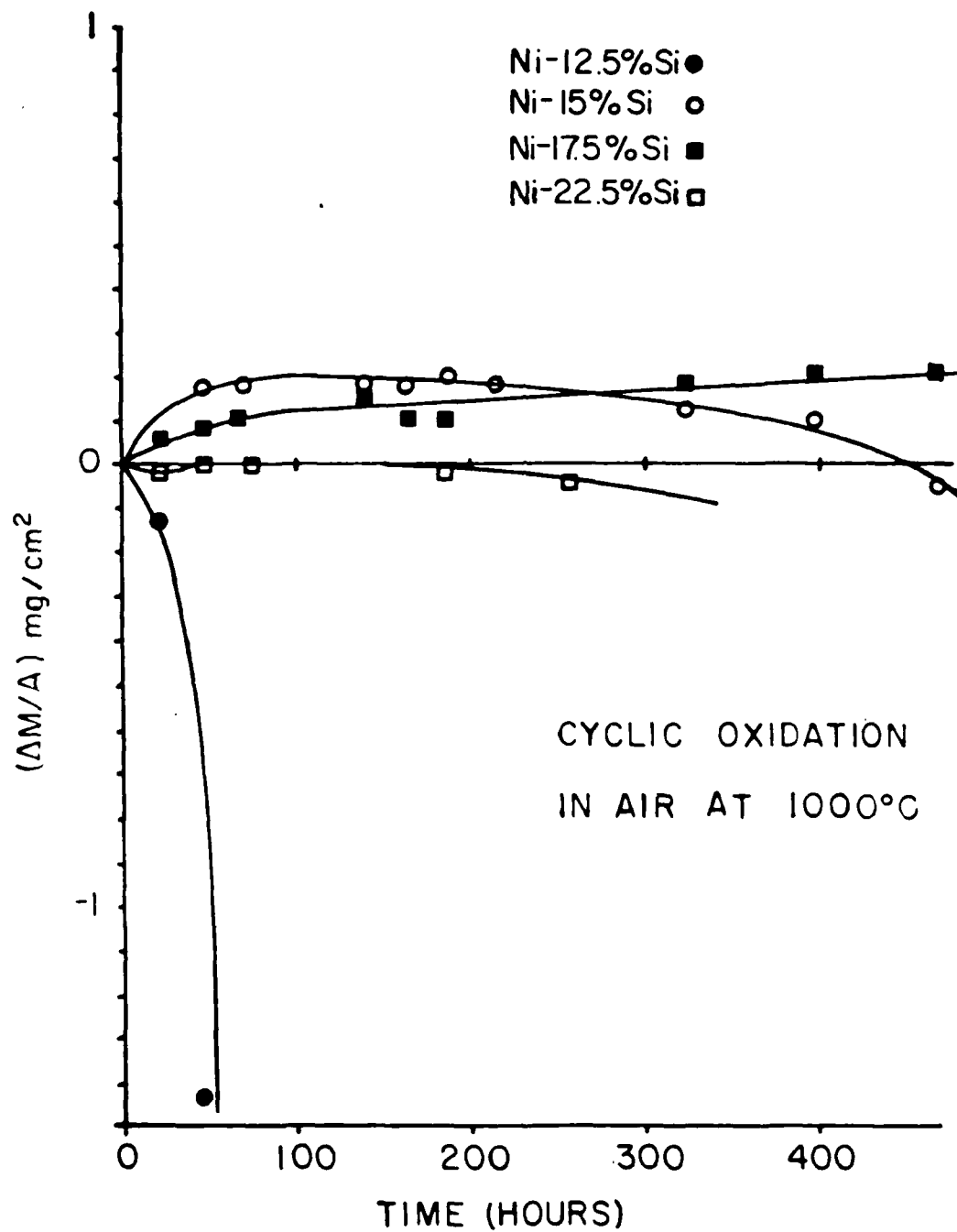


Figure 73: Cyclic oxidation data for some Ni-Si alloys in air at 1000°C.



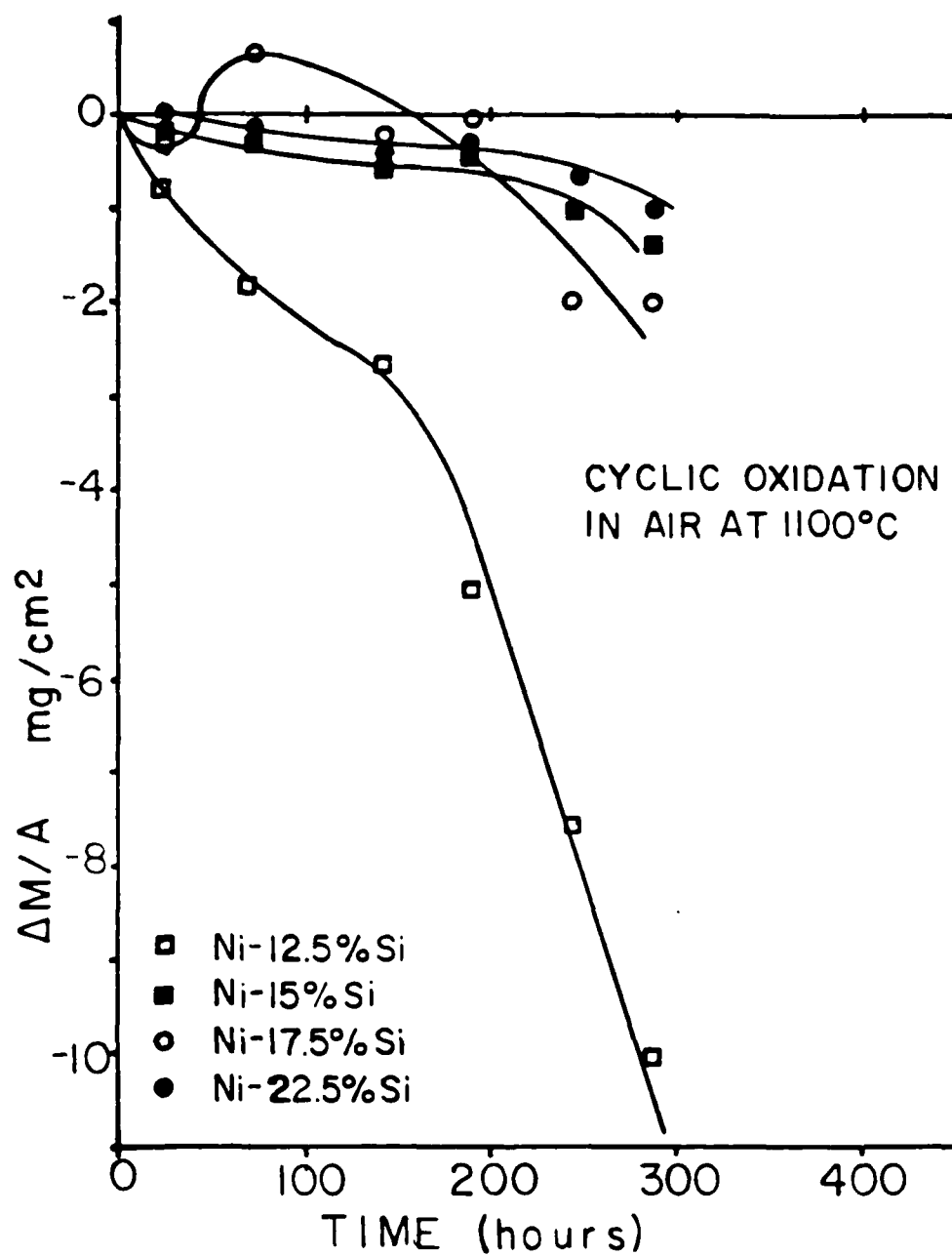


Figure 74: Cyclic oxidation data for some Ni-Si alloys in air at 1100°C.

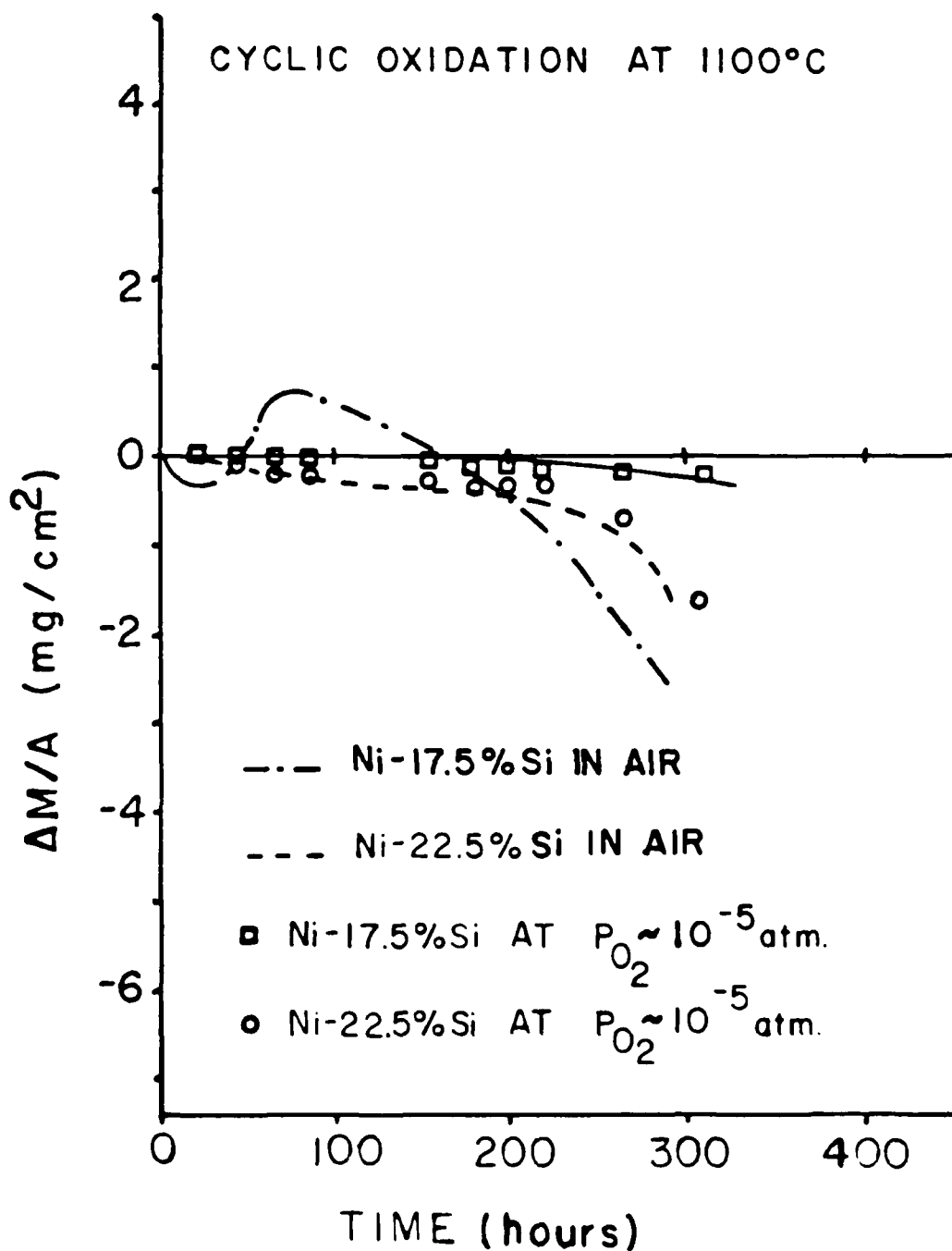
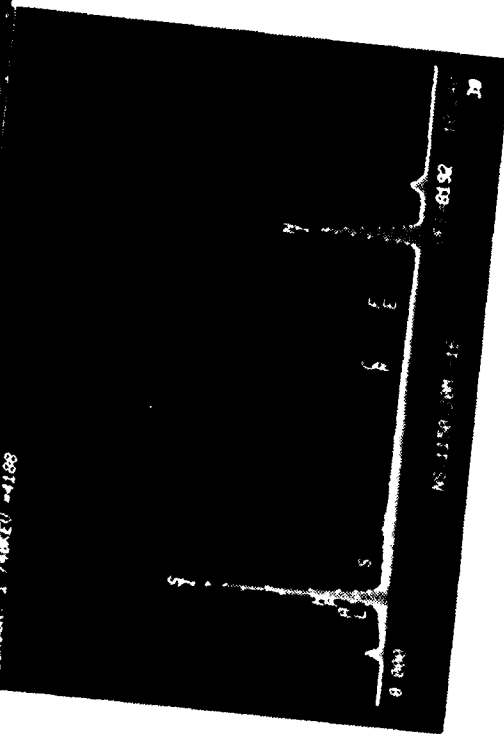


Figure : Cyclic oxidation data comparing results obtained in air and at a reduced oxygen pressure.



Figure 2

Surface photographs of Ni-20Si specimen after oxidation which show surface features indicative of SiO volatilization.



**Ni-20Si, 1150 C, 30 min Oxidation ( $\log P_{O_2} = -15.3$ )**

END

DT/C

8-86